



POLITECNICO
MILANO 1863

SCUOLA DI INGEGNERIA INDUSTRIALE
E DELL'INFORMAZIONE

Guidance and Feedback Control Solutions for Impulsive and Continuous Rendezvous Proximity Operations

TESI DI LAUREA MAGISTRALE IN
SPACE ENGINEERING - INGEGNERIA SPAZIALE

Author: **Samuele Vincenzi**

Student ID: 214867

Advisor: Prof. Gabriella Vittoria Maria Gaias

Co-advisors: Stefano Torresan (MSc.), Thomas Peters (PhD.)

Academic Year: 2024-25

This thesis was carried out in collaboration with OHB System AG, within the AOCS & GNC Department in Bremen, Germany. I am grateful for the opportunity to contribute to their work and for the support provided throughout the research.



Abstract

This thesis addresses the development of control algorithms for the final approach phase of rendezvous and docking (RVD) missions, along with an additional analysis on formation flying using an eccentricity/inclination (e/i) separation orbit. The study investigates the relative translational motion between spacecraft using both Cartesian coordinates and the Relative Orbital Elements (ROE) framework. These representations enable the formulation of guidance profiles and feedback controllers capable of tracking reference trajectories while satisfying the constraints imposed by discrete-thrust actuators. Both impulsive and continuous thrust scenarios are considered for guidance design. Linear optimal control strategies, particularly the Linear Quadratic Regulator (LQR), are employed for feedback control in both Cartesian and ROE domains, with extensions made from near-circular to eccentric orbital configurations. For rotational dynamics, the chaser is equipped with an LQR-based attitude control system, assuming a cooperative target maintaining a fixed orientation in its Local Vertical Local Horizontal (LVLH) frame. Thruster management is implemented via pulse-width modulation, tailored to the limitations of non-throttleable propulsion systems. A high-fidelity simulator was developed to model the relevant dynamics, disturbances, and onboard subsystems, including guidance, control, and actuation logic. Extensive simulations validate the control strategies and demonstrate robust performance in a variety of mission scenarios.

Keywords: near-circular relative motion, eccentric relative motion, RV&D, Formation flying, impulsive guidance, continuous guidance, rendezvous, LQR control, relative orbital elements (ROE), relative attitude dynamics, LVLH, rendezvous simulator

Abstract in lingua italiana

Questa tesi affronta lo sviluppo di algoritmi di controllo per la fase di avvicinamento finale in missioni di rendezvous e docking (RVD), includendo un'analisi aggiuntiva sul 'Formation flying' tramite un'orbita con separazione di eccentricità/inclinazione (e/i). Lo studio analizza il moto traslazionale relativo tra satelliti utilizzando sia la rappresentazione cartesiana sia il framework degli Elementi Orbitali Relativi (ROE). Queste formulazioni permettono la progettazione di profili di guida e controllori in retroazione capaci di seguire accuratamente traiettorie di riferimento, rispettando al contempo i vincoli imposti da attuatori a spinta discreta. Sono considerati scenari di guida sia impulsiva che continua. Per il controllo in retroazione, vengono adottate strategie di controllo ottimale lineare, in particolare il regolatore lineare quadratico (LQR), applicato sia nel dominio cartesiano che in quello ROE, con estensioni da orbite quasi-circolari a orbite eccentriche. Le dinamiche rotazionali del 'chaser' sono gestite tramite un controllore d'assetto LQR, assumendo un 'target' cooperativo che mantiene un orientamento fisso rispetto al proprio sistema di riferimento LVLH (Local Vertical Local Horizontal). La gestione dei propulsori è realizzata tramite una modulazione della larghezza d'impulso (PWM), adattata alle limitazioni di sistemi propulsivi non modulabili. È stato sviluppato un simulatore ad alta fedeltà per modellare le dinamiche orbitali, le perturbazioni ambientali e i sottosistemi di bordo, inclusi guida, controllo e gestione degli attuatori. I risultati delle simulazioni confermano l'efficacia e la robustezza delle strategie di controllo proposte in diversi scenari missione.

Parole chiave: moto relativo quasi-circolare, moto relativo eccentrico, RV&D, volo in formazione, guida impulsiva, guida continua, rendezvous, controllo LQR, elementi orbitali relativi (ROE), dinamica relativa d'assetto, LVLH, simulatore di rendezvous

Contents

Abstract	i
Abstract in lingua italiana	iii
Contents	v
1 Introduction	1
1.1 Background	1
1.2 Heritage and Past Missions	2
1.3 Drivers and Phases of a Rendezvous Mission	4
1.4 Contents and Contributions	6
2 Relative Motion Dynamics	9
2.1 Reference Frames	10
2.1.1 Earth-Centered Inertial Frame (ECI)	10
2.1.2 Spacecraft Local Orbital Frame (LVLH)	11
2.1.3 Spacecraft Body Frame	12
2.2 Cartesian-based Translational Dynamics	12
2.2.1 Tschauner-Hempel Equations	13
2.2.2 Hill-Clohessy-Wiltshire Equations	16
2.2.3 Solutions of HCW Equations	17
2.2.4 Solutions of TH Equations	19
2.3 ROE-based Translational Dynamics	21
2.3.1 The Relative Orbital Elements	22
2.3.2 The ROE Equations	25
2.3.3 Solutions of ROE Equations	29
2.3.4 ROE-TH Framework for Keplerian Motion	30
2.4 Rotational Motion	32
2.4.1 Absolute Dynamics and Kinematics	32

2.4.2	Relative Dynamics	34
2.4.3	Relative Kinematics	36
2.4.4	Relative Equations of Motion	36
3	Rendezvous Simulator: Structure and Components	39
3.1	Real world	40
3.1.1	Dynamics	40
3.1.2	External Disturbances	44
3.2	On-Board Software	44
3.2.1	Translational Guidance & Control	45
3.2.2	Attitude Control	46
3.2.3	Actuators Management	46
4	RVD guidance & control	49
4.1	Guidance	49
4.1.1	Impulsive Guidance Profile	50
4.1.2	Continuos Guidance Profile	56
4.2	Feedback Control	58
4.2.1	Rendezvous Control Problem	58
4.2.2	Linear Optimal Control	60
4.2.3	Reference Tracking with LQR	63
4.2.4	LQR Control of Rendezvous Dynamics	64
5	Simulations and Case Studies	67
5.1	Hypothesis and Data Selection	68
5.1.1	Target Vehicle	68
5.1.2	Chaser Vehicle	71
5.2	Test 1: Control Gain Tuning with the Target in a Circular Orbit	73
5.3	Test 2: RV&D using Impulsive Guidance	75
5.4	Test 3: RV&D using Continuous Guidance	77
5.5	Test 4: Formation Flying using e/i Separation Orbit	78
6	Results	81
6.1	Test 1: Control Gain Tuning with the Target in a Circular Orbit	81
6.2	Test 2: RV&D using Impulsive Guidance	85
6.3	Test 3: RV&D using Continuous Guidance	99
6.4	Test 4: Formation Flying using e/i Separation Orbit	105
7	Conclusions and Recommendations	107

Bibliography	111
A Appendix: Relative Motion Dynamics	117
B Appendix: Results	121
B.1 Test 2: RV&D using Impulsive Guidance	121
B.2 Test 3: RV&D using Continuous Guidance	123
List of Figures	125
List of Tables	127
List of Symbols	129
List of Acronyms	133
Acknowledgements	135

1 | Introduction

1.1. Background

Rendezvous is a fundamental technology that refers to many missions involving more than one spacecraft. It is defined as the process of bringing multiple spacecraft close to each other in space, usually to a specific point or orbit. Rendezvous is a key technique in scenarios such as [16]:

- Satellite servicing missions: to repair, refuel, or upgrade satellites that are already in orbit.
- Space debris removal missions: to capture and remove defunct satellites or space debris from orbit, reducing the risk of collisions and debris accumulation.
- Re-supply of orbital platforms and stations: to deliver supplies, equipment, or fuel to space stations or other spacecraft.
- Exchange of crew between two spacecraft.
- On-orbit assembly and manufacturing missions.
- Interplanetary rendezvous missions: to bring spacecraft together in orbit around another planet or moon, or to rendezvous with asteroids and comets for exploration.
- Formation flying missions: maintaining precise relative positions of multiple spacecraft in orbit for cooperative tasks such as scientific observations or Earth monitoring.
- Autonomous Rendezvous and Docking (AR&D) missions: to perform rendezvous and docking operations autonomously, often used for spacecraft that need to dock without human intervention.
- Sample return missions: to collect and return samples from other celestial bodies like the Moon, asteroids, or comets.

The two satellites are often referred to as the *target* (or *chief*) and the *chaser* (or *deputy*).

The former is the destination or primary objective of the mission, while the latter is the satellite that must actively control its relative state with respect to the target during the mission. The docking/berthing process involves a series of orbital maneuvers that bring the active vehicle (chaser) into proximity with the passive vehicle (target) and ultimately into physical contact.

Docking refers to bringing the chaser into alignment with the docking interface of the target, where they connect directly, often with automated or manual assistance. In contrast, *berthing* involves the precise delivery of the chaser to a position with nominally zero relative velocity and angular rate, after which a manipulator (typically a robotic arm) grapples the chaser and moves it into its final position for secure attachment. This category of missions is referred to as *rendezvous and docking or berthing (RVD/B)* [16].

Another type of rendezvous mission is defined as *formation flying* [3]: the operation of two or more spacecraft that autonomously or manually fly in close proximity while maintaining precise relative positions and velocities.

A rendezvous mission is considered *automated* when operations are executed without human intervention, following a pre-programmed sequence of instructions. In contrast, a mission is considered *autonomous* when the spacecraft performs operations independently and is capable of making decisions based on sensor inputs, environmental conditions, or mission objectives.

The target satellite is termed *cooperative* when it supports the rendezvous process by providing real-time data, such as its position, orientation, and velocity, to aid relative navigation tasks. It is considered *collaborative* when it additionally performs actions, such as adjusting its attitude or trajectory, to actively assist in tasks like safe docking, capture, or other proximity operations.

This document focuses on rendezvous missions involving a cooperative target. The chaser spacecraft is assumed to have decision-making capabilities, implemented through a feedback controller that acts on a pre-programmed guidance profile to track a desired reference trajectory. While the primary emphasis is on rendezvous and docking (RVD) missions, formation flying [8] scenarios will also be briefly addressed.

1.2. Heritage and Past Missions

The concept of orbital rendezvous has been central to the development of spaceflight since the earliest days of human exploration beyond Earth. The evolution of rendezvous systems reflects the technological philosophies of different nations. While the United States

initially adopted a manual approach emphasizing astronaut control, the Soviet Union developed automated systems prioritizing operational reliability and standardization. These parallel strategies, refined over decades, now converge in the pursuit of fully autonomous orbital rendezvous systems [47].

1. **Early concepts and diverging philosophies:** During the space race of the 1960s, the United States focused on manual rendezvous to reduce system complexity and increase pilot involvement, while the Soviets relied heavily on automation, influenced by military priorities.
2. **Vostok and Gemini:** The Soviet Vostok program achieved several early proximity operations. Notably, Vostok 3 and Vostok 4 came within 6.5 km of each other in 1962, and Vostok 5 and Vostok 6 repeated this feat in 1963. However, none of these missions included controlled rendezvous, as the spacecraft lacked maneuvering capability. The Gemini program was crucial for the U.S. in mastering rendezvous and docking techniques. Between 1965 and 1966, it achieved the first manual orbital rendezvous (Gemini VI and VII), the first docking with a target vehicle (Gemini VIII), and the development of the coelliptic approach strategy using optical and radar navigation.
3. **Soyuz and Apollo:** The Soyuz program introduced the Igla radar-based rendezvous system, enabling fully automated docking. Despite early challenges, including the fatal Soyuz 1 mission and manual docking errors during Soyuz 3, the system evolved into a reliable technology. Apollo's lunar missions demanded precise orbital rendezvous in lunar orbit. The Lunar Module (LM) had to autonomously launch from the Moon, track the Command/Service Module (CSM), and dock for return to Earth. Apollo used inertial navigation, optical sextants, and radar to achieve high-precision rendezvous. These operations were manually executed by astronauts but supported by extensive ground planning and onboard computation.
4. **Shuttle and Progress:** Between 1983 and 2005, the Space Shuttle conducted 57 rendezvous missions of varying complexity, including satellite capture, servicing, and space station assembly. Despite technological advances, its navigation system retained similarities with Gemini and Apollo, combining radar, inertial systems, and visual information, with astronauts executing final approaches. Meanwhile, the Kurs system replaced Igla in Soviet and Russian spacecraft, improving automation and reliability. Kurs allowed greater acquisition distances and finer control using advanced RF antennas and signal processing. Used by Soyuz and uncrewed Progress vehicles, Kurs remains a benchmark for automated rendezvous, despite trade-offs in

weight, power, and hardware obsolescence.

5. **Transition to autonomy:** As missions became more complex and human intervention less practical, new autonomous rendezvous missions emerged. This transition also marked a shift toward using multiple, simplified unmanned platforms, designed specifically for robotic tasks, rather than relying on complex, expensive, or unavailable crewed spacecraft modules. Key technology demonstration missions in the development of robotic rendezvous capabilities include:

- *ETS-VII (Japan, 1998)*: Conducted by NASDA, ETS-VII demonstrated autonomous rendezvous and docking between uncrewed spacecraft. The chaser (*Hikoboshi*) used GPS, laser radar (RVR), and a proximity sensor (PXS) to dock with the target (*Orihime*).
- *XSS-11 (USA, 2005)*: A microsatellite launched by the U.S. Air Force, XSS-11 performed over 20 autonomous proximity operations with derelict targets.
- *DART (USA, 2005)*: NASA's DART was designed for autonomous rendezvous with the MUBLCOM satellite. A GPS error and untuned filters led to fuel depletion and an unintended collision with the target.
- *Orbital Express (USA, 2007)*: A joint DARPA–NASA mission that demonstrated autonomous rendezvous, capture, fluid transfer, and robotic servicing.

1.3. Drivers and Phases of a Rendezvous Mission

Overview

An RVD mission typically consists of the following phases [16]:

- **Launch and orbit injection:** The chaser is brought into a stable orbit in the target orbital plane, usually in a lower orbit and at an arbitrary phase angle behind the target.
- **Phasing:** This phase reduces the phase angle between chaser and target by leveraging the shorter orbital period of the lower orbit. Launch errors in inclination and RAAN are also corrected. Phasing ends when margins on the selected 'aim point' are reached.
- **Far-range rendezvous or homing:** The objective is to achieve velocity and angular rate conditions necessary for initiating close-range maneuvers. Major tasks include orbit acquisition, velocity reduction, and timeline synchronization.

- **Close-range rendezvous or closing:** This phase reduces the distance between chaser and target to prepare for final approach. The chaser must be correctly positioned with suitable velocity, attitude, and angular rates to enter the final approach corridor. A fly-around maneuver may be required to align with the desired approach axis.
- **Final approach:** The goal is to meet docking or berthing capture conditions in terms of position, velocity, attitude, and angular rates.

Final Approach

The final approach is the most safety-critical and precision-driven phase of rendezvous. It begins when the chaser is aligned with the docking axis and within capture range. The space surrounding the target where final approach may begin is the *Approach Ellipsoid*, whose dimensions depend on the target's size and characteristics. The chaser must also remain within the *Approach Corridor*, a conical volume typically with a 10–15° aperture along the docking axis.

The goal is to guide the chaser's docking interface into the target's capture envelope, minimizing position error, approach velocity, and attitude misalignment. Trajectories may involve closed-loop controlled straight-line approaches or sequences of small thrust “hops,” depending on whether docking is automated or crew-monitored. For human missions, trajectories must be observable via video or sensors.

High-precision relative navigation is required, with position accuracy on the order of centimeters and attitude/rate errors within 1° and 0.1°/s. Final approach navigation often combines optical sensors with relative GPS.

To ensure mission safety and mitigate collision risks during this critical phase, recent guidelines such as the ESA Close Proximity Operations Working Group recommendations [13] provide standardized procedures and operational constraints for safe approach trajectories, keep-out zones, and contingency management.

Drivers

Key drivers for rendezvous mission design include [16]:

- Launch window must align with the target's orbital plane.
- Phasing strategy depends on phase angle, mission duration, and fuel constraints.
- Docking port location and orientation determine viable approach axes.

- Sensor limitations (range, field of view, lighting) constrain trajectory and timing.
- Final approach must occur under favorable Sun illumination.
- Requires coordination with communication windows and crew availability.
- Limited propellant and power restrict maneuver complexity and duration.
- Defined keep-out zones and approach corridors.
- Target may be passive or cooperative.
- Safety violations trigger automated or manual aborts.

1.4. Contents and Contributions

Contents

This study focuses on the analysis of the final approach phase of a rendezvous and docking mission, along with an additional analysis of the eccentricity/inclination separation orbit for collision avoidance during formation flying.

Chapter 2 provides a detailed overview of the relative motion dynamics. The equations of relative motion are derived for both translational and rotational states. Translational motion is analyzed using both Cartesian-based and ROE-based representations. Solutions to these equations are discussed with respect to both natural and forced motion.

Chapter 3 describes the structure of the rendezvous simulator used for numerical simulations. It focuses on implementing real-world components to simulate the operational environment, motion, and on-board software, which, based on simulated measurements, computes the required control action.

Chapter 4 presents the guidance and control algorithms. The guidance function provides the required state at each instant based on a ground-derived reference input profile. The controller operates in feedback, correcting the error between the guidance profile and the measurements. The LQR algorithm is used to generate the control gain due to its ability to guarantee system stability, desirable transient behavior, and efficient control effort.

Chapter 5 outlines the hypotheses and data used in each simulation scenario. The goal is to quantify controller performance for both eccentric and circular orbits, and under Cartesian- and ROE-based formulations. Both impulsive and continuous guidance references are considered.

Finally, Chapter 6 presents the results obtained from the numerical simulations.

Contributions

This thesis presents several original contributions to the field of spacecraft proximity operations and autonomous rendezvous and docking (RV&D) guidance and control. The main contributions are summarized below:

- **Dual-framework modeling of translational dynamics:** The relative motion between chaser and target spacecraft is modeled using both Cartesian coordinates and Relative Orbital Elements (ROEs). This dual approach allows for flexibility in control design and enhances understanding of orbital geometry and coupling effects.
- **Extension of ROE-based dynamics to eccentric orbits:** Building on classical formulations valid for circular or near-circular orbits, this work extends the ROE framework to support the dynamics of eccentric orbits using a linear time-varying (LTV) formulation. The resulting model is suited for more general mission scenarios.
- **Design and implementation of guidance profiles:** Two types of guidance strategies are developed and analyzed:
 - *Impulsive guidance*
 - *Continuous guidance*
- **LQR-based feedback control in multiple coordinate systems:** Linear Quadratic Regulator (LQR) controllers are designed for both Cartesian and ROE-based dynamics. The controllers are tuned for precision tracking of guidance profiles while respecting thrust constraints and ensuring system stability.
- **Development of a rendezvous simulation environment:** A software framework has been created to simulate the guidance, control (GNC), and actuation systems of an RV&D mission. The simulator integrates realistic orbital dynamics, discrete thruster modeling, and feedback control loops.
- **Rotational dynamics and attitude control:** The rotational motion of the chaser spacecraft is modeled under the assumption of a cooperative target. An LQR controller is implemented to maintain attitude alignment with the docking axis frame during final approach.

Together, these contributions provide a robust theoretical and practical framework for high-precision autonomous rendezvous operations and offer a solid foundation for further research in autonomous GNC systems.

2 | Relative Motion Dynamics

Accurate modeling of spacecraft relative motion is essential for the success of rendezvous operations. This chapter begins by establishing the foundational reference frames, followed by an introduction to the various dynamic models employed in the study. Emphasis is placed on the specific formulations, both translational and rotational, used in the simulations, with particular focus on the assumptions and methodological choices that reflect the unique aspects of this work. Two main approaches are examined for the translational dynamics: the Cartesian formulation and the orbital elements-based representation. Each method is evaluated for its respective advantages in analyzing and controlling spacecraft proximity operations, depending on mission-specific requirements and constraints.

Contents and Contributions

This section provides an overview of the chapter by outlining its contents and highlighting the original contributions on the derivations of the rendezvous equations of motion.

- Section 2.1 introduces the reference frames employed for the analysis of rendezvous dynamics, based on established methodologies in the literature [16].
- Section 2.2 discusses the Cartesian-based translational dynamics, presenting a detailed derivation of the governing equations for relative motion. The equations presented in this section are derived from state-of-the-art references [10, 16, 48].
- Section 2.3 explores the ROE-based translational dynamics, employing a set of quasi-nonsingular orbital elements as described in Ref. [8, 21]. While the final equations of motion are consistent with established results in the literature [8, 21, 25, 37], the linearization of the nonlinear dynamics was developed independently. The methodology for deriving the linearized equations in the ROE-based formulation is typically not disclosed in detail, only the final expressions are usually provided. This manuscript aims to bridge that gap by presenting the complete procedure, from the absolute motion equations of the chaser and target to the derivation of the linearized relative motion equations of the chaser with respect to the target vehicle. The com-

plete procedure and derivation steps are presented in this chapter. Section 2.3.4 is an extension of the work of Ref. [21], which presents the ROE-HCW framework for near-circular orbits. This study includes an original extension to the eccentric case.

- Section 2.4 details the derivation of the equations of motion used for rotational dynamics. Although inspired by existing research [4, 27], the equations were independently derived and adapted to meet the specific requirements of the simulations conducted in this study.

2.1. Reference Frames

This section aims to describe the reference frames commonly used in the analysis of the rendezvous problem. It begins with the *Earth-Centered Inertial* (ECI) reference frame, which serves as the baseline for describing the absolute motion of both the chaser and the target spacecraft. The discussion then moves to the *spacecraft local orbital frame* (also known as the LVLH frame), which is essential for analyzing the relative motion of the chaser with respect to the target. Finally, the *spacecraft body frame* is introduced to study the satellite's attitude in relation to its mission objectives.

2.1.1. Earth-Centered Inertial Frame (ECI)

The frame \mathcal{F}_{ECI} is used to describe a satellite's motion relative to the center of the Earth and with respect to fixed inertial directions in space.

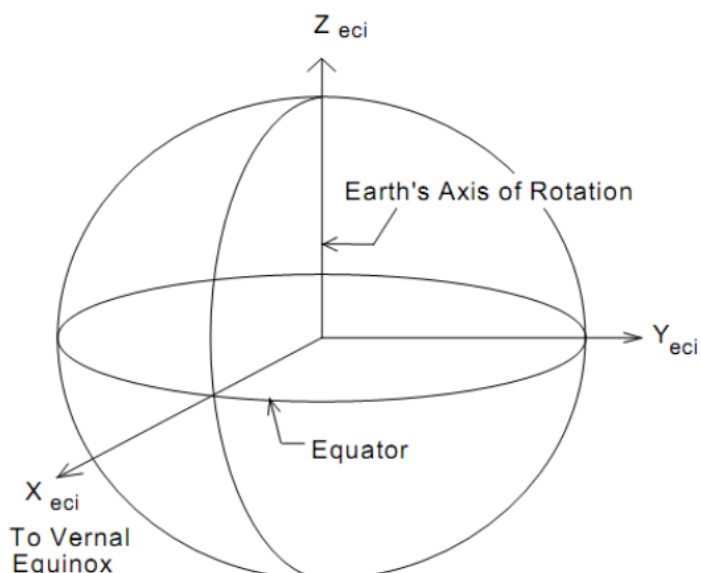


Figure 2.1: ECI reference frame (from Ref. [34])

The reference frame consists of:

- Origin O_{ECI} : the center of the Earth; it is approximated as a sphere, with the assumption that its geometric center coincides with its center of mass.
- Axis \mathbf{x}_{ECI} : lies in the equatorial plane, pointing toward the vernal equinox.
- Axis \mathbf{y}_{ECI} : completes the right-handed coordinate system ($\mathbf{y}_{\text{ECI}} = \mathbf{z}_{\text{ECI}} \times \mathbf{x}_{\text{ECI}}$).
- Axis \mathbf{z}_{ECI} : aligned with the Earth's rotational axis, pointing toward the celestial north pole.

2.1.2. Spacecraft Local Orbital Frame (LVLH)

The frame $\mathcal{F}_{\text{LVLH}}$ is used to describe a satellite's motion relative to its position along the orbit or, in the context of rendezvous dynamics, to describe the motion of the chaser with respect to the target.

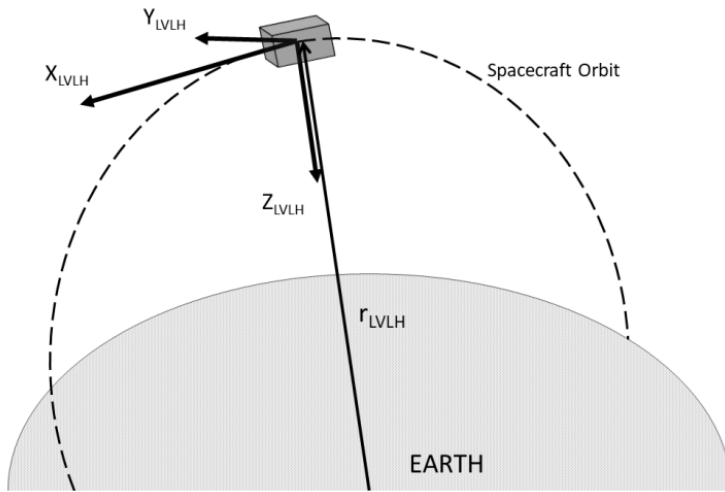


Figure 2.2: LVLH reference frame (from Ref. [6])

The reference frame consists of:

- Origin O_{LVLH} : the center of mass of the target spacecraft.
- Axis \mathbf{x}_{LVLH} : it describes the transverse direction, which is perpendicular to the radial one. In a circular orbit, the transverse direction aligns with the velocity vector (*i.e.*, it is tangential to the orbit) and is therefore often referred to as the **V-bar**. It completes the right-handed coordinate system, such that $\mathbf{x}_{\text{LVLH}} = \mathbf{y}_{\text{LVLH}} \times \mathbf{z}_{\text{LVLH}}$.

- Axis \mathbf{y}_{LVLH} : directed opposite to the orbital angular momentum vector; referred to as the **H-bar**.
- Axis \mathbf{z}_{LVLH} : aligned along the radial direction, from the spacecraft's center of mass toward the center of the Earth; referred to as the **R-bar**.

2.1.3. Spacecraft Body Frame

The frame \mathcal{F}_b is fixed to the spacecraft itself. It moves and rotates along with the spacecraft, making it essential for describing the orientation, dynamics, and control of the spacecraft.

The reference frame consists of:

- Origin O_b : the center of mass of the spacecraft.
- Axes \mathbf{x}_b , \mathbf{y}_b , and \mathbf{z}_b : their orientations depend on the specific mission scenario and will be described in detail in chapter 5.

For the purposes of this study, the body frame is considered to be aligned with the principal inertial directions.

2.2. Cartesian-based Translational Dynamics

This section presents the relative translational dynamical models, employing a Cartesian formulation. The motion is described using position and velocity vectors. Initially, the absolute dynamics of both the chaser and the target satellites are formulated with respect to an inertial frame. Subsequently, the chaser's position and velocity are expressed relative to the target. Finally, by transforming from the inertial frame to a rotating reference frame, the equations of motion of the chaser are derived with respect to the target's local orbital reference frame (LVLH). The equations are obtained by considering the following assumptions:

- Both spacecraft are treated as point masses.
- Only central gravity is considered; perturbations (*e.g.*, J_2 , drag) are neglected.
- The target follows a purely Keplerian (uncontrolled) orbit.
- The relative distance $s = \|\mathbf{r}_c - \mathbf{r}_t\|$ is small compared to the orbital radius: $s \ll r_t$.

2.2.1. Tschauner-Hempel Equations

The two bodies (target and chaser vehicles) are initially modeled as point masses, each subject to the gravitational influence of a central spherical gravity field, as well as forces from thrusters and other disturbances. The gravitational forces acting on the two spacecraft are described by Newton's law of gravitation [1], as shown in Eq. (2.1):

$$\mathbf{F}_g(\mathbf{r}) = -G \frac{Mm}{r^2} \frac{\mathbf{r}}{r} + \mathbf{F}_d = -\mu \frac{m}{r^3} \mathbf{r} \quad (2.1)$$

The equations of motion for the two spacecraft are:

$$m_t \ddot{\mathbf{r}}_t = \mathbf{F}_g(\mathbf{r}_t) + \mathbf{F}_{t,d} + \mathbf{F}_t \quad (2.2)$$

$$m_c \ddot{\mathbf{r}}_c = \mathbf{F}_g(\mathbf{r}_c) + \mathbf{F}_{c,d} + \mathbf{F}_c \quad (2.3)$$

Here, $\mathbf{F}_{t,d}$ and \mathbf{F}_t denote the disturbance and control forces acting on the target, respectively. Similarly, $\mathbf{F}_{c,d}$ and \mathbf{F}_c represent the disturbance and control forces acting on the chaser. In this formulation, the effects of external disturbances are neglected. Additionally, since the target follows a natural (uncontrolled) trajectory, no control input is applied to it. Therefore:

$$\mathbf{F}_{t,d} = \mathbf{F}_{c,d} = \mathbf{F}_t = \mathbf{0} \quad (2.4)$$

Let $\mathbf{s} = \mathbf{r}_c - \mathbf{r}_t$ define the relative position of the chaser with respect to the target's center of mass. The relative acceleration in a non-rotating frame fixed to the target is then given by:

$$\ddot{\mathbf{s}} = \ddot{\mathbf{r}}_c - \ddot{\mathbf{r}}_t = \mathbf{a}_g(\mathbf{r}_c) - \mathbf{a}_g(\mathbf{r}_t) + \frac{\mathbf{F}_c}{m_c} \quad (2.5)$$

Here, $\mathbf{a}_g(\mathbf{r}_c)$ and $\mathbf{a}_g(\mathbf{r}_t)$ represent the gravitational accelerations obtained by dividing the gravitational force by mass. The gravitational acceleration of the chaser is expressed as a Taylor expansion about the target's position \mathbf{r}_t , truncated to first order:

$$\mathbf{a}_g(\mathbf{r}_c) = \mathbf{a}_g(\mathbf{r}_t) + \left. \frac{\partial \mathbf{a}_g(\mathbf{r})}{\partial \mathbf{r}} \right|_{\mathbf{r}=\mathbf{r}_t} (\mathbf{r}_c - \mathbf{r}_t) \quad (2.6)$$

The truncation to first order is justified by the assumption that the distance between the chaser and the target is much smaller than the target's orbital radius, i.e., $s \ll r_t$.

Denoting the Jacobian in Eq. (2.6) as \mathbf{M} , and substituting $\mathbf{s} = \mathbf{r}_c - \mathbf{r}_t$, the relative motion in an inertial frame centered at the target is given by:

$$\ddot{\mathbf{s}} = -\frac{\mu}{r_t^3} \mathbf{Ms} + \frac{\mathbf{F}_c}{m_c} \quad (2.7)$$

To express the motion in the local orbital frame (LVLH) of the target, we apply the transformation from an inertial to a rotating frame:

$$\left\{ \begin{array}{l} \mathbf{A}_{inertial} = T_{rot \rightarrow inertial} \mathbf{A}_{rot} \\ \left(\frac{d\mathbf{A}}{dt} \right)_{inertial} = \left(\frac{d\mathbf{A}}{dt} \right)_{rot} + \boldsymbol{\omega} \times \mathbf{A}_{rot} \\ \left(\frac{d^2\mathbf{A}}{dt^2} \right)_{inertial} = \left(\frac{d^2\mathbf{A}}{dt^2} \right)_{rot} + 2\boldsymbol{\omega} \times \left(\frac{d\mathbf{A}}{dt} \right)_{rot} + \dot{\boldsymbol{\omega}} \times \mathbf{A}_{rot} + \boldsymbol{\omega} \times (\boldsymbol{\omega} \times \mathbf{A}_{rot}) \end{array} \right. \quad (2.8)$$

Substituting Eq. (2.7) into Eq. (2.8), the equations of motion of the chaser in the target's LVLH frame become:

$$\ddot{\mathbf{s}}_{rot} + \boldsymbol{\omega} \times (\boldsymbol{\omega} \times \mathbf{s}_{rot}) + 2\boldsymbol{\omega} \times \dot{\mathbf{s}}_{rot} + \dot{\boldsymbol{\omega}} \times \mathbf{s}_{rot} + \frac{\mu}{r_t^3} \mathbf{M}_{rot} \mathbf{s}_{rot} = \frac{\mathbf{F}_{c,rot}}{m_c} \quad (2.9)$$

The vectors in the LVLH frame are expressed as:

$$\mathbf{s}_{rot} = \begin{bmatrix} x \\ y \\ z \end{bmatrix}, \quad \boldsymbol{\omega} = \begin{bmatrix} 0 \\ -\omega \\ 0 \end{bmatrix}, \quad \mathbf{F}_{c,rot} = \begin{bmatrix} F_x \\ F_y \\ F_z \end{bmatrix}, \quad \mathbf{r}_{t,rot} = \begin{bmatrix} 0 \\ 0 \\ -r_t \end{bmatrix} \quad (2.10)$$

The Jacobian \mathbf{M}_{rot} is evaluated as:

$$\mathbf{M}_{rot} = \left(\frac{d\mathbf{a}_g(\mathbf{r})}{d\mathbf{r}} \right)_{rot} \Big|_{\mathbf{r}_{rot}=\mathbf{r}_{t,rot}} = \begin{bmatrix} 1 & 0 & 0 \\ 0 & 1 & 0 \\ 0 & 0 & -2 \end{bmatrix} \quad (2.11)$$

The individual components of Eq. (2.9) are:

$$\begin{aligned}\boldsymbol{\omega} \times \dot{\mathbf{s}}_{rot} &= \begin{bmatrix} -\omega \dot{z} \\ 0 \\ \omega \dot{x} \end{bmatrix} \\ \dot{\boldsymbol{\omega}} \times \mathbf{s}_{rot} &= \begin{bmatrix} -\dot{\omega} z \\ 0 \\ \dot{\omega} x \end{bmatrix} \\ \boldsymbol{\omega} \times (\boldsymbol{\omega} \times \mathbf{s}_{rot}) &= \begin{bmatrix} -\omega^2 x \\ 0 \\ -\omega^2 z \end{bmatrix} \\ \mathbf{M}_{rot} \mathbf{s}_{rot} &= \begin{bmatrix} x \\ y \\ -2z \end{bmatrix}\end{aligned}\tag{2.12}$$

From conservation of angular momentum, we have $r_t \omega = h$. Define a constant $k = \mu/h^{3/2}$. The Tschauner-Hempel equations are then given by:

$$\left\{ \begin{array}{l} \ddot{x} = -k\omega^{3/2}x + 2\omega\dot{z} + \dot{\omega}z + \omega^2x + \frac{F_x}{m_c} \\ \ddot{y} = -k\omega^{3/2}y + \frac{F_y}{m_c} \\ \ddot{z} = 2k\omega^{3/2}z - 2\omega\dot{x} - \dot{\omega}x + \omega^2z + \frac{F_z}{m_c} \end{array} \right.\tag{2.13}$$

In state-space form, the Tschauner-Hempel equations become:

$$\begin{bmatrix} \dot{x} \\ \dot{y} \\ \dot{z} \\ \ddot{x} \\ \ddot{y} \\ \ddot{z} \end{bmatrix} = \begin{bmatrix} 0 & 0 & 0 & 1 & 0 & 0 \\ 0 & 0 & 0 & 0 & 1 & 0 \\ 0 & 0 & 0 & 0 & 0 & 1 \\ -k\omega^{3/2} + \omega^2 & 0 & \dot{\omega} & 0 & 0 & 2\omega \\ 0 & -k\omega^{3/2} & 0 & 0 & 0 & 0 \\ -\dot{\omega} & 0 & 2k\omega^{3/2} + \omega^2 & -2\omega & 0 & 0 \end{bmatrix} \begin{bmatrix} x \\ y \\ z \\ \dot{x} \\ \dot{y} \\ \dot{z} \end{bmatrix} + \begin{bmatrix} 0 & 0 & 0 \\ 0 & 0 & 0 \\ 0 & 0 & 0 \\ 1 & 0 & 0 \\ 0 & 1 & 0 \\ 0 & 0 & 1 \end{bmatrix} \begin{bmatrix} F_x \\ m_c \\ F_y \\ m_c \\ F_z \\ m_c \end{bmatrix} \quad (2.14)$$

These equations are valid for arbitrary eccentric orbits. The first-order truncation in the Taylor expansion ensures that the model accurately represents the relative motion only when the chaser remains sufficiently close to the target, i.e., $s \ll r_t$. The homogeneous solution follows Keplerian dynamics, while the particular solution depends on the control force.

2.2.2. Hill-Clohessy-Wiltshire Equations

The *Hill-Clohessy-Wiltshire (HCW) equations* are a particular case of the *Tschauner-Hempel equations* applicable to circular orbits. By setting the eccentricity to zero, the angular velocity satisfies $\omega^2 = \mu/r_t^3$. Consequently, Eq. (2.13) reduces to Eq. (2.15):

$$\begin{cases} \ddot{x} = 2\omega\dot{z} + \frac{F_x}{m_c} \\ \ddot{y} = -\omega^2 y + \frac{F_y}{m_c} \\ \ddot{z} = -2\omega\dot{x} + 3\omega^2 z + \frac{F_z}{m_c} \end{cases} \quad (2.15)$$

The *Hill-Clohessy-Wiltshire equations* can also be expressed in state-space form as

$$\dot{\mathbf{x}}(t) = \mathbf{A}\mathbf{x}(t) + \mathbf{B}\mathbf{u}(t),$$

where

$$\begin{bmatrix} \dot{x} \\ \dot{y} \\ \dot{z} \\ \ddot{x} \\ \ddot{y} \\ \ddot{z} \end{bmatrix} = \begin{bmatrix} 0 & 0 & 0 & 1 & 0 & 0 \\ 0 & 0 & 0 & 0 & 1 & 0 \\ 0 & 0 & 0 & 0 & 0 & 1 \\ 0 & 0 & 0 & 0 & 0 & 2n \\ 0 & -n^2 & 0 & 0 & 0 & 0 \\ 0 & 0 & 3n^2 & -2n & 0 & 0 \end{bmatrix} \begin{bmatrix} x \\ y \\ z \\ \dot{x} \\ \dot{y} \\ \dot{z} \end{bmatrix} + \begin{bmatrix} 0 & 0 & 0 \\ 0 & 0 & 0 \\ 0 & 0 & 0 \\ 1 & 0 & 0 \\ 0 & 1 & 0 \\ 0 & 0 & 1 \end{bmatrix} \begin{bmatrix} \frac{F_x}{m_c} \\ \frac{F_y}{m_c} \\ \frac{F_z}{m_c} \end{bmatrix} \quad (2.16)$$

Here, n represents the mean angular velocity. All the considerations discussed for the *Tschauner-Hempel equations* also apply here, with the important distinction that the *Hill-Clohessy-Wiltshire equations* are valid only for circular orbits.

2.2.3. Solutions of HCW Equations

The general solution to these differential equations consists of a homogeneous part plus a particular solution that depends on the external input:

$$\mathbf{x}(t) = \mathbf{x}_h(t) + \mathbf{x}_p(t) = \Phi(t, t_0)\mathbf{x}(t_0) + \int_{t_0}^t \Phi(t, \tau)\mathbf{B}(\tau)\mathbf{u}(\tau) d\tau, \quad (2.17)$$

where $\Phi(t, t_0)$ is the state transition matrix and τ denotes the time integration variable.

Homogeneous solution

The matrix $\Phi(t, t_0)$ is called *State Transition Matrix* and describes the natural motion of the body from the initial to the final time, when it is not subject to external inputs. For LTI systems, like the one of Eq. (2.16), the STM is computed as:

$$\Phi_{LTI}(t, t_0) = e^{\mathbf{A}(t-t_0)} \quad (2.18)$$

This exponential can be easily obtained by means of the Laplace transform applied to the HCW equation in state space form (see Eq.(2.16)).

$$(s\mathbf{I} - \mathbf{A})\mathbf{x}(s) = \mathbf{x}(0_+) + \mathbf{B}\mathbf{u}(s) \quad (2.19)$$

Accordingly, the state-transition matrix (STM) is obtained by applying the inverse transform to the matrix that links the initial state to its natural evolution in the frequency

domain [16]:

$$\Phi(t, t_0) = \mathcal{L}^{-1}\{(s\mathbf{I} - \mathbf{A})^{-1}\} \quad (2.20)$$

Which becomes:

$$\Phi(t, t_0) = \begin{bmatrix} 1 & 0 & 6n\tau - 6\sin(n\tau) & \frac{4\sin(n\tau)-3n\tau}{n} & 0 & \frac{1-2(\cos(n\tau))}{n} \\ 0 & \cos(n\tau) & 0 & 0 & \frac{\sin(n\tau)}{n} & 0 \\ 0 & 0 & 4 - 3\cos(n\tau) & \frac{2(\cos(n\tau)-1)}{n} & 0 & \frac{\sin(n\tau)}{n} \\ 0 & 0 & 6n(1 - \cos(n\tau)) & 4\cos(n\tau) - 3 & 0 & 2\sin(n\tau) \\ 0 & -n\sin(n\tau) & 0 & 0 & \cos(n\tau) & 0 \\ 0 & 0 & 3n\sin(n\tau) & -2\sin(n\tau) & 0 & \cos(n\tau) \end{bmatrix} \quad (2.21)$$

Where $\tau = t - t_0$.

Particular solution

The particular solution of a differential equation for an LTI system is retrieved by substituting the STM in Eq. (2.17) with the corresponding exponential matrix.

$$\mathbf{x}_p = \int_{t_0}^t e^{\mathbf{A}(t-\tau)} \mathbf{B} \mathbf{u}(\tau) d\tau \quad (2.22)$$

This convolution integral has to be computed based on the type of input considered in each specific problem. Especially, this study deals with impulsive and continuous inputs.

- **Impulsive control input:** since the control action is impulsive, the integral will be evaluated across a specific time instant. The STM corresponds to the identity matrix since no propagation is performed, while the input matrix is constant and can be moved outside the integral. Finally, the integral of the control action is the $\Delta\mathbf{v}$ required for the manoeuvre.

$$\mathbf{x}_p = \int_{t_{imp}^-}^{t_{imp}^+} e^{\mathbf{A}(t-\tau)} \mathbf{B} \mathbf{u}(\tau) d\tau = \mathbf{B} \int_{t_{imp}^-}^{t_{imp}^+} \mathbf{u}(\tau) d\tau = \mathbf{B} \Delta\mathbf{v} \quad (2.23)$$

Due to the structure of the input matrix, we can notice that the $\Delta\mathbf{v}$ represents the

velocity variation across the impulse.

$$\mathbf{x}_p = \begin{bmatrix} \mathbf{r} \\ \dot{\mathbf{r}} \end{bmatrix} = \begin{bmatrix} \mathbf{0} \\ \Delta \mathbf{v} \end{bmatrix} \quad (2.24)$$

- **Continuous control input:** in the case of continuous control input, the full integral has to be computed.

$$\mathbf{x}_p = \int_{t_0}^t \Phi(t, \tau) \mathbf{B} \mathbf{u}(\tau) d\tau \quad (2.25)$$

This operation can be simplified by a numerical approximation of the integral:

$$\mathbf{x}_p = \sum_{n=1}^{N-1} \Phi(t_{n+1}, t_n) \mathbf{B} \mathbf{u}(t_n) \Delta t \quad (2.26)$$

2.2.4. Solutions of TH Equations

The dynamics of relative motion in an eccentric orbit are governed by a linear time-varying (LTV) system as outlined in Eq. (2.14). In this formulation, the system matrix $\mathbf{A}(t)$ varies with time due to the eccentric nature of the orbit, while the input matrix \mathbf{B} remains constant. Although the general solution maintains the same structure as in Eq. (2.17), it cannot be derived through a matrix exponential, as is done for linear time-invariant systems.

Homogeneous Solution

For LTV systems, the homogeneous solution cannot be obtained using the exponential of a constant matrix. Instead, the concept of a *fundamental matrix* $\mathcal{X}(t)$ becomes essential (see Ref. [36, 43] for a more in-depth analysis). This matrix is constructed from a complete set of six linearly independent solutions to the system. Each solution vector $\mathbf{x}_i(t)$ forms a column of $\mathcal{X}(t)$, capturing the full state space of the solution:

$$\mathcal{X}(t) = \begin{bmatrix} \mathbf{x}_1(t) & \mathbf{x}_2(t) & \cdots & \mathbf{x}_6(t) \end{bmatrix}. \quad (2.27)$$

Any general solution $\mathbf{x}(t)$ of the homogeneous system can then be expressed as a linear combination of these basis vectors:

$$\mathbf{x}(t) = \mathcal{X}(t)\mathbf{c}, \quad (2.28)$$

where \mathbf{c} is a constant vector determined by the initial condition. At the reference time t_0 , the system state satisfies:

$$\mathbf{x}(t_0) = \mathcal{X}(t_0)\mathbf{c}. \quad (2.29)$$

Assuming that $\mathcal{X}(t_0)$ is invertible, guaranteed by the linear independence of its columns, the coefficient vector is computed as:

$$\mathbf{c} = \mathcal{X}^{-1}(t_0)\mathbf{x}(t_0). \quad (2.30)$$

Substituting Eq. (2.30) into Eq. (2.28), the state evolution is described by:

$$\mathbf{x}(t) = \mathcal{X}(t)\mathcal{X}^{-1}(t_0)\mathbf{x}(t_0). \quad (2.31)$$

Comparing with the definition of the state transition matrix (STM) $\Phi(t, t_0)$:

$$\mathbf{x}(t) = \Phi(t, t_0)\mathbf{x}(t_0), \quad (2.32)$$

we identify:

$$\Phi(t, t_0) = \mathcal{X}(t)\mathcal{X}^{-1}(t_0). \quad (2.33)$$

This formulation offers a tractable method for evaluating the STM in LTV systems by utilizing known solutions. Specifically, in the context of eccentric orbit rendezvous modeled by Eq. (2.14), an analytical fundamental matrix was proposed by Yamanaka and Ankersen [36, 48]:

$$\begin{aligned}\mathcal{X}_{\text{in}}(t) &= \begin{bmatrix} 1 & -\cos \nu(1 + \rho) & \sin \nu(1 + \rho) & 3\rho^2 J \\ 0 & \rho \sin \nu & \rho \cos \nu & 2 - 3e\rho \sin \nu J \\ 0 & 2\rho \sin \nu & 2\rho \cos \nu - e & 3 - 6e\rho \sin \nu J \\ 0 & \rho \cos \nu - e \sin^2 \nu & -\sin \nu(2\rho - 1) & -3e \left(\frac{\sin \nu}{\rho} + (\rho \cos \nu - e \sin^2 \nu) J \right) \end{bmatrix}, \\ \mathcal{X}_{\text{out}}(t) &= \begin{bmatrix} \cos \nu & \sin \nu \\ -\sin \nu & \cos \nu \end{bmatrix}\end{aligned}\tag{2.34}$$

Here, ν denotes the true anomaly, e the eccentricity, and $\rho = 1 + e \cos \nu$, while $J(\nu)$ represents the scaled time integral of motion, given by $J(\nu) = \frac{\omega}{\rho^2}(t - t_0)$.

Particular Solution

The particular solution arising from external control inputs, either impulsive or continuous, can be treated analogously to the circular orbit case, as discussed in Section 2.2.3.

2.3. ROE-based Translational Dynamics

In the context of satellite dynamics, orbital elements, particularly the Keplerian set, often offer more intuitive insights than Cartesian coordinates. These elements are especially advantageous when the focus lies on the geometry, shape, or long-term evolution of an orbit rather than on instantaneous position and velocity data. This same rationale extends to the analysis of the relative motion between spacecraft. Rather than relying solely on Cartesian representations of relative position and velocity, an alternative formulation based on orbital elements can be more insightful and practically useful. This chapter introduces the concept of *Relative Orbital Elements* (ROEs) and demonstrates how the traditional Cartesian framework for relative motion can be transformed into an ROE-based formulation. The equations are derived by considering the same assumptions of Section 2.2. The following expressions define classical orbital parameters for a two-body

Keplerian orbit, in terms of the semi-major axis a , eccentricity e , true anomaly ν , and standard gravitational parameter μ : the semi-latus rectum p , the semi-minor axis b , the radial distance r , the eccentricity function η , the mean motion n , the specific angular momentum h , and the orbital speed v .

$$\begin{aligned} p &= a(1 - e^2), \quad b = a\sqrt{1 - e^2}, \quad r = \frac{a(1 - e^2)}{1 + e \cos \nu}, \quad \eta = \sqrt{1 - e^2} \\ n &= \sqrt{\frac{\mu}{a^3}}, \quad h = \sqrt{\mu a(1 - e^2)}, \quad v = \sqrt{\frac{2\mu(1 + e \cos \nu)}{a(1 - e^2)} - \frac{\mu}{a}} \end{aligned} \tag{2.35}$$

2.3.1. The Relative Orbital Elements

Relative Orbital Elements (ROEs) are defined as the difference between the absolute orbital elements of the chaser spacecraft and those of the target. Given the classical Keplerian element vector, defined by the semi-major axis a , eccentricity e , inclination i , right ascension of the ascending node (RAAN) Ω , argument of pericenter ω , and mean anomaly M ,

$$\boldsymbol{\alpha}_{kep} = [a \ e \ i \ \Omega \ \omega \ M]^\top,$$

the Keplerian ROEs are defined as:

$$\delta\boldsymbol{\alpha}_{kep} = \Delta\boldsymbol{\alpha}_{kep} = \begin{bmatrix} \delta a \\ \delta e \\ \delta i \\ \delta \Omega \\ \delta \omega \\ \delta M \end{bmatrix} = \begin{bmatrix} a_c - a_t \\ e_c - e_t \\ i_c - i_t \\ \Omega_c - \Omega_t \\ \omega_c - \omega_t \\ M_c - M_t \end{bmatrix}, \tag{2.36}$$

where subscripts c and t denote chaser and target respectively.

However, this Keplerian formulation becomes singular for circular ($e_t = 0$) or equatorial ($i_t = 0^\circ$) target orbits. To address this issue, a quasi-nonsingular (qns) set of orbital

elements is introduced, which avoids singularities associated with circular orbits:

$$\delta\boldsymbol{\alpha}_{qns} = \begin{bmatrix} \delta a/a_t \\ \delta\lambda \\ \delta e_x \\ \delta e_y \\ \delta i_x \\ \delta i_y \end{bmatrix} = \begin{bmatrix} \frac{a_c - a_t}{a_t} \\ (M_c + \omega_c) - (M_t + \omega_t) + (\Omega_c - \Omega_t) \cos i_t \\ e_c \cos \omega_c - e_t \cos \omega_t \\ e_c \sin \omega_c - e_t \sin \omega_t \\ i_c - i_t \\ (\Omega_c - \Omega_t) \sin i_t \end{bmatrix}. \quad (2.37)$$

The term $\delta\lambda$ is referred to as the relative mean argument of longitude, whereas $\mathbf{e} = [e_x, e_y]^\top$ and $\mathbf{i} = [i_x, i_y]^\top$ represent the relative eccentricity vector and the relative inclination vector, respectively. This formulation eliminates the singularity at zero eccentricity while retaining a singularity for equatorial orbits. Many Low Earth Orbit (LEO) missions operate in nearly circular orbits that are not equatorial. In contrast, Geostationary Earth Orbits (GEO) are equatorial. As a result, certain formulations may be less suitable when applied to equatorial orbits. In this study, we focus specifically on non-equatorial orbits, which justifies the choice of the adopted orbital elements formulation.

The time derivatives of the two sets of ROEs are defined as:

$$\delta\dot{\boldsymbol{\alpha}}_{kep} = \begin{bmatrix} \delta\dot{a} \\ \delta\dot{e} \\ \delta\dot{i} \\ \delta\dot{\Omega} \\ \delta\dot{\omega} \\ \delta\dot{M} \end{bmatrix} = \begin{bmatrix} \dot{a}_c - \dot{a}_t \\ \dot{e}_c - \dot{e}_t \\ \dot{i}_c - \dot{i}_t \\ \dot{\Omega}_c - \dot{\Omega}_t \\ \dot{\omega}_c - \dot{\omega}_t \\ \dot{M}_c - \dot{M}_t \end{bmatrix}, \quad (2.38)$$

$$\begin{aligned} \delta\dot{\alpha}_{qns} &= \begin{bmatrix} \delta\ddot{a}/a_t - \dot{a}_t\delta a/a_t^2 \\ \delta\dot{\lambda} \\ \delta\dot{e}_x \\ \delta\dot{e}_y \\ \delta\dot{i}_x \\ \delta\dot{i}_y \end{bmatrix} = \\ &= \begin{bmatrix} (\dot{a}_c - \dot{a}_t)/a_t - \dot{a}_t(a_c - a_t)/a_t^2 \\ (\dot{M}_c + \dot{\omega}_c) - (\dot{M}_t + \dot{\omega}_t) + (\dot{\Omega}_c - \dot{\Omega}_t)\cos i_t - \dot{i}_t(\Omega_c - \Omega_t)\sin i_t \\ (\dot{e}_c \cos \omega_c - \dot{e}_t \cos \omega_t) - (\dot{\omega}_c e_c \sin \omega_c - \dot{\omega}_t e_t \sin \omega_t) \\ (\dot{e}_c \sin \omega_c - \dot{e}_t \sin \omega_t) + (\dot{\omega}_c e_c \cos \omega_c - \dot{\omega}_t e_t \cos \omega_t) \\ \dot{i}_c - \dot{i}_t \\ (\dot{\Omega}_c - \dot{\Omega}_t)\sin i_t + \dot{i}_t(\Omega_c - \Omega_t)\cos i_t \end{bmatrix} \end{aligned} \quad (2.39)$$

The transformation from the Keplerian elements to the quasi-nonsingular (qns) set can be linearized by applying a first-order Taylor expansion of the chaser's qns vector around the target's Keplerian orbital elements:

$$\alpha_{qns,c} = \alpha_{qns,t} + \frac{\partial \alpha_{qns,c}}{\partial \alpha_{kep,c}} \Big|_{\alpha_{kep,c}=\alpha_{kep,t}} (\alpha_{kep,c} - \alpha_{kep,t}) \quad (2.40)$$

Defining the Jacobian matrix as $\mathbf{T}_{kep \rightarrow qns}$, Eq. (2.40) can be expressed more compactly as:

$$\delta\alpha_{qns} = \mathbf{T}_{kep \rightarrow qns} \delta\alpha_{kep}, \quad (2.41)$$

where $\delta\alpha_{qns} = \alpha_{qns,c} - \alpha_{qns,t}$ and $\delta\alpha_{kep} = \alpha_{kep,c} - \alpha_{kep,t}$.

Taking the time derivative of the above yields:

$$\dot{\delta}\alpha_{qns} = \dot{\mathbf{T}}_{kep \rightarrow qns} \delta\alpha_{kep} + \mathbf{T}_{kep \rightarrow qns} \delta\dot{\alpha}_{kep}. \quad (2.42)$$

The transformation matrix $\mathbf{T}_{kep \rightarrow qns}$ is obtained from the Jacobian of Eq. (2.40) and is given by:

$$\mathbf{T}_{kep \rightarrow qns} = \begin{bmatrix} \frac{1}{a_t} & 0 & 0 & 0 & 0 & 0 \\ 0 & 0 & 0 & \cos i_t & 1 & 1 \\ 0 & \cos \omega_t & 0 & 0 & -e_t \sin \omega_t & 0 \\ 0 & \sin \omega_t & 0 & 0 & e_t \cos \omega_t & 0 \\ 0 & 0 & 1 & 0 & 0 & 0 \\ 0 & 0 & 0 & \sin i_t & 0 & 0 \end{bmatrix}. \quad (2.43)$$

Its time derivative is expressed as:

$$\dot{\mathbf{T}}_{kep \rightarrow qns} = \begin{bmatrix} -\frac{\dot{a}_t}{a_t^2} & 0 & 0 & 0 & 0 & 0 \\ 0 & 0 & 0 & -\dot{i}_t \sin i_t & 0 & 0 \\ 0 & -\dot{\omega}_t \sin \omega_t & 0 & 0 & -\dot{e}_t \sin \omega_t - e_t \dot{\omega}_t \cos \omega_t & 0 \\ 0 & \dot{\omega}_t \cos \omega_t & 0 & 0 & \dot{e}_t \cos \omega_t - e_t \dot{\omega}_t \sin \omega_t & 0 \\ 0 & 0 & 0 & 0 & 0 & 0 \\ 0 & 0 & 0 & \dot{i}_t \cos i_t & 0 & 0 \end{bmatrix}. \quad (2.44)$$

2.3.2. The ROE Equations

The equations of motion using the quasi-nonsingular ROE (qns-ROE) representation are derived under the same assumptions outlined in Section 2.2. Accordingly, external disturbances acting on both vehicles are neglected, and the target is assumed to follow its natural, uncontrolled trajectory. Therefore, the target's dynamics are governed by pure Keplerian motion, while the motion of the chaser is described by the *Gauss Planetary Equations* [26]:

$$\dot{\boldsymbol{\alpha}}_{\text{kep},t} = \begin{bmatrix} \dot{a}_t \\ \dot{e}_t \\ \dot{i}_t \\ \dot{\Omega}_t \\ \dot{\omega}_t \\ \dot{M}_t \end{bmatrix} = \begin{bmatrix} 0 \\ 0 \\ 0 \\ 0 \\ 0 \\ \sqrt{\mu} a_t^{-3/2} \end{bmatrix}$$

$$\dot{\boldsymbol{\alpha}}_{\text{kep},c} = \begin{bmatrix} \dot{a}_c \\ \dot{e}_c \\ \dot{i}_c \\ \dot{\Omega}_c \\ \dot{\omega}_c \\ \dot{M}_c \end{bmatrix} = \begin{bmatrix} \frac{2a_c^2}{h} \left(-e_c \sin \nu_c u_z + \frac{p}{r} u_x \right) \\ \frac{1}{h} \left(-p \sin \nu_c u_z + ((p+r) \cos \nu_c + r e_c) u_x \right) \\ -\frac{r \cos(\nu_c + \omega_c)}{h} u_y \\ -\frac{r \sin(\nu_c + \omega_c)}{h \sin i_c} u_y \\ \frac{1}{h e_c} (p \cos \nu_c u_z + (p+r) \sin \nu_c u_x) \\ \sqrt{\mu} a_c^{-3/2} + \frac{b}{a_c h e_c} (-p \cos \nu_c - 2r e_c) u_z - (p+r) \sin \nu_c u_x \end{bmatrix} \quad (2.45)$$

The parameters h , p , r , and b are defined in terms of the chaser's Keplerian orbital elements, as shown in Eq. (2.35). The control acceleration vector in the target's LVLH (Local-Vertical Local-Horizontal) reference frame is defined as:

$$\mathbf{u}_t = \frac{\mathbf{F}_{t,\text{rot}}}{m_t} = \mathbf{0}, \quad \mathbf{u}_c = \frac{\mathbf{F}_{c,\text{rot}}}{m_c} \quad (2.46)$$

Here \mathbf{F}_{rot} expresses the control force in the rotating (LVLH) reference frame as done in Section 2.2.4. The chaser's absolute dynamics can be linearized around the target's orbital elements. By taking a first-order Taylor expansion and assuming that the relative distance s is much smaller than the target's orbital radius ($s \ll r_t$), we obtain the linearized dynamics:

$$\dot{\boldsymbol{\alpha}}_c \approx \dot{\boldsymbol{\alpha}}_t + \frac{\partial \dot{\boldsymbol{\alpha}}_c}{\partial \boldsymbol{\alpha}_c} \Big|_{\substack{\boldsymbol{\alpha}_c = \boldsymbol{\alpha}_t \\ \mathbf{u}_c = \mathbf{u}_t}} (\boldsymbol{\alpha}_c - \boldsymbol{\alpha}_t) + \frac{\partial \dot{\boldsymbol{\alpha}}_c}{\partial \mathbf{u}_c} \Big|_{\substack{\boldsymbol{\alpha}_c = \boldsymbol{\alpha}_t \\ \mathbf{u}_c = \mathbf{u}_t}} (\mathbf{u}_c - \mathbf{u}_t) \quad (2.47)$$

We first examine the Jacobian $\partial \dot{\boldsymbol{\alpha}}_c / \partial \boldsymbol{\alpha}_c$, which can be separated into homogeneous ' h '

and particular ' p ' components:

$$\frac{\partial \dot{\alpha}_c}{\partial \alpha_c} \Big|_{\substack{\alpha_c = \alpha_t \\ \mathbf{u}_c = \mathbf{u}_t}} = \frac{\partial \dot{\alpha}_{c,h}}{\partial \alpha_{c,h}} \Big|_{\alpha_c = \alpha_t} + \frac{\partial \dot{\alpha}_{c,p}}{\partial \alpha_{c,p}} \Big|_{\mathbf{u}_c = \mathbf{u}_t} \quad (2.48)$$

Based on the assumptions of Section 2.2 and Eq. (2.45), the particular component is zero due to $\mathbf{u}_t = \mathbf{0}$. The homogeneous part, originating from the Keplerian motion, varies only in the mean anomaly, hence:

$$\frac{\partial \dot{\alpha}_{\text{kep},c}}{\partial \alpha_{\text{kep},c}} \Big|_{\substack{\alpha_{\text{kep},c} = \alpha_{\text{kep},t} \\ \mathbf{u}_c = \mathbf{u}_t}} = \begin{bmatrix} 0 & 0 & 0 & 0 & 0 & 0 \\ 0 & 0 & 0 & 0 & 0 & 0 \\ 0 & 0 & 0 & 0 & 0 & 0 \\ 0 & 0 & 0 & 0 & 0 & 0 \\ 0 & 0 & 0 & 0 & 0 & 0 \\ -1.5\sqrt{\mu}a_t^{-5/2} & 0 & 0 & 0 & 0 & 0 \end{bmatrix} \quad (2.49)$$

Next, we analyze the Jacobian $\partial \dot{\alpha}_c / \partial \mathbf{u}_c$. Since the system is linear in the control input, this Jacobian is constant with respect to \mathbf{u}_c :

$$\frac{\partial \dot{\alpha}_{\text{kep},c}}{\partial \mathbf{u}_c} \Big|_{\substack{\alpha_{\text{kep},c} = \alpha_{\text{kep},t} \\ \mathbf{u}_c = \mathbf{u}_t}} = \begin{bmatrix} \frac{2a_t^2 p}{h r} & 0 & -\frac{2a_t^2}{h} e_c \sin(\nu_c) \\ \frac{1}{h} ((p+r) \cos(\nu_c) + r e_t) & 0 & -\frac{1}{h} p \sin(\nu_t) \\ 0 & -\frac{r \cos(\nu_t + \omega_t)}{h} & 0 \\ 0 & -\frac{r \sin(\nu_t + \omega_t)}{h \sin(i_t)} & 0 \\ \frac{1}{h e_t} (p+r) \sin(\nu_t) & 0 & \frac{1}{h e_t} p \cos(\nu_t) \\ -\frac{b}{a_t h e_t} (p+r) \sin(\nu_t) & 0 & -\frac{b}{a_t h e_c} (p \cos(\nu_t) - 2r e_t) \end{bmatrix} \quad (2.50)$$

Let \mathbf{A}_{kep} and \mathbf{B}_{kep} denote the Jacobians in Eqs. (2.49) and (2.50), respectively. The linearized chaser dynamics in terms of Keplerian elements is:

$$\dot{\alpha}_{\text{kep},c} \approx \dot{\alpha}_{\text{kep},t} + \mathbf{A}_{\text{kep}} \delta\alpha_{\text{kep}} + \mathbf{B}_{\text{kep}} \mathbf{u}_c \quad (2.51)$$

Consequently, the relative motion equations in Keplerian elements are:

$$\delta\dot{\alpha}_{\text{kep}} = \Delta\dot{\alpha}_{\text{kep}} = \mathbf{A}_{\text{kep}} \delta\alpha_{\text{kep}} + \mathbf{B}_{\text{kep}} \mathbf{u}_c \quad (2.52)$$

Transforming to the quasi-nonsingular set (see Eq.(2.42)) and noticing that $\dot{\mathbf{T}}_{\text{kep} \rightarrow \text{qns}} = \mathbf{0}$ when substituting the target components from Eq.(2.45), gives:

$$\delta\dot{\alpha}_{\text{qns}} = \mathbf{T}_{\text{kep} \rightarrow \text{qns}} \mathbf{A}_{\text{kep}} \mathbf{T}_{\text{kep} \rightarrow \text{qns}}^{-1} \delta\alpha_{\text{qns}} + \mathbf{T}_{\text{kep} \rightarrow \text{qns}} \mathbf{B}_{\text{kep}} \mathbf{u}_c \quad (2.53)$$

The final state-space form is:

$$\begin{aligned} \delta\dot{\alpha}_{\text{qns}}(t) &= \mathbf{A} \delta\alpha_{\text{qns}}(t) + \mathbf{B}(t) \mathbf{u}_c \\ \mathbf{A} &= \begin{bmatrix} 0 & 0 & 0 & 0 & 0 & 0 \\ -1.5n & 0 & 0 & 0 & 0 & 0 \\ 0 & 0 & 0 & 0 & 0 & 0 \\ 0 & 0 & 0 & 0 & 0 & 0 \\ 0 & 0 & 0 & 0 & 0 & 0 \\ 0 & 0 & 0 & 0 & 0 & 0 \end{bmatrix} \\ \mathbf{B}(t) &= \frac{1}{an} \begin{bmatrix} 2\frac{e \cos(\nu)+1}{\eta} & 0 & -2e\frac{\sin(\nu)}{\eta} \\ -\frac{\eta \sin(\nu)(\eta-1)(e \cos(\nu)+2)}{e(e \cos(\nu)+1)} & 0 & \frac{\eta \cos(\nu)-\eta^2 \left(\cos(\nu)-\frac{2e}{e \cos(\nu)+1}\right)}{e} \\ \frac{\eta[(2+e \cos \nu) \cos \theta+e_x]}{e \cos \nu+1} & -\frac{e \eta \sin (\theta) e_y}{(e \cos (\nu)+1) \tan (i)} & -\eta \sin (\theta) \\ \frac{\eta[(2+e \cos \nu) \sin \theta+e_y]}{e \cos (\nu)+1} & \frac{e \eta \sin (\theta) e_x}{(e \cos (\nu)+1) \tan (i)} & \eta \cos (\theta) \\ 0 & -\frac{\eta \cos (\theta)}{e \cos (\nu)+1} & 0 \\ 0 & -\frac{\eta \sin (\theta)}{e \cos (\nu)+1} & 0 \end{bmatrix} \end{aligned} \quad (2.54)$$

Here, $\theta = \nu + \omega$ is the true argument of latitude. The input matrix $\mathbf{B}(t)$ corresponds to the one defined in Ref. [37], with two key differences: the reference frame is changed from

RTN (Radial–Transverse–Normal) to LVLH (Local Vertical Local Horizontal), and the second row differs due to the use, in Ref. [37], of a *modified* mean argument of longitude as the second element of the state vector. In the circular case ($e \rightarrow 0$), the input matrix reduces to:

$$\mathbf{B}(t) = \frac{1}{an} \begin{bmatrix} 2 & 0 & 0 \\ 0 & 0 & 2 \\ 2\cos u & 0 & -\sin u \\ 2\sin u & 0 & \cos u \\ 0 & -\cos u & 0 \\ 0 & -\sin u & 0 \end{bmatrix} \quad (2.55)$$

Where $u = M + \omega$ is the mean argument of latitude. We can observe that:

- The system is linear time-varying (LTV);
- The state matrix \mathbf{A} is time-invariant, enabling computation of the homogeneous solution using the matrix exponential;
- The input matrix $\mathbf{B}(t)$ is time-dependent.

2.3.3. Solutions of ROE Equations

Homogeneous Solution

The qns-ROE set offers an easy way to compute the State transition matrix. Since the plant matrix is time-invariant, the STM can be retrieved from the exponential matrix:

$$\Phi(t, t_0) = e^{\mathbf{A}(t-t_0)} = \sum_{n=0}^{\infty} \mathbf{A}^n \frac{(t-t_0)^n}{n!} \quad (2.56)$$

Due to the sparsity of the plant matrix, the components $\mathbf{A}^2, \dots, \mathbf{A}^\infty$ are zero. Therefore, the STM is given by:

$$\Phi(t, t_0) = \mathbf{I} + \mathbf{A}(t-t_0) = \begin{bmatrix} 1 & 0 & 0 & 0 & 0 & 0 \\ -1.5n(t-t_0) & 1 & 0 & 0 & 0 & 0 \\ 0 & 0 & 1 & 0 & 0 & 0 \\ 0 & 0 & 0 & 1 & 0 & 0 \\ 0 & 0 & 0 & 0 & 1 & 0 \\ 0 & 0 & 0 & 0 & 0 & 1 \end{bmatrix} \quad (2.57)$$

Particular Solution

The particular solution depends on the nature of the control input applied to the chaser's dynamics and is given by:

$$\delta\boldsymbol{\alpha}_{qns,p}(t) = \int_{t_0}^t e^{\mathbf{A}(t-\tau)} \mathbf{B}(\tau) \mathbf{u}_c(\tau) d\tau \quad (2.58)$$

This expression accounts for the time-dependent nature of the input matrix $\mathbf{B}(t)$, which differentiates it from the corresponding formulation in section 2.2.

The particular solution is computed differently depending on whether the control input is impulsive or continuous:

- **Impulsive Input:**

$$\delta\boldsymbol{\alpha}_{qns,p} = \int_{t_{\text{imp}}^-}^{t_{\text{imp}}^+} e^{\mathbf{A}(t-\tau)} \mathbf{B}(\tau) \mathbf{u}(\tau) d\tau = \mathbf{B}(t_{\text{imp}}) \Delta \mathbf{v} \quad (2.59)$$

- **Continuous Input:**

$$\delta\boldsymbol{\alpha}_{qns,p} = \sum_{n=1}^{N-1} \Phi(t_{n+1}, t_n) \mathbf{B}(t_n) \mathbf{u}(t_n) \Delta t \quad (2.60)$$

2.3.4. ROE-TH Framework for Keplerian Motion

This section is inspired by Ref. [21], where the ROE-HCW is presented for near-circular orbits where the eccentricity is considered to be zero. Here, the extension to the eccentric case by means of the Tschauner-Hempel (TH) equations is provided. The procedure starts by defining the transformation matrix from Cartesian state to qns-ROEs. Ref. [36] provides the transformation matrix from Cartesian state to Keplerian ROEs, which will be employed as an intermediate trasformation together with the transformation matrix from Keplerian ROEs to qns-ROEs of Eq.(2.43) in order to get the final result.

$$\mathbf{T}_{car \rightarrow qns} = \mathbf{T}_{kep \rightarrow qns} \mathbf{T}_{car \rightarrow kep} \quad (2.61)$$

The matrix components can be found in Appendix A. When the eccentricity tends to zero ($e \rightarrow 0$), the transformation matrix tends to the result shown in Ref. [21] for the

ROE-HCW framework:

$$\mathbf{T}_{car \rightarrow qns}(t) = \frac{1}{a} \begin{bmatrix} 0 & 0 & -4 & \frac{2}{n} & 0 & 0 \\ 1 & 0 & 0 & 0 & 0 & \frac{2}{n} \\ 0 & 0 & -3\cos(u) & \frac{2\cos(u)}{n} & 0 & -\frac{\sin(u)}{n} \\ 0 & 0 & -3\sin(u) & \frac{2\sin(u)}{n} & 0 & \frac{\cos(u)}{n} \\ 0 & -\sin(u) & 0 & 0 & -\frac{\cos(u)}{n} & 0 \\ 0 & \cos(u) & 0 & 0 & -\frac{\sin(u)}{n} & 0 \end{bmatrix} \quad (2.62)$$

Finally, the equations of motion and their solutions can be transformed from one set to the other by means of the following transformations:

$$\begin{aligned} \mathbf{A}_{car}(t) &= \mathbf{T}_{car \rightarrow qns}^{-1}(t) \mathbf{A}_{qns} \mathbf{T}_{car \rightarrow qns}(t) - \mathbf{T}_{car \rightarrow qns}^{-1}(t) \dot{\mathbf{T}}_{car \rightarrow qns}(t) \\ \mathbf{B}_{car} &= \mathbf{T}_{car \rightarrow qns}^{-1}(t) \mathbf{B}_{qns}(t) \\ \Phi_{car}(t, t_0) &= \mathbf{T}_{car \rightarrow qns}^{-1}(t) \Phi_{qns}(t, t_0) \mathbf{T}_{car \rightarrow qns}(t) \end{aligned} \quad (2.63)$$

And the opposite transformation:

$$\begin{aligned} \mathbf{A}_{qns} &= \mathbf{T}_{car \rightarrow qns}(t) \mathbf{A}_{qns}(t) \mathbf{T}_{car \rightarrow qns}^{-1}(t) + \dot{\mathbf{T}}_{car \rightarrow qns}(t) \mathbf{T}_{car \rightarrow qns}^{-1}(t) \\ \mathbf{B}_{qns}(t) &= \mathbf{T}_{car \rightarrow qns}(t) \mathbf{B}_{car} \\ \Phi_{qns}(t, t_0) &= \mathbf{T}_{car \rightarrow qns}(t) \Phi_{qns}(t, t_0) \mathbf{T}_{car \rightarrow qns}^{-1}(t) \end{aligned} \quad (2.64)$$

The transformation matrix $\mathbf{T}_{car \rightarrow qns}(t)$ exhibits time dependence as it converts the *time-dependent plant matrix* of the Cartesian dynamics into a *time-invariant plant matrix* in the ROE domain. Conversely, it maps the *time-dependent input matrix* in the ROE formulation into a *constant input matrix* in the Cartesian representation.

2.4. Rotational Motion

In this study, the rotational dynamics will be analyzed with the aim of controlling the attitude of the chaser during the final approach of a rendezvous mission. A simplified formulation of the relative attitude dynamics will be employed, based on the following assumptions:

- The target vehicle is able to maintain a fixed attitude with respect to its LVLH (Local-Vertical, Local-Horizontal) frame. Therefore, the Direction Cosine Matrix (DCM) that describes the rotation from the target's LVLH frame to its body frame remains constant over time.
- The target vehicle rotates with the angular velocity of its LVLH frame.
- External disturbances are neglected in the equations of motion.
- The body frame is aligned with the principal axes of inertia.

2.4.1. Absolute Dynamics and Kinematics

The matrix that represents the rotation from a frame b to a frame a is called direction cosine matrix and will be denoted as $\mathbf{A}_{a/b}$. Therefore, the rotation of a generic vector \mathbf{v} from one frame to the other is:

$$\mathbf{v}_a = \mathbf{A}_{a/b} \mathbf{v}_b \quad (2.65)$$

The direction cosine matrix can be expressed by means of the Euler's angles; if θ_x , θ_y , θ_z are the rotations around the axis x , y , z respectively, for a set of rotations 321 we can define:

$$\mathbf{A}_{a/b}(\boldsymbol{\theta}) = \begin{bmatrix} \cos \theta_y \cos \theta_z & \cos \theta_y \sin \theta_z & -\sin \theta_y \\ \sin \theta_x \sin \theta_y \cos \theta_z - \cos \theta_x \sin \theta_z & \sin \theta_x \sin \theta_y \sin \theta_z + \cos \theta_x \cos \theta_z & \sin \theta_x \cos \theta_y \\ \cos \theta_x \sin \theta_y \cos \theta_z + \sin \theta_x \sin \theta_z & \cos \theta_x \sin \theta_y \sin \theta_z - \sin \theta_x \cos \theta_z & \cos \theta_x \cos \theta_y \end{bmatrix} \quad (2.66)$$

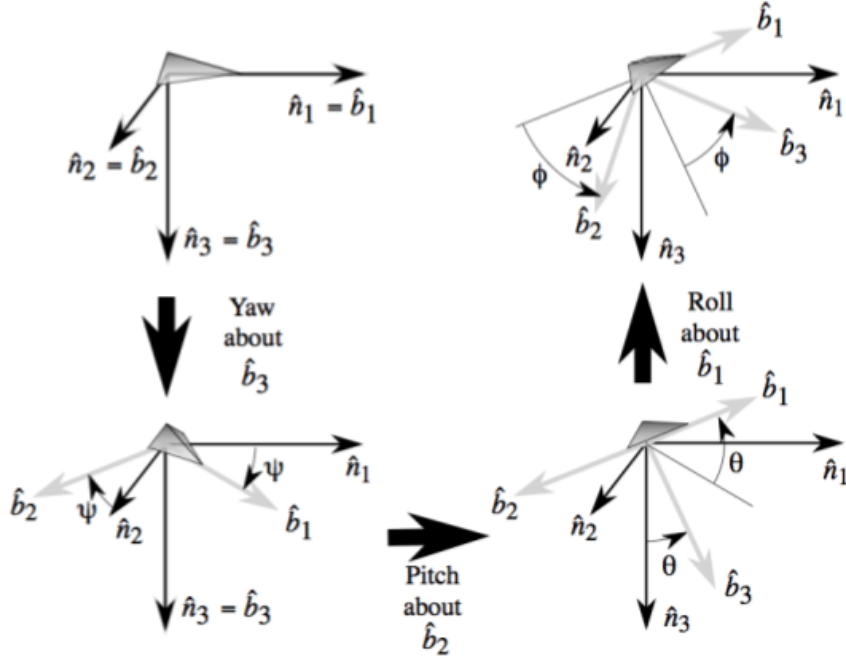


Figure 2.3: 321 rotation set (from Ref. [18])

We can define the angular velocity of the body frame as:

$$\begin{aligned}\omega_B^B &= \omega_{B/N}^B + \omega_N^B = \omega_{B/N}^B + \mathbf{A}_{B/N}\omega_N^N \\ \omega_N^N &= \mathbf{0} \Rightarrow \omega_B^B = \omega_{B/N}^B\end{aligned}\quad (2.67)$$

Here, the subscript indicates the reference frame to which the angular velocity refers, while the superscript specifies the frame in which the angular velocity is expressed. For example, ω_N^B denotes the angular velocity of the inertial frame expressed in the body frame. $\omega_{B/N}^B$ is the relative angular velocity between the inertial and the body frame, expressed in the body frame. Since the inertial frame is a fixed frame, its angular velocity is zero. For simplicity ω_B^B will be denoted as ω_B . Moreover, the relative angular velocity between two rotating frames is:

$$\omega_{a/b}^a = \omega_a^a - \mathbf{A}_{a/b}\omega_b^b \quad (2.68)$$

We can define the time variation of the angular velocity of the body frame through Euler's equations:

$$\mathbf{I} \frac{d\omega_B}{dt} + \omega_B \times (\mathbf{I}\omega_B) = \mathbf{M} \quad (2.69)$$

Here, \mathbf{I} is the inertia tensor in the body frame and \mathbf{M} is the external moment (torque)

applied to the body. If the body-fixed frame is aligned with the principal axes of inertia, the Euler's equations become:

$$\begin{aligned}\dot{\omega}_x &= \frac{(I_y - I_z)}{I_x} \omega_y \omega_z + \frac{M_x}{I_x} \\ \dot{\omega}_y &= \frac{(I_z - I_x)}{I_y} \omega_x \omega_z + \frac{M_y}{I_y} \\ \dot{\omega}_z &= \frac{(I_x - I_y)}{I_z} \omega_x \omega_y + \frac{M_z}{I_z}\end{aligned}\quad (2.70)$$

The Euler's angles kinematics for the set of rotations of Eq.(2.66) is:

$$\begin{bmatrix} \dot{\theta}_x \\ \dot{\theta}_y \\ \dot{\theta}_z \end{bmatrix} = \begin{bmatrix} 1 & \sin \theta_x \tan \theta_y & \cos \theta_x \tan \theta_y \\ 0 & \cos \theta_x & -\sin \theta_x \\ 0 & \sin \theta_x / \cos \theta_y & \cos \theta_x / \cos \theta_y \end{bmatrix} \boldsymbol{\omega}_{a/b}^a \quad (2.71)$$

Eq.(2.69) and Eq.(2.71) can be used to compute the relative angular motion of the chaser with respect to the target.

2.4.2. Relative Dynamics

We can define the angular velocity of the chaser with respect to the target as:

$$\boldsymbol{\omega}_{c/t}^c = \boldsymbol{\omega}_c^c - \boldsymbol{\omega}_t^c = \boldsymbol{\omega}_c^c - \mathbf{A}_{c/t}(\boldsymbol{\theta}) \boldsymbol{\omega}_t^t \quad (2.72)$$

Here, the direction cosine matrix is a function of the Euler's angles and is written for a set of rotations 321. $\boldsymbol{\omega}_{c/t}^c$ is the relative angular velocity expressed in the chaser's body frame, and $\boldsymbol{\theta} = [\theta_x, \theta_y, \theta_z]^T$ is the relative attitude. A first step for the computation of the relative equations of motion is to linearize Euler's equations of the chaser around the angular velocity of the target and the control torque applied to it [4].

$$\mathbf{I}\dot{\boldsymbol{\omega}}_c^c = \left(\mathbf{M}_t - \boldsymbol{\omega}_t \times (\mathbf{I}\boldsymbol{\omega}_t) + \left. \frac{\mathbf{I}\partial\dot{\boldsymbol{\omega}}_c}{\partial\boldsymbol{\omega}_c} \right|_{\boldsymbol{\omega}_t, \mathbf{M}_t} (\boldsymbol{\omega}_c - \boldsymbol{\omega}_t) + \left. \frac{\mathbf{I}\partial\dot{\boldsymbol{\omega}}_c}{\partial\mathbf{M}_c} \right|_{\boldsymbol{\omega}_t, \mathbf{M}_t} (\mathbf{M}_c - \mathbf{M}_t) \right)^c \quad (2.73)$$

The operating points are $\mathbf{M}_t^c = [0, 0, 0]^T$, $\boldsymbol{\omega}_t^c = [\omega_{t,x}^c, \omega_{t,y}^c, \omega_{t,z}^c]$. All the variables in the equation are expressed in the chaser's body frame. Let's analyse all the components:

- Order zero term of Taylor's expansion:

$$(\mathbf{M}_t - \boldsymbol{\omega}_t \times (\mathbf{I}\boldsymbol{\omega}_t))^c = \mathbf{I}\dot{\boldsymbol{\omega}}_t^c \Rightarrow \mathbf{I}\dot{\boldsymbol{\omega}}_c^c - \mathbf{I}\dot{\boldsymbol{\omega}}_t^c = \mathbf{I}\dot{\boldsymbol{\omega}}_{c/t}^c \quad (2.74)$$

Here, $\dot{\omega}_{c/t}^c$ is the time derivative of the relative angular velocity expressed in the body frame of the chaser.

- Order one term of Taylor's expansion: first Jacobian:

$$\frac{\mathbf{I}\partial\dot{\omega}_c}{\partial\omega_c}\Bigg|_{\omega_t, \mathbf{M}_t} = \begin{bmatrix} 0 & I_y\omega_{t,z}^c - I_z\omega_{t,z}^c & I_y\omega_{t,y}^c - I_z\omega_{t,y}^c \\ I_z\omega_{t,z}^c - I_x\omega_{t,z}^c & 0 & I_z\omega_{t,x}^c - I_x\omega_{t,x}^c \\ I_x\omega_{t,y}^c - I_y\omega_{t,y}^c & I_x\omega_{t,x}^c - I_y\omega_{t,x}^c & 0 \end{bmatrix} \quad (2.75)$$

- Order one term of Taylor's expansion: second Jacobian:

$$\frac{\mathbf{I}\partial\dot{\omega}_c}{\partial\mathbf{M}_c}\Bigg|_{\omega_t, \mathbf{M}_t} = \begin{bmatrix} 1 & 0 & 0 \\ 0 & 1 & 0 \\ 0 & 0 & 1 \end{bmatrix} \quad (2.76)$$

Therefore, Eq.(2.73) can be rewritten as:

$$\begin{aligned} \mathbf{I}\dot{\omega}_{c/t}^c &= \begin{bmatrix} 0 & I_y\omega_{t,z}^c - I_z\omega_{t,z}^c & I_y\omega_{t,y}^c - I_z\omega_{t,y}^c \\ I_z\omega_{t,z}^c - I_x\omega_{t,z}^c & 0 & I_z\omega_{t,x}^c - I_x\omega_{t,x}^c \\ I_x\omega_{t,y}^c - I_y\omega_{t,y}^c & I_x\omega_{t,x}^c - I_y\omega_{t,x}^c & 0 \end{bmatrix} \omega_{c/t}^c + \mathbf{I}_{3\times 3}\mathbf{M}_c = \\ &= \mathbf{F}(\boldsymbol{\theta})\omega_{c/t}^c + \mathbf{I}_{3\times 3}\mathbf{M}_c^c \end{aligned} \quad (2.77)$$

The angular velocity of the target expressed in the chaser's body frame is a function of the relative attitude between the chaser's body frame and the target's body frame:

$$\omega_t^c = \mathbf{A}_{c/t}(\boldsymbol{\theta})\omega_t, \quad \text{with } \omega_t = [\omega_{t,x}, \omega_{t,y}, \omega_{t,z}]^T \quad (2.78)$$

Eq.(2.77) can be again linearised around the operating point for the relative attitude and relative angular velocity ($\bar{\boldsymbol{\theta}} = [0, 0, 0]^T$ and $\bar{\omega}_{c/t}^c = [0, 0, 0]^T$). Therefore:

$$\mathbf{I}\dot{\omega}_c^c = \mathbf{F}(\bar{\boldsymbol{\theta}})\bar{\omega}_{c/t}^c + \frac{\partial(\mathbf{F}(\boldsymbol{\theta})\omega_{c/t}^c)}{\partial\boldsymbol{\theta}}\Bigg|_{\bar{\boldsymbol{\theta}}, \bar{\omega}_{c/t}^c} (\boldsymbol{\theta} - \bar{\boldsymbol{\theta}}) + \frac{\partial(\mathbf{F}(\boldsymbol{\theta})\omega_{c/t}^c)}{\partial\omega_{c/t}^c}\Bigg|_{\bar{\boldsymbol{\theta}}, \bar{\omega}_{c/t}^c} (\omega_{c/t}^c - \bar{\omega}_{c/t}^c) + \mathbf{I}_{3\times 3}\mathbf{M}_c \quad (2.79)$$

It leads to the following linear equation:

$$\begin{aligned} \mathbf{I}\dot{\boldsymbol{\omega}}_c^c &= \begin{bmatrix} 0 & 0 & 0 \\ 0 & 0 & 0 \\ 0 & 0 & 0 \end{bmatrix} \boldsymbol{\theta} + \begin{bmatrix} 0 & \omega_{t,z}(I_y - I_z) & \omega_{t,y}(I_y - I_z) \\ -\omega_{t,z}(I_x - I_z) & 0 & -\omega_{t,x}(I_x - I_z) \\ \omega_{t,y}(I_x - I_y) & \omega_{t,x}(I_x - I_y) & 0 \end{bmatrix} \boldsymbol{\omega}_{c/t}^c + \\ &+ \begin{bmatrix} 1 & 0 & 0 \\ 0 & 1 & 0 \\ 0 & 0 & 1 \end{bmatrix} \mathbf{M}_c \end{aligned} \quad (2.80)$$

2.4.3. Relative Kinematics

The non-linear kinematics is given by Eq.(2.71):

$$\begin{bmatrix} \dot{\theta}_x \\ \dot{\theta}_y \\ \dot{\theta}_z \end{bmatrix} = \begin{bmatrix} 1 & \sin \theta_x \tan \theta_y & \cos \theta_x \tan \theta_y \\ 0 & \cos \theta_x & -\sin \theta_x \\ 0 & \sin \theta_x / \cos \theta_y & \cos \theta_x / \cos \theta_y \end{bmatrix} \boldsymbol{\omega}_{c/t}^c = \mathbf{H}(\boldsymbol{\theta}) \boldsymbol{\omega}_{c/t}^c \quad (2.81)$$

The latter can be linearised around the operating point for the relative attitude and relative angular velocity ($\bar{\boldsymbol{\theta}} = [0, 0, 0]^T$ and $\bar{\boldsymbol{\omega}}_{c/t}^c = [0, 0, 0]^T$). Therefore:

$$\dot{\boldsymbol{\theta}} = \mathbf{H}(\bar{\boldsymbol{\theta}}) \bar{\boldsymbol{\omega}}_{c/t}^c + \frac{\partial \mathbf{H}(\boldsymbol{\theta}) \boldsymbol{\omega}_{c/t}^c}{\partial \boldsymbol{\theta}} \Bigg|_{\bar{\boldsymbol{\theta}}, \bar{\boldsymbol{\omega}}_{c/t}^c} (\boldsymbol{\theta} - \bar{\boldsymbol{\theta}}) + \frac{\partial \mathbf{H}(\boldsymbol{\theta}) \boldsymbol{\omega}_{c/t}^c}{\partial \boldsymbol{\omega}_{c/t}^c} \Bigg|_{\bar{\boldsymbol{\theta}}, \bar{\boldsymbol{\omega}}_{c/t}^c} (\boldsymbol{\omega}_{c/t}^c - \bar{\boldsymbol{\omega}}_{c/t}^c) \quad (2.82)$$

It leads to:

$$\dot{\boldsymbol{\theta}} = \begin{bmatrix} 0 & 0 & 0 \\ 0 & 0 & 0 \\ 0 & 0 & 0 \end{bmatrix} \boldsymbol{\theta} + \begin{bmatrix} 1 & 0 & 0 \\ 0 & 1 & 0 \\ 0 & 0 & 1 \end{bmatrix} \boldsymbol{\omega}_{c/t}^c \quad (2.83)$$

2.4.4. Relative Equations of Motion

We can define the relative state as:

$$\mathbf{x} = \begin{bmatrix} \boldsymbol{\theta} \\ \boldsymbol{\omega}_{c/t}^c \end{bmatrix} \quad (2.84)$$

Therefore, the state space formulation is:

$$\begin{aligned} \dot{\mathbf{x}}(t) = & \begin{bmatrix} 0 & 0 & 0 & 1 & 0 & 0 \\ 0 & 0 & 0 & 0 & 1 & 0 \\ 0 & 0 & 0 & 0 & 0 & 1 \\ 0 & 0 & 0 & 0 & \frac{\omega_{t,z}(I_y - I_z)}{I_x} & \frac{\omega_{t,y}(I_y - I_z)}{I_x} \\ 0 & 0 & 0 & -\frac{\omega_{t,z}(I_x - I_z)}{I_y} & 0 & -\frac{\omega_{t,x}(I_x - I_z)}{I_y} \\ 0 & 0 & 0 & \frac{\omega_{t,y}(I_x - I_y)}{I_z} & \frac{\omega_{t,x}(I_x - I_y)}{I_z} & 0 \end{bmatrix} \mathbf{x}(t) + \\ & + \begin{bmatrix} 0 & 0 & 0 \\ 0 & 0 & 0 \\ 0 & 0 & 0 \\ \frac{1}{I_x} & 0 & 0 \\ 0 & \frac{1}{I_y} & 0 \\ 0 & 0 & \frac{1}{I_z} \end{bmatrix} \mathbf{M}_c(t) \end{aligned} \quad (2.85)$$

Once the inertia matrix of the chaser vehicle and the target's body-frame angular velocity are known, the equations of motion can be fully defined. Furthermore, the system exhibits linear time-varying (LTV) behavior for eccentric orbits of the target due to the time dependence of the angular velocity vector. In contrast, the system becomes linear time-invariant (LTI) for circular orbits, where the angular velocity vector remains constant over time. Specifically, the time dependence appears in the system (plant) matrix, while the input matrix remains constant at all times.

3 | Rendezvous Simulator: Structure and Components

This chapter outlines the architecture of the simulator developed for modeling the guidance, navigation, and control of rendezvous dynamics. The simulator is organized around a separation between the *real world* and the *on-board software*. The *real world* component models the physical motion of the spacecraft and the surrounding operational environment. In contrast, the *software* component represents the on-board algorithms responsible for processing sensor measurements and computing the control commands applied to the vehicles. The structure of this first layer of the simulator is illustrated in Figure 3.1. The diagram shows how the outputs of the real world, namely, the rotational and translational states (including the absolute states of the target and both the absolute and relative states of the chaser), are fed into the on-board software to simulate sensor measurements. The control commands generated by the software are then applied back to the real world, thereby influencing the spacecraft dynamics.

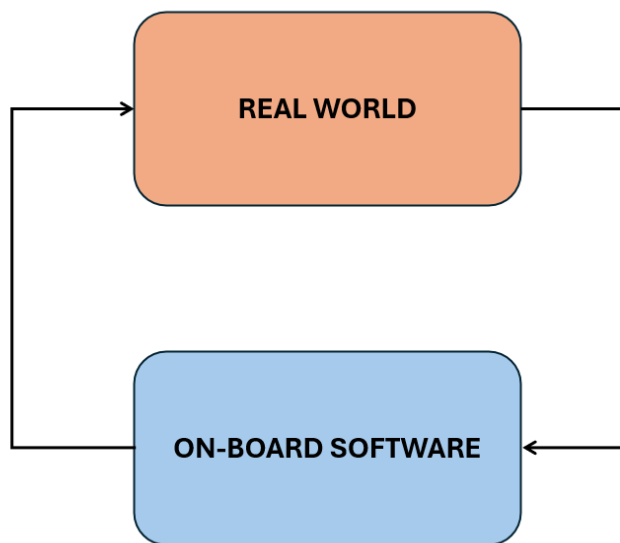


Figure 3.1: Simulator

3.1. Real world

The *real world* block simulates the equations of motion and the operating environment of the two satellites, as shown in Figure 3.2. The control input computed by the *software* block is applied to the satellites' dynamics, along with disturbances from the external environment. This information is processed by the *dynamics* block to compute the updated translational and rotational states. These updated states are then sent to the *software* block and also fed back to the *environment* blocks.

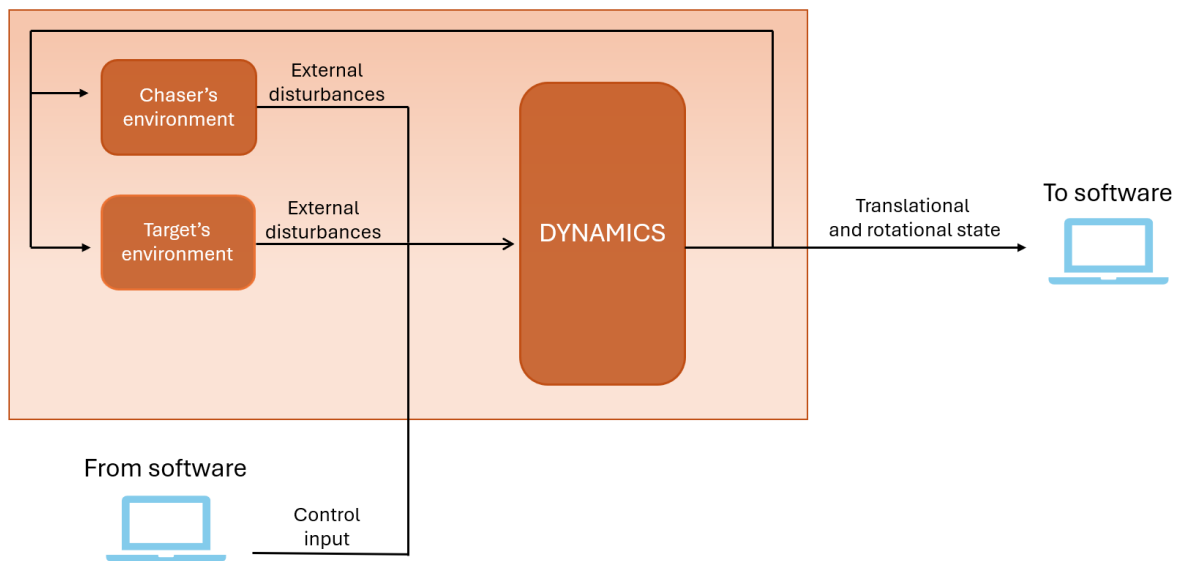


Figure 3.2: Simulator/ Real World

3.1.1. Dynamics

The *dynamics* block is separated into the chaser's dynamics, the target's dynamics, and the relative states. It takes as input the control commands computed by the *software* block (acceleration and torque), along with the disturbances (acceleration and torque) acting on both satellites. The translational equations of motion for the satellites are based on a Cartesian representation. The structure is designed to model the absolute dynamics of the two vehicles in order to retrieve their absolute state, orbital elements, angular velocity, and quaternion. This information is then used to determine the relative states. The output of the block includes both absolute and relative state information.

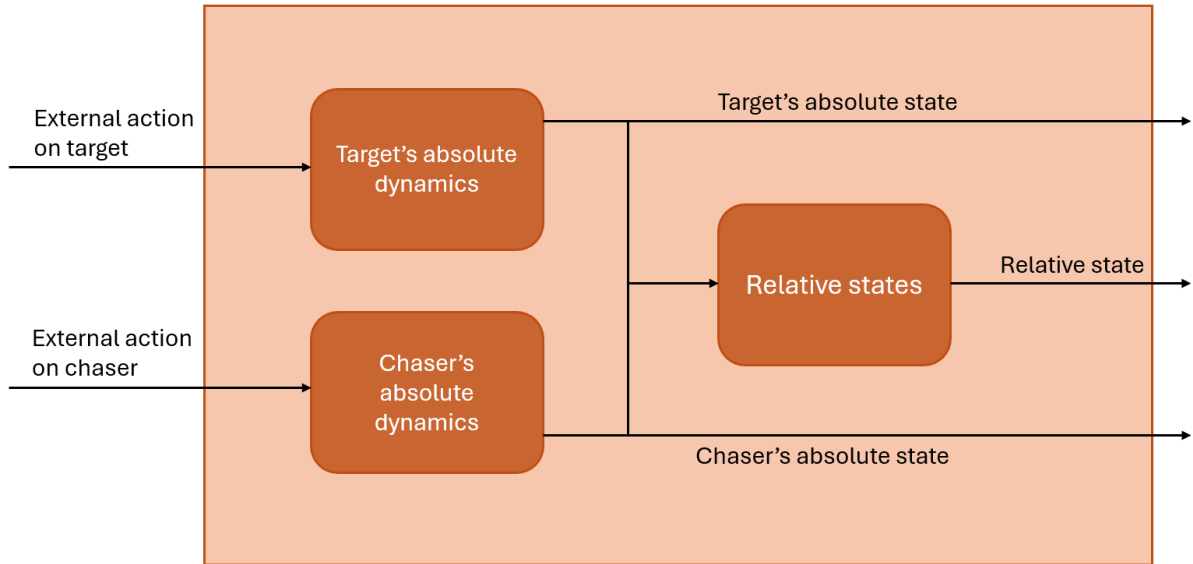


Figure 3.3: Simulator/ Real World/ Dynamics

Absolute Dynamics

The absolute dynamics takes the external acceleration and torque as input and is modeled as shown in Figure 3.4:

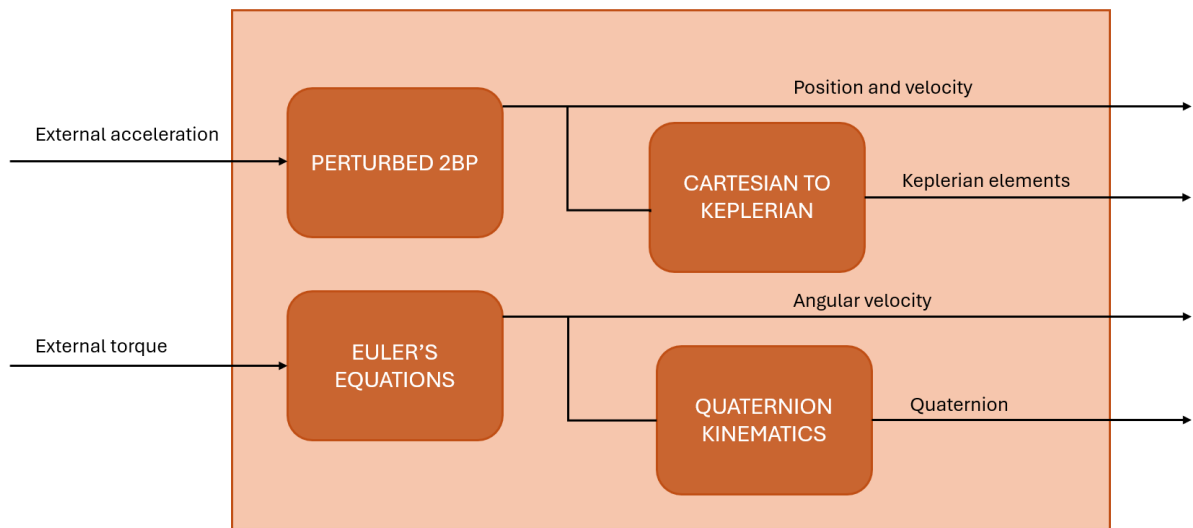


Figure 3.4: Simulator/ Real World/ Dynamics/ Absolute Dynamics

- **Translational dynamics:** the system integrates the non-linear 2-body-problem

along with the external accelerations [1].

$$\ddot{\mathbf{r}} = -\frac{\mu}{r^3} \mathbf{r} + \mathbf{a}_{ext} \quad (3.1)$$

Here, \mathbf{r} is the spacecraft position, μ the Earth's planetary gravitational constant, and \mathbf{a}_{ext} represents the external accelerations coming from disturbances and control actions acting on the satellite. The Keplerian orbital elements are then obtained from the Cartesian state using a *Cartesian-to-Keplerian* transformation function. An efficient method is employed to reduce the conversion errors, particularly for low-eccentricity orbits [17].

- **Rotational dynamics:** the angular state is computed by integrating Euler's equations together with the quaternion kinematics [27]. The Euler's equation is formulated as follows:

$$\mathbf{I}\dot{\boldsymbol{\omega}} + \boldsymbol{\omega} \times (\mathbf{I}\boldsymbol{\omega}) = \mathbf{M}_{ext} \quad (3.2)$$

Here \mathbf{I} is the inertia tensor, $\boldsymbol{\omega}$ the satellite's angular velocity, and \mathbf{M}_{ext} represents the external torque acting on the vehicle (disturbances and control input). The quaternion is retrieved by integrating the following equation:

$$\dot{\mathbf{q}} = \frac{1}{2} \boldsymbol{\Omega}(\boldsymbol{\omega}) \mathbf{q}$$

$$\boldsymbol{\Omega}(\boldsymbol{\omega}) = \begin{bmatrix} 0 & -\omega_1 & -\omega_2 & -\omega_3 \\ \omega_1 & 0 & \omega_3 & -\omega_2 \\ \omega_2 & -\omega_3 & 0 & \omega_1 \\ \omega_3 & \omega_2 & -\omega_1 & 0 \end{bmatrix} \quad (3.3)$$

The integration of the former equations allows for the retrieval of the translation and rotational absolute state of the two satellites. It will be employed to obtain data based on the absolute dynamics of the satellite and to compute the chaser's relative state with respect to the target.

Relative States

The absolute translational and rotational states of the target and chaser are employed to compute the relative quantities as displayed in Figure 3.5

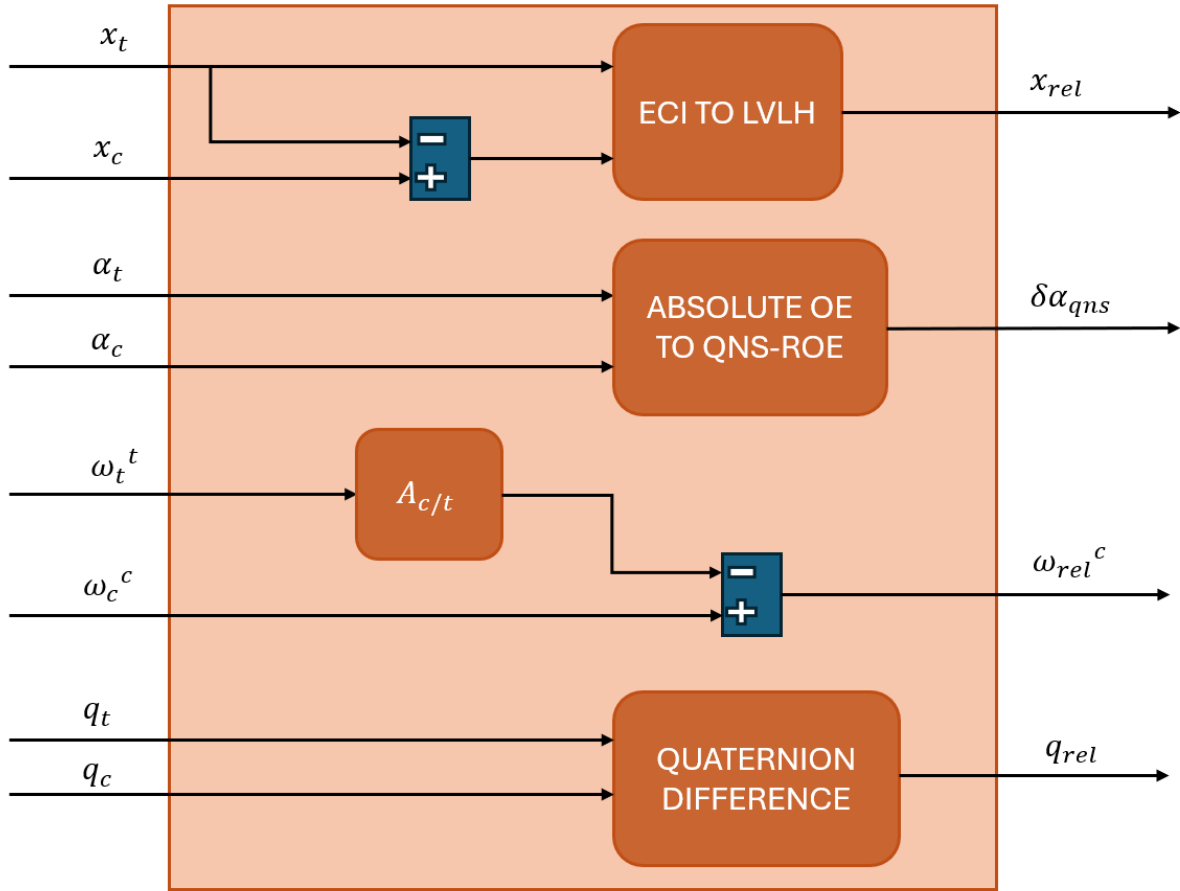


Figure 3.5: Simulator/ Real World/ Dynamics/ Relative States

- Relative position and velocity:** the absolute positions and velocities are given in the inertial frame; therefore, the relative state of the chaser with respect to the target is computed by subtracting the target's state to the chaser's one and then by applying the transformation from ECI to the target's LVLH frame;
- qns-ROE:** the Keplerian absolute elements are employed for the retrieval of the qns-ROE by applying Eq.(2.37);
- Relative angular velocity:** the target's angular velocity ω_t^t is rotated in the chaser's body frame to obtain ω_t^c and subtracted to the chaser's angular velocity ω_c^c ;
- Relative attitude:** the relative attitude is computed via quaternion differences:

$$\mathbf{q}_{rel} = \mathbf{q}_t \otimes \mathbf{q}_c^{-1} \quad (3.4)$$

Here, \otimes represents the quaternion multiplication and \mathbf{q}^{-1} is the conjugate quaternion.

3.1.2. External Disturbances

The *environment* blocks represent the external disturbances acting on the satellites. For the purpose of this simulation, the translational dynamics accounts for the J_2 gravitational perturbation and aerodynamic drag. No disturbances are considered in the rotational dynamics. For the J_2 gravitational perturbation, the following formulation is employed [2]:

$$\mathbf{a}_{J_2} = -\frac{3}{2} J_2 \left(\frac{\mu}{r^2} \right) \left(\frac{r_{eq}}{r} \right)^2 \begin{bmatrix} \left(1 - 5 \left(\frac{z}{r} \right)^2 \right) \frac{x}{r} \\ \left(1 - 5 \left(\frac{z}{r} \right)^2 \right) \frac{y}{r} \\ \left(3 - 5 \left(\frac{z}{r} \right)^2 \right) \frac{z}{r} \end{bmatrix} \quad (3.5)$$

Here, $J_2 = 1082.63 \times 10^6$, $\mathbf{r} = [x, y, z]^T$ is the spacecraft position, r_{eq} is the Earth's equatorial radius and μ is the Earth's planetary gravitational constant. The upper layers of the Earth's atmosphere produce a perturbation acceleration modeled as [22]:

$$\mathbf{a}_{drag} = -\frac{1}{2} \rho ||\mathbf{v} - \mathbf{v}_{atm}|| (\mathbf{v} - \mathbf{v}_{atm}) \frac{SC_d}{m} \quad (3.6)$$

Here, ρ denotes the atmospheric density, S the impact cross-sectional area, C_d the drag coefficient, and m the mass of the spacecraft. The quantity SC_d/m is called the ballistic coefficient.

3.2. On-Board Software

The *on-board Software* receives the information on the translational and rotational state from the *real world* and computes the control action required by the mission, as shown in Figure 3.6.

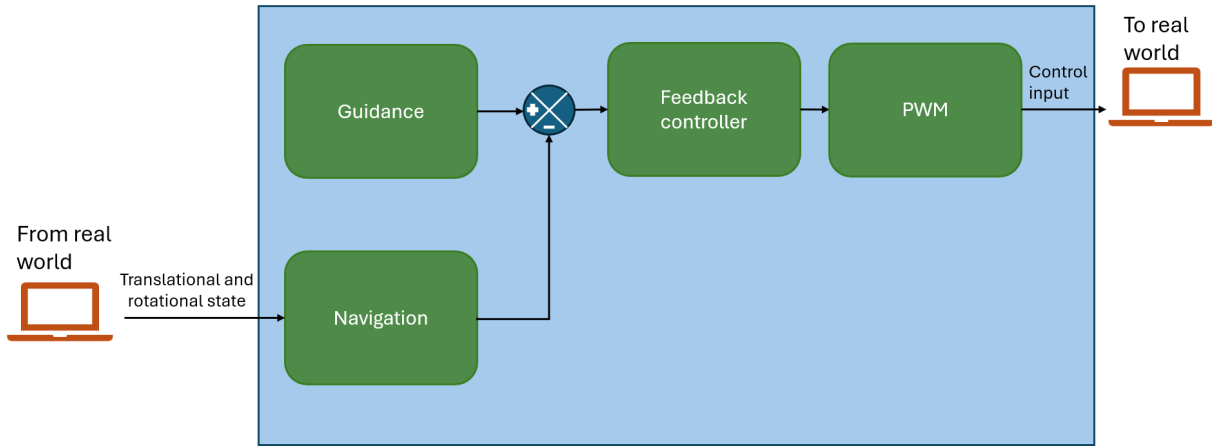


Figure 3.6: Simulator/ On-Board Software

3.2.1. Translational Guidance & Control

The information obtained from the real world is compared with a reference profile, and the resulting error is then used to compute the required control action, which is fed to the *actuators management* block.

- **Guidance:** The *guidance* block provides the reference trajectory to be followed in accordance with the mission requirements. It is implemented as an automated function capable of computing the reference state online, but it does not possess the capability to make autonomous decisions based on sensor inputs, environmental conditions, or evolving mission objectives. This means that the guidance profile is computed prior to the mission, and the resulting Δv or acceleration commands provided by this block are not updated during the mission. The block takes as input the pre-computed acceleration profile (see Section 4.1) and uses it to determine the current reference state, which is then compared with the state estimated from sensor measurements.
- **Navigation:** The simulator does not include an explicit navigation filter. Instead, navigation is simulated by taking the state data generated within the *real world* block and adding Gaussian white noise, based on results from previous studies [39], effectively modeling the output of a Kalman filter. The noise is characterized by the following standard deviation:

Quantity	3σ Value
Relative position	0.1 [m]
Relative velocity	10^{-4} [m/s]

Table 3.1: Standard deviation values used for noise modeling

The noise on the relative orbital elements is introduced by a transformation from the Cartesian state by means of Eq.(2.61).

- **Control:** While the *guidance* block does not support autonomous decision-making, the controller operates through a feedback mechanism. It takes as input the error between the *guidance* and *navigation* outputs and computes the required correction to the accelerations provided by the *guidance*.

3.2.2. Attitude Control

The attitude control software does not include a guidance block, and full authority is left to the feedback controller. The controller works as a regulator that leads the relative rotational state to zero in order for the chaser vehicle to have the same attitude and angular velocity of the chaser. Therefore, the target and chaser absolute rotational states are taken from the *real world* block and, as explained in Section 2.4, the relative state is retrieved and fed to the LQR controller in order to calculate the control torque. The latter will be used as the input of the Euler equations of the chaser absolute rotational dynamics block.

3.2.3. Actuators Management

The ideal control action computed by the controller must be adapted to match the actual capabilities of the available actuators. Since the actuators logic is neglected for rotational control, the ideal input torque is directly applied to the *real world* block.

For translational control, non-throttleable thrusters are employed, meaning they can only produce a fixed level of thrust. To approximate the desired acceleration profile, the control algorithm utilizes *pulse-width modulation* (PWM) [50]. Pulse-width modulation (PWM) is a control technique that adjusts the effective output of an actuator by varying the duration of its "on" time within a fixed time interval. Instead of continuously varying the magnitude of the actuator's output, PWM rapidly switches it on and off, with the ratio of on-time to the total period (the duty cycle) determining the average effect over

that interval. This requires discretizing the continuous control signal using a *zero-order hold* (ZOH), aligning it with the selected discretization time for the thrust commands. The concept of PWM is shown in Figure 3.7. A continuous input signal (shown in red) represents the ideal thrust level over time. This signal is compared to a repeating reference waveform (called the carrier), which oscillates between fixed maximum and minimum values. Whenever the input signal is higher than the carrier, the output pulse is turned ON at full thrust; when it's lower, the output is OFF. This creates a series of pulses all at the same thrust level, but with different durations (widths). By adjusting how long each pulse stays ON within a fixed time frame, the average thrust over time closely matches the original continuous input signal.

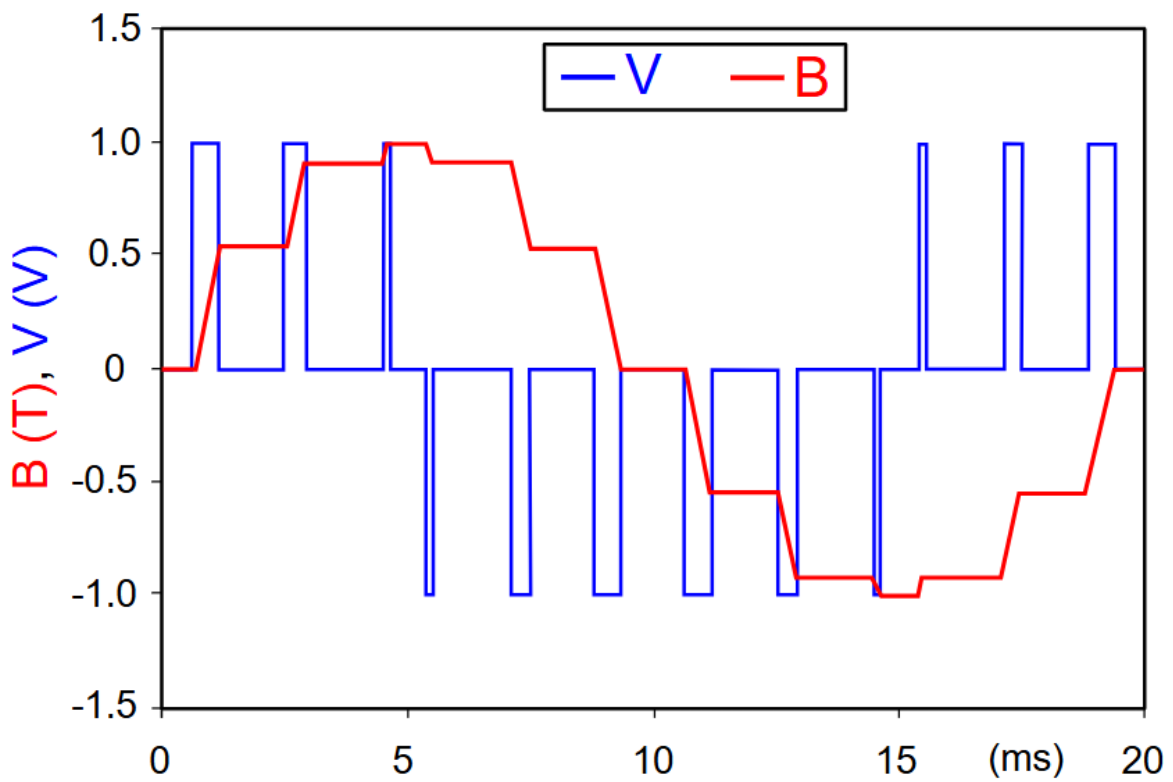


Figure 3.7: Pulse-width-modulation (From Ref. [46])

The PWM technique converts the discretized control input into a command compatible with the fixed thrust level. Specifically, the thruster firing time t_{fire} is computed based on the ratio between the ideal thrust requested by the controller T_{ideal} and the actual thrust available from the thruster T_{real} , over the discretization interval t_{disc} :

$$t_{\text{fire}} = \frac{T_{\text{ideal}}}{T_{\text{real}}} t_{\text{disc}} \quad (3.7)$$

Rather than firing the thruster continuously for the full discretization period with the ideal thrust T_{ideal} , the algorithm computes a reduced firing time t_{fire} at the available thrust level T_{real} . This preserves the total impulse delivered while respecting the hardware constraints.

Additionally, the algorithm considers the *minimum impulse bit* (MIB), as specified in the thruster datasheet. The Minimum Impulse Bit (MIB) is the smallest amount of impulse a thruster can reliably produce in a single firing. It is determined by the minimum firing duration and the fixed thrust level of the actuator. If the calculated impulse for a given time step is below the MIB, the action is not executed. Instead, the impulse is stored and accumulated. Once the accumulated impulse reaches or exceeds the MIB, the corresponding thrust command is applied, and the accumulator is reset. This mechanism ensures that even sub-threshold control efforts eventually result in actuation, without violating the minimum impulse constraints of the thruster.

The propellant mass consumption can be determined from the total firing time, the thrust profile, and the specific impulse. For a constant thrust profile, the specific impulse is defined as [41]:

$$I_s = \frac{I_{\text{tot}}}{M_p g_0} \quad (3.8)$$

where I_{tot} is the total impulse, M_p is the propellant mass, and g_0 is the gravitational acceleration at sea level. Since the duty cycle is generated by discretization through a zero-order hold (ZOH) process, the total impulse, defined as the integral of the thrust profile over time, can be expressed simply as the product of the constant thrust and the burning time:

$$I_{\text{tot}} = \int_{t_0}^{t_f} T(t) dt = \bar{T} t_{\text{fire}} \quad (3.9)$$

Here, \bar{T} is the constant thrust level and Δt_{fire} is the total firing duration.

4 | RVD guidance & control

Contents and Contributions

The aim of this chapter is to present the main algorithms used for computing the guidance reference profile and the control gains. The chapter begins with a description of the guidance algorithm, followed by an analysis of the feedback controller.

- Section 4.1 presents the algorithm used to generate the guidance profile that serves as a reference input for the controller. The impulsive guidance profile is examined with reference to state-of-the-art studies [19–21, 24]. While these works support the analysis, an original multi-impulse profile is developed by combining an accelerating inbound and a decelerating inbound glideslope for the final approach phase of a rendezvous mission. Additionally, a continuous guidance profile is obtained through an original derivation and discretization of the convolution integral, which represents the particular solution to the equations of motion.
- Section 4.2 addresses the rendezvous control problem. It explores the linear optimal control problem and its application to the final approach phase of a rendezvous mission. Several references are considered in constructing a feedback controller [5, 38, 40, 42]. Nonetheless, the analysis of the feedback controller’s application to rendezvous dynamics is the result of original work, particularly regarding the ROE-based formulation of the equations of motion. The controllability analysis of the resulting state-space systems is also an original contribution of this work.

4.1. Guidance

As previously explained (Chapter 3), the guidance function is generated on-ground and subsequently processed by the on-board software to compute, at each time instant, the desired spacecraft state and corresponding acceleration. This reference acceleration is then corrected by the feedback controller, which uses real-time data from the navigation system to ensure the actual state follows the reference trajectory. In this study, two

different strategies are investigated for constructing the guidance profile that serves as the reference input for the on-board software. Since the focus is on the final approach phase of a rendezvous and docking mission, a common method is to execute the final maneuver using continuous thrust. However, an alternative impulsive strategy is also analyzed. This comparison aims to assess how well an impulsive profile can be integrated with the feedback controller and to evaluate its impact on mission constraints and propellant consumption.

4.1.1. Impulsive Guidance Profile

The equations of motion when an impulsive control input is applied to the spacecraft free dynamics are described in Section 2.2.3 and Section 2.2.4 for the Cartesian-based dynamics and in Section 2.3.3 for the ROE-based dynamics. For both scenarios, the time propagation of the state when a single impulse is applied to the spacecraft is:

$$\mathbf{x}(t) = \Phi(t, t_0)\mathbf{x}_0 + \Phi(t, t_{imp})\mathbf{B}(t_{imp})\Delta\mathbf{v} \quad (4.1)$$

Where $\mathbf{B}(t)$ is time-varying for the ROE-based dynamics and constant for the Cartesian-based dynamics.

Two-Impulse Manoeuvre

The procedure to compute the guidance profile for a two-impulse manoeuvre is based on Ref. [19, 21, 24, 37]. Eq. (4.1) can be extended to the case of two impulses by considering a first impulse $\Delta\mathbf{v}_1$ applied at t_0 and a second one $\Delta\mathbf{v}_2$ applied at t_1 . The final state, computed after the second impulse is obtained through the following procedure:

$$\begin{cases} \mathbf{x}_0^+ = \mathbf{x}_0^- + \mathbf{B}(t_0)\Delta\mathbf{v}_1 \\ \mathbf{x}_1^- = \Phi(t_1, t_0)\mathbf{x}_0^+ \\ \mathbf{x}_f = \mathbf{x}_1^+ = \mathbf{x}_1^- + \mathbf{B}(t_1)\Delta\mathbf{v}_2 \end{cases} \quad (4.2)$$

Which leads to:

$$\begin{aligned} \mathbf{x}_f &= \Phi(t_1, t_0)(\mathbf{x}_0 + \mathbf{B}(t_0)\Delta\mathbf{v}_1) + \mathbf{B}(t_1)\Delta\mathbf{v}_2 = \\ &= \Phi(t_1, t_0)\mathbf{x}_0 + [\Phi(t_1, t_0)\mathbf{B}(t_0) \quad \mathbf{B}(t_1)] \begin{bmatrix} \Delta\mathbf{v}_1 \\ \Delta\mathbf{v}_2 \end{bmatrix} \end{aligned} \quad (4.3)$$

The $\Delta\mathbf{v}$ required to perform a manoeuvre from the initial state \mathbf{x}_0 to a final state \mathbf{x}_f is given by:

$$\Delta\mathbf{V} = \begin{bmatrix} \Delta\mathbf{v}_1 \\ \Delta\mathbf{v}_2 \end{bmatrix} = [\Phi(t_1, t_0)\mathbf{B}(t_0) \quad \mathbf{B}(t_1)]^{-1} (\mathbf{x}_f - \Phi(t_1, t_0)\mathbf{x}_0) \quad (4.4)$$

Three-Impulse Manoeuvre

The three-impulse manoeuvre can be computed as the composition of two two-impulse manoeuvre, where the second and third impulses overlap in correspondence of the same time instant. Therefore:

$$\begin{cases} \mathbf{x}_0^+ = \mathbf{x}_0^- + \mathbf{B}(t_0)\Delta\mathbf{v}_1 \\ \mathbf{x}_{1,1}^- = \Phi(t_1, t_0)\mathbf{x}_0^+ \\ \mathbf{x}_{1,1}^+ = \mathbf{x}_{1,1}^- + \mathbf{B}(t_1)\Delta\mathbf{v}_{2,1} \end{cases} + \begin{cases} \mathbf{x}_{1,2}^- = \mathbf{x}_{1,1}^+ \\ \mathbf{x}_{1,2}^+ = \mathbf{x}_{1,2}^- + \mathbf{B}(t_1)\Delta\mathbf{v}_{2,2} \\ \mathbf{x}_2^- = \Phi(t_2, t_1)\mathbf{x}_{1,2}^+ \\ \mathbf{x}_f = \mathbf{x}_2^+ = \mathbf{x}_2^- + \mathbf{B}(t_2)\Delta\mathbf{v}_3 \end{cases} \quad (4.5)$$

Which leads to:

$$\mathbf{x}_f = \Phi(t_2, t_0)\mathbf{x}_0 + [\Phi(t_2, t_0)\mathbf{B}(t_0) \quad \Phi(t_2, t_1)\mathbf{B}(t_1) \quad \mathbf{B}(t_2)] \begin{bmatrix} \Delta\mathbf{v}_1 \\ \Delta\mathbf{v}_{2,1} + \Delta\mathbf{v}_{2,2} \\ \Delta\mathbf{v}_3 \end{bmatrix} \quad (4.6)$$

And the $\Delta\mathbf{V}$ is given by:

$$\Delta\mathbf{V} = \begin{bmatrix} \Delta\mathbf{v}_1 \\ \Delta\mathbf{v}_{2,1} + \Delta\mathbf{v}_{2,2} \\ \Delta\mathbf{v}_3 \end{bmatrix} = [\Phi(t_2, t_0)\mathbf{B}(t_0) \quad \Phi(t_2, t_1)\mathbf{B}(t_1) \quad \mathbf{B}(t_2)]^{-1} (\mathbf{x}_f - \Phi(t_2, t_0)\mathbf{x}_0) \quad (4.7)$$

Multi-Impulse Manoeuvre

The $\Delta\mathbf{V}$ of a multi-impulse manoeuvre is given by the composition of N two-impulse manoeuvres:

$$\Delta\mathbf{V} = \begin{bmatrix} \Delta\mathbf{v}_1 \\ \vdots \\ \Delta\mathbf{v}_{i,1} + \Delta\mathbf{v}_{i,2} \\ \vdots \\ \Delta\mathbf{v}_f \end{bmatrix} = \mathbf{M}^{-1}(\mathbf{x}_f - \Phi(t_N, t_0)\mathbf{x}_0) \quad (4.8)$$

where $\mathbf{M} = [\Phi(t_N, t_0)\mathbf{B}(t_1) \quad \dots \quad \Phi(t_N, t_i)\mathbf{B}(t_i) \quad \dots \quad \mathbf{B}(t_N)]$

Glideslope Profile

The guidance strategy proposed in this study is based on the solution employed in Ref. [24]: the vector $\rho(t)$ is generated from the tip of the position vector $\mathbf{r}(t)$ and defines the commanded location of the chaser along the straight path from \mathbf{r}_0 to \mathbf{r}_f (see Figure 4.1 and Figure 4.2). The strategy consists on defining the profile along the straight line, which allows to fix the intermediate position between two sets of two-impulse manoeuvres. Moreover, the interval between two successive pulses is constant and computed as $\Delta t = T/N$, where T is the duration of the overall manoeuvre. Once the initial and final states, the profile along the straight-line path, the duration T , and the number of successive impulses are defined, the $\Delta\mathbf{v}$ vectors at the boundaries of each two-impulse manoeuvre can be computed. The resulting guidance profile is then defined by the $N + 1$ impulsive manoeuvres performed at the boundary positions along $\rho(t)$.

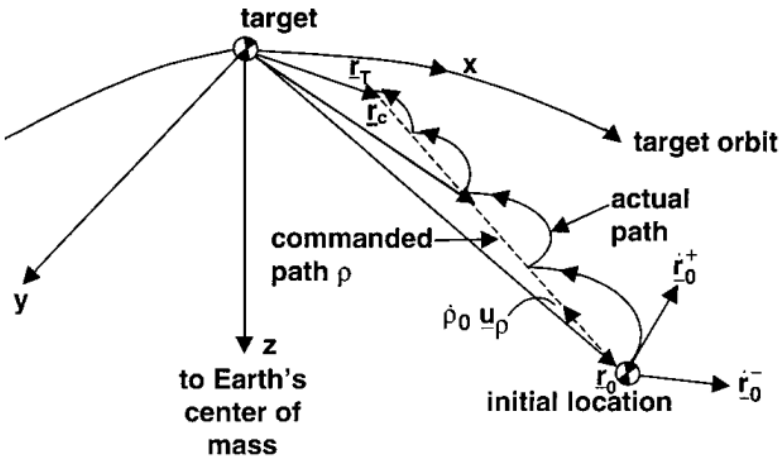


Figure 4.1: Decelerating inbound glideslope (from Ref. [24])

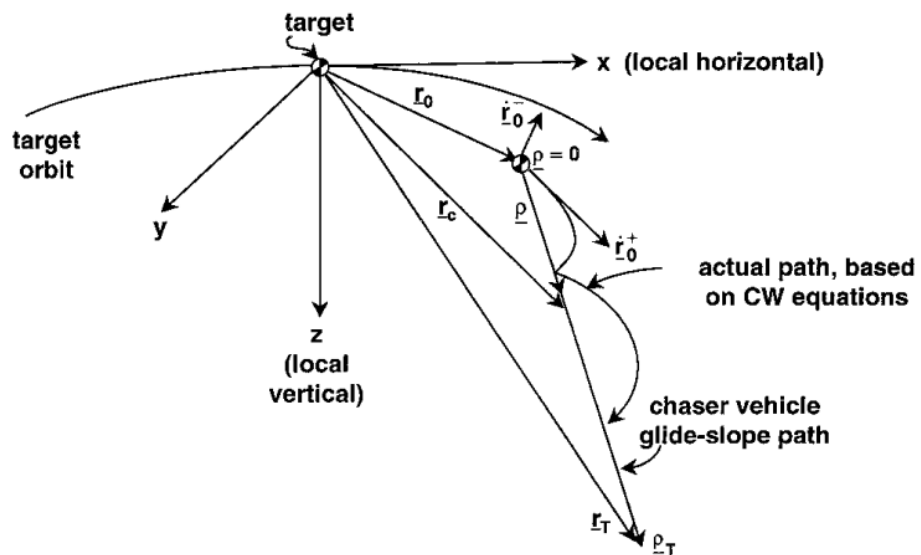


Figure 4.2: Accelerating inbound glideslope (from Ref. [24])

Figure 4.1 illustrates the decelerating inbound glideslope, where impulsive maneuvers executed at each Δt are used to decelerate the spacecraft while decreasing its distance from the target vehicle. Conversely, Figure 4.2 depicts an accelerating outbound glideslope, in which the spacecraft increases both its velocity and distance from the target. During the final approach phase of a rendezvous mission, the chaser vehicle must reduce its velocity while closing the distance to the target, in order to comply with the maximum allowed docking velocity. However, between the closing phase and the final approach, it is common for the chaser to be held at a designated hold point. This hold point maintains a fixed relative position with respect to the target to allow for other mission operations to

be performed [16]. As a result, when the final approach begins, the chaser must first be accelerated to gain sufficient velocity, and then gradually decelerated to reach the docking point with the required position and velocity alignment. Therefore, a combination of an inbound accelerating glideslope, an inbound coasting profile with constant velocity, and an inbound decelerating glideslope will be employed.

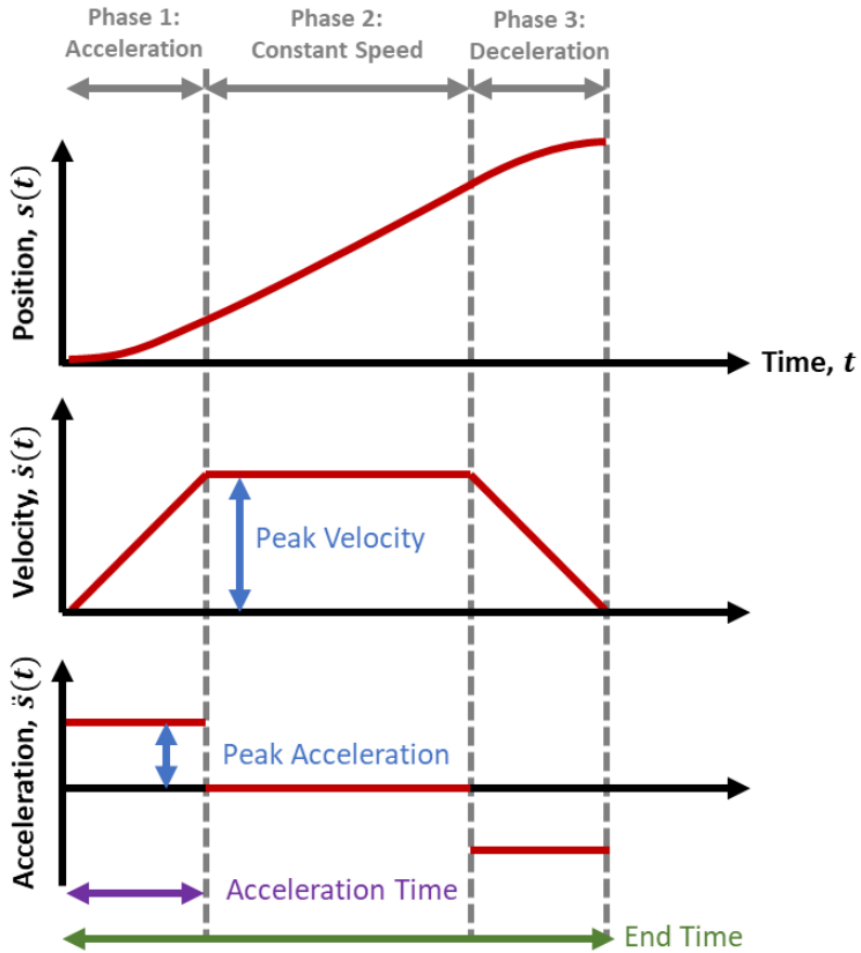


Figure 4.3: Trapezoidal velocity profile (from Ref. [28])

Figure 4.3 shows the trapezoidal velocity profile. In this profile, the constant acceleration phase results in a linearly increasing velocity and a parabolic position trajectory. During the coasting phase, where acceleration is zero, the velocity remains constant and the position increases linearly with time. This motion profile represents the path of the vector $\rho(t)$, which defines the commanded position of the chaser along the straight-line trajectory from the initial point \mathbf{r}_0 to the final point \mathbf{r}_f . Consequently, the actual trajectory of the chaser does not follow the continuous parabolic curve shown in Figure 4.3; instead, the impulsive maneuver points are sampled along this idealized reference path. Similarly, the

initial velocity increment applied at each control node (*e.g.*, $\Delta\mathbf{v}_{i,1}$ in Equation 4.8) is chosen to match the instantaneous velocity defined by the trapezoidal velocity profile at that node. This ensures consistency between the discrete impulsive control strategy and the continuous reference trajectory.

The procedure requires the definition of a set of parameters that enable the computation of the complete profile for $\rho(t)$. Once the initial and final states $(\rho_0, \rho_f, \dot{\rho}_0, \dot{\rho}_f)$ are known, the following steps are performed:

- **Accelerating glideslope:** This phase involves selecting the segment length $\rho_{f,acc}$, the number of impulsive manoeuvres N_{acc} , and the acceleration a_{acc} . The relevant quantities are computed as:

$$\begin{aligned} T_{acc} &= \sqrt{\frac{2\rho_{f,acc}}{a_{acc}}} \\ \Delta t_{acc} &= \frac{T_{acc}}{N_{acc}} \\ \dot{\rho}_{f,acc} &= a_{acc}T_{acc} \end{aligned} \tag{4.9}$$

The position and velocity profiles are then:

$$\begin{aligned} \rho_{acc}(n) &= \frac{1}{2}a_{acc}(n\Delta t_{acc})^2 \quad \text{for } n = 1, \dots, N_{acc} \\ \dot{\rho}_{acc}(n) &= a_{acc}(n\Delta t_{acc}) \end{aligned} \tag{4.10}$$

- **Coasting glideslope:** This phase maintains a uniform spacing between pulses, equal to that of the last two accelerating impulses. Once the number of impulses N_{coast} is chosen:

$$\begin{aligned} \rho_{f,coast} &= \rho_{f,acc} + N_{coast} |\rho_{f,acc} - \rho_{acc}(T_{acc} - \Delta t_{acc})| \\ T_{coast} &= \frac{\rho_{f,coast} - \rho_{f,acc}}{\dot{\rho}_{f,acc}} \\ \Delta t_{coast} &= \frac{T_{coast}}{N_{coast}} \\ \dot{\rho}_{f,coast} &= \dot{\rho}_{f,acc} \end{aligned} \tag{4.11}$$

The corresponding profiles are:

$$\begin{aligned} \rho_{coast}(n) &= \rho_{f,acc} + \dot{\rho}_{f,acc}(n\Delta t_{coast}) \quad \text{for } n = 1, \dots, N_{coast} \\ \dot{\rho}_{coast} &= \dot{\rho}_{f,acc} \end{aligned} \tag{4.12}$$

- **Decelerating glideslope:** This phase completes the profile to match the final position and velocity. It begins with the same step size as the last coasting interval. The key quantities are:

$$\begin{aligned}
 \rho_{f,\text{dec}} &= \rho_f \\
 T_{\text{dec}} &= \frac{2(\rho_{f,\text{dec}} - \rho_{f,\text{coast}})}{\dot{\rho}_{f,\text{acc}} + \dot{\rho}_f} \\
 a_{\text{dec}} &= \frac{\dot{\rho}_f - \dot{\rho}_{f,\text{acc}}}{T_{\text{dec}}} \\
 \Delta t_{\text{dec}} &= \frac{-\dot{\rho}_{f,\text{acc}} + \sqrt{\dot{\rho}_{f,\text{acc}}^2 + 2a_{\text{dec}} \frac{\rho_{f,\text{coast}} - \rho_{f,\text{acc}}}{N_{\text{coast}}}}}{a_{\text{dec}}} \\
 N_{\text{dec}} &= \text{round} \left(\frac{T_{\text{dec}}}{\Delta t_{\text{dec}}} \right)
 \end{aligned} \tag{4.13}$$

Resulting in:

$$\begin{aligned}
 \rho_{\text{dec}}(n) &= \rho_{f,\text{coast}} + \frac{1}{2} a_{\text{dec}} (n \Delta t_{\text{dec}})^2 \quad \text{for } n = 1, \dots, N_{\text{dec}} \\
 \dot{\rho}_{\text{dec}}(n) &= \dot{\rho}_{f,\text{coast}} + a_{\text{dec}} (n \Delta t_{\text{dec}})
 \end{aligned} \tag{4.14}$$

4.1.2. Continuos Guidance Profile

The equations of motion when a continuous control input is applied to the spacecraft free dynamics are described in Section 2.2.3 and Section 2.2.4 for the Cartesian-based dynamics and in Section 2.3.3 for the ROE-based dynamics:

$$\mathbf{x}(t) = \Phi(t, t_0) \mathbf{x}_0 + \left(\int_{t_0}^t \Phi(t, \tau) \mathbf{B}(\tau) \mathbf{u}(\tau) d\tau \right) \tag{4.15}$$

As explained in Chapter 2, the integral is numerically computed by means of a summation.

$$\mathbf{x}(t_n) = \Phi(t_n, t_0) \mathbf{x}_0 + \sum_{i=0}^{n-1} \Phi(t_{i+1}, t_i) \mathbf{B}(t_i) \mathbf{u}(t_i) \Delta t \tag{4.16}$$

Which corresponds to a constant acceleration along each Δt segment. If we define $\Psi(t_{i+1}, t_i) = \Phi(t_{i+1}, t_i) \mathbf{B}(t_i) \Delta t$, the control acceleration required from $\mathbf{x}(t_i)$ to $\mathbf{x}(t_{i+1})$ is calculated as:

$$\mathbf{u}(t_i) = \Psi(t_{i+1}, t_i)^{-1} (\mathbf{x}(t_{i+1}) - \Phi(t_{i+1}, t_i) \mathbf{x}(t_i)), \quad \text{for } i = 0, \dots, n-1 \tag{4.17}$$

Once the maneuver duration $T = t_n$ and the shape of the guidance profile $\mathbf{x}(t_i)$ are defined, the control acceleration can be determined, thereby establishing the guidance trajectory. Since the focus of this study is the final approach phase of the rendezvous mission, a straight-line path with constant acceleration along the direction of motion will be selected, as illustrated in Figure 4.3. While in the case of impulsive maneuvers the trapezoidal profile defined the trajectory of the sampled nodes where impulses are applied, here it represents the continuous acceleration, velocity, and position profiles along the direction of motion. The components perpendicular to the direction of motion are chosen to counterbalance gravitational forces, enabling the spacecraft to maintain the desired linear trajectory.

The guidance profile of the along-track component resembles Eqs.(4.10),(4.12),(4.14) with the exception that $\rho(t)$ is the actual path.

$$\rho(t) = \begin{cases} \frac{1}{2}a_{acc}t^2 & \text{for } 0 \leq t < T_{acc} \\ \frac{1}{2}a_{acc}T_{acc}^2 + a_{acc}T_{acc}t & \text{for } T_{acc} \leq t < (T_{acc} + T_{coast}) \\ \frac{3}{2}a_{acc}T_{acc}^2 + \frac{1}{2}a_{dec}t^2 & \text{for } (T_{acc} + T_{coast}) \leq t < T \end{cases} \quad (4.18)$$

$$\dot{\rho}(t) = \begin{cases} a_{acc}t & \text{for } 0 \leq t < T_{acc} \\ a_{acc}T_{acc} & \text{for } T_{acc} \leq t < (T_{acc} + T_{coast}) \\ a_{acc}T_{acc} + a_{dec}t & \text{for } (T_{acc} + T_{coast}) \leq t < T \end{cases}$$

Here, $T_{acc}, T_{coast}, T_{dec}, T$ are respectively the duration of the accelerating, coasting, decelerating glidslopes and the total duration of the manoeuvre. They are computed as:

$$\left\{ \begin{array}{l} T_{acc} = \sqrt{\frac{2(\rho_{f,acc} - \rho_0)}{a_{acc}}} \\ T_{dec} = \frac{\dot{\rho}_f - a_{acc}T_{acc}}{a_{dec}} \\ T_{coast} = \frac{\rho_0 - a_{acc}T_{acc}T_{dec} - 0.5a_{dec}T_{dec}^2 - \rho_{f,acc}}{a_{acc}T_{acc}} \\ T = T_{acc} + T_{coast} + T_{dec} \end{array} \right. \quad (4.19)$$

The profile can be fully defined by the selection of $\rho_{f,acc}, a_{acc}, a_{dec}$. The values of $\rho_0, \rho_f, \dot{\rho}_0, \dot{\rho}_f$ come from the initial and final conditions of the manoeuvre.

4.2. Feedback Control

This section describes the application of a feedback control law to the rendezvous dynamics. Data received from the guidance and navigation subsystems are compared to determine the state error, which is then used to compute the control gain. This gain generates the control action necessary to keep the satellite aligned with the reference trajectory.

4.2.1. Rendezvous Control Problem

The rendezvous control problem is described by the following state-space system:

$$\begin{cases} \dot{\mathbf{x}}_{6 \times 1} = \mathbf{A}_{6 \times 6}(t)\mathbf{x}_{6 \times 1}(t) + \mathbf{B}_{6 \times 3}(t)\mathbf{u}_{3 \times 1}(t) \\ \mathbf{y}_{6 \times 1}(t) = \mathbf{C}_{6 \times 6}\mathbf{x}_{6 \times 1}(t) + \mathbf{D}_{6 \times 3}\mathbf{u}_{3 \times 1}(t) \end{cases} \quad (4.20)$$

Here, $\mathbf{x}_{6 \times 1}(t)$ can represent either the Cartesian state or the qns-ROE, and the plant and input matrices can be time-varying or time-invariant based on the chosen dynamical formulation. The equations of motion are represented by a multi-input multi-output (MIMO) system with three inputs (control accelerations) and six outputs (the states to be controlled).

Cartesian-based Control Problem

The state-space representation of the Cartesian translational dynamics is:

$$\begin{cases} \dot{\mathbf{x}}(t) = \mathbf{A}(t)\mathbf{x}(t) + \mathbf{B}\mathbf{u}(t) \\ \mathbf{y}(t) = \mathbf{C}\mathbf{x}(t) + \mathbf{D}\mathbf{u}(t) \end{cases} \quad (4.21)$$

with

$$\mathbf{A}(t) = \mathbf{A}_{TH}(t), \quad \mathbf{B} = \mathbf{B}_{TH},$$

$$\mathbf{C} = \begin{bmatrix} 1 & 0 & 0 & 0 & 0 & 0 \\ 0 & 1 & 0 & 0 & 0 & 0 \\ 0 & 0 & 1 & 0 & 0 & 0 \\ 0 & 0 & 0 & 1 & 0 & 0 \\ 0 & 0 & 0 & 0 & 1 & 0 \\ 0 & 0 & 0 & 0 & 0 & 1 \end{bmatrix}, \quad \mathbf{D} = \begin{bmatrix} 0 & 0 & 0 \\ 0 & 0 & 0 \\ 0 & 0 & 0 \\ 0 & 0 & 0 \\ 0 & 0 & 0 \\ 0 & 0 & 0 \end{bmatrix}$$

Where $\mathbf{A}_{TH}(t)$ and \mathbf{B}_{TH} are fully detailed in Eq.(2.14). The system is linear time-varying

(LTV), as the plant matrix $\mathbf{A}(t)$ depends on the norm of the angular velocity vector, which varies with time for eccentric orbits. The input matrix \mathbf{B} remains constant. For circular orbits, the angular velocity is constant, and the system dynamics are governed by the Hill-Clohessy-Wiltshire (HCW) equations (Eq.(2.16)). In this case, the plant matrix is time-invariant, and the system becomes linear time-invariant (LTI).

Due to its linear time-invariant (LTI) nature, the controllability of the circular, Cartesian-based problem can be assessed using the controllability matrix [45]:

$$\mathcal{C} = \begin{bmatrix} \mathbf{B} & \mathbf{AB} & \mathbf{A}^2\mathbf{B} & \mathbf{A}^3\mathbf{B} & \mathbf{A}^4\mathbf{B} & \mathbf{A}^5\mathbf{B} \end{bmatrix} \in \mathbb{R}^{6 \times 18} \quad (4.22)$$

The system is considered **controllable** if the controllability matrix \mathcal{C} has full rank, that is,

$$\text{rank}(\mathcal{C}) = 6$$

In contrast, the controllability of the eccentric, Cartesian-based problem cannot be evaluated using the controllability matrix due to its time-varying nature (LTV). Instead, the controllability Gramian is employed, as it is more suitable for analyzing the controllability of linear time-varying systems:

$$\mathbf{W}_c(t_0, t_f) = \int_{t_0}^{t_f} \Phi(t, \tau) \mathbf{B} \mathbf{B}^\top \Phi^\top(t, \tau) d\tau \in \mathbb{R}^{6 \times 6} \quad (4.23)$$

In this case, the input matrix is time-invariant, as the Cartesian-based formulation is being considered. The system is considered **controllable** if the controllability Gramian is positive definite, that is,

$$\mathbf{W}_c(t_0, t_f) > \mathbf{0}$$

ROE-based Control Problem

The state-space representation of the ROE-based translational dynamics is:

$$\begin{cases} \delta\dot{\boldsymbol{\alpha}}(t) = \mathbf{A}\delta\boldsymbol{\alpha}(t) + \mathbf{B}(t)\mathbf{u}(t) \\ \mathbf{y}(t) = \mathbf{C}\delta\boldsymbol{\alpha}(t) + \mathbf{D}\mathbf{u}(t) \end{cases} \quad (4.24)$$

with

$$\mathbf{A} = \mathbf{A}_{ROE}, \quad \mathbf{B} = \mathbf{B}_{ROE}(t),$$

$$\mathbf{C} = \begin{bmatrix} 1 & 0 & 0 & 0 & 0 & 0 \\ 0 & 1 & 0 & 0 & 0 & 0 \\ 0 & 0 & 1 & 0 & 0 & 0 \\ 0 & 0 & 0 & 1 & 0 & 0 \\ 0 & 0 & 0 & 0 & 1 & 0 \\ 0 & 0 & 0 & 0 & 0 & 1 \end{bmatrix}, \quad \mathbf{D} = \begin{bmatrix} 0 & 0 & 0 \\ 0 & 0 & 0 \\ 0 & 0 & 0 \\ 0 & 0 & 0 \\ 0 & 0 & 0 \\ 0 & 0 & 0 \end{bmatrix}$$

Where \mathbf{A}_{ROE} and $\mathbf{B}_{ROE}(t)$ are fully detailed in Eq.(2.54). Unlike the Cartesian formulation, the time dependence in the ROE-based system appears in the input matrix $\mathbf{B}(t)$, due to its dependence on the true anomaly (or the mean anomaly when eccentricity is zero). Consequently, the system remains linear time-varying (LTV) regardless of whether the orbit is circular or eccentric.

The controllability of the ROE-based problem cannot be evaluated using the controllability matrix due to the time dependence of the input matrix. Instead, the controllability Gramian is employed:

$$\mathbf{W}_c(t_0, t_f) = \int_{t_0}^{t_f} \Phi(t, \tau) \mathbf{B}(\tau) \mathbf{B}^\top(\tau) \Phi^\top(t, \tau) d\tau \in \mathbb{R}^{6 \times 6} \quad (4.25)$$

In contrast with the eccentric Cartesian-based formulation, the input matrix is time-dependent. As previously mentioned, the system is considered **controllable** if the controllability Gramian is positive definite.

4.2.2. Linear Optimal Control

In spacecraft control applications, optimizing system performance in the time domain is often essential. The primary objective is to design a control law that guarantees system stability, desirable transient behavior, and efficient use of control effort [7, 42].

A common cost function to be minimized is expressed as:

$$J = \int_0^{t_f} \mathbf{x}^\top \mathbf{x} dt$$

However, to limit excessive control inputs—which could demand large actuator capabilities, the cost function is extended to penalize control effort:

$$J = \int_0^{t_f} (\mathbf{x}^\top \mathbf{x} + \mathbf{u}^\top \mathbf{u}) dt$$

To further tailor the trade-off between state regulation and control usage, weighting matrices are introduced:

$$J = \int_0^{t_f} (\mathbf{x}^\top \mathbf{Q} \mathbf{x} + \mathbf{u}^\top \mathbf{R} \mathbf{u}) dt$$

where:

- \mathbf{Q} is the state weighting matrix, symmetric and positive semi-definite,
- \mathbf{R} is the control weighting matrix, symmetric and positive definite.

These weighting matrices enable expressing the relative importance of different state variables and control inputs, accounting for varying physical units such as radians and Newtons.

The optimal control problem thus consists of minimizing the quadratic cost function with an optional terminal state penalty:

$$J_0 = \frac{1}{2} \mathbf{x}_f^\top \mathbf{S} \mathbf{x}_f + \frac{1}{2} \int_0^{t_f} (\mathbf{x}^\top \mathbf{Q} \mathbf{x} + \mathbf{u}^\top \mathbf{R} \mathbf{u}) dt$$

subject to the system dynamics:

$$\dot{\mathbf{x}} = \mathbf{A}\mathbf{x} + \mathbf{B}\mathbf{u}$$

To enforce the system dynamics constraint, Lagrange multipliers λ are introduced, defining the augmented cost function:

$$J = \frac{1}{2} \mathbf{x}_f^\top \mathbf{S} \mathbf{x}_f + \frac{1}{2} \int_0^{t_f} (\mathbf{x}^\top \mathbf{Q} \mathbf{x} + \mathbf{u}^\top \mathbf{R} \mathbf{u} + 2\lambda^\top (\mathbf{A}\mathbf{x} + \mathbf{B}\mathbf{u} - \dot{\mathbf{x}})) dt$$

The minimization of J with respect to \mathbf{u} , \mathbf{x} , and λ leads to the following optimality conditions:

- **With respect to \mathbf{u} :**

$$\frac{\partial J}{\partial \mathbf{u}} = \mathbf{R}\mathbf{u} + \mathbf{B}^\top \lambda = \mathbf{0} \quad \Rightarrow \quad \mathbf{u} = -\mathbf{R}^{-1}\mathbf{B}^\top \lambda$$

- With respect to λ :

$$\frac{\partial J}{\partial \lambda} = \mathbf{Ax} + \mathbf{Bu} - \dot{\mathbf{x}} = \mathbf{0} \quad \Rightarrow \quad \dot{\mathbf{x}} = \mathbf{Ax} + \mathbf{Bu}$$

- With respect to \mathbf{x} :

$$\dot{\lambda} = -\mathbf{A}^\top \lambda - \mathbf{Qx}$$

These conditions form a two-point boundary value problem:

$$\begin{cases} \dot{\mathbf{x}} = \mathbf{Ax} + \mathbf{Bu} \\ \dot{\lambda} = -\mathbf{A}^\top \lambda - \mathbf{Qx} \\ \mathbf{u} = -\mathbf{R}^{-1}\mathbf{B}^\top \lambda \end{cases}$$

To recast the solution into a feedback form, we posit:

$$\lambda = \mathbf{Px}$$

Substituting into the control law yields:

$$\mathbf{u} = -\mathbf{R}^{-1}\mathbf{B}^\top \mathbf{Px}$$

Differentiating $\lambda = \mathbf{Px}$ with respect to time and applying the chain rule leads to:

$$\dot{\lambda} = \dot{\mathbf{P}}\mathbf{x} + \mathbf{Px}$$

Replacing $\dot{\lambda}$ and $\dot{\mathbf{x}}$ using the optimality conditions provides:

$$\dot{\mathbf{P}}\mathbf{x} + \mathbf{P}(\mathbf{Ax} + \mathbf{Bu}) = -\mathbf{A}^\top \mathbf{Px} - \mathbf{Qx}$$

Substituting $\mathbf{u} = -\mathbf{R}^{-1}\mathbf{B}^\top \mathbf{Px}$, and simplifying, yields the Differential Riccati Equation (DRE):

$$\dot{\mathbf{P}} = -\mathbf{A}^\top \mathbf{P} - \mathbf{PA} - \mathbf{Q} + \mathbf{PBR}^{-1}\mathbf{B}^\top \mathbf{P} \quad (4.26)$$

subject to the terminal condition:

$$\mathbf{P}(t_f) = \mathbf{S}$$

The DRE is typically solved by backward integration from t_f to t_0 . For infinite-horizon problems ($t_f \rightarrow \infty$), it is assumed that \mathbf{P} converges to a steady-state solution satisfying the Algebraic Riccati Equation (ARE):

$$\mathbf{0} = -\mathbf{A}^\top \mathbf{P} - \mathbf{P}\mathbf{A} - \mathbf{Q} + \mathbf{P}\mathbf{B}\mathbf{R}^{-1}\mathbf{B}^\top \mathbf{P} \quad (4.27)$$

Consequently, the optimal feedback control law becomes:

$$\mathbf{u} = -\mathbf{K}\mathbf{x}, \quad \mathbf{K} = \mathbf{R}^{-1}\mathbf{B}^\top \mathbf{P} \quad (4.28)$$

This yields a time-invariant optimal control strategy, well-suited for infinite-horizon regulation problems, where \mathbf{P} is the stabilizing solution to the ARE and \mathbf{K} is the constant state feedback gain.

4.2.3. Reference Tracking with LQR

As described in Section 3.2, the feedback controller, using data from the navigation filter, modifies the reference acceleration in order to track the reference state provided by the guidance block. Since we are operating within a regulator framework, which computes the control gain that minimizes the state (driving it to zero), we must work with the *error dynamics* [3, 5].

$$\begin{cases} \dot{\mathbf{x}}(t) = \mathbf{A}(t)\mathbf{x}(t) + \mathbf{B}(t)\mathbf{u}(t) \\ \mathbf{y}(t) = \mathbf{C}\mathbf{x}(t) + \mathbf{D}\mathbf{u}(t) \end{cases}, \quad \begin{cases} \dot{\mathbf{x}}_r(t) = \mathbf{A}(t)\mathbf{x}_r(t) + \mathbf{B}(t)\mathbf{u}_r(t) \\ \mathbf{y}_r(t) = \mathbf{C}\mathbf{x}_r(t) + \mathbf{D}\mathbf{u}_r(t) \end{cases} \quad (4.29)$$

Here, the subscript r refers to the dynamics of the *reference system*. We define the *state error* and *output error* as:

$$\mathbf{e}(t) = \mathbf{x}(t) - \mathbf{x}_r(t), \quad \boldsymbol{\epsilon}(t) = \mathbf{y}(t) - \mathbf{y}_r(t)$$

The corresponding error dynamics and output equations become:

$$\begin{cases} \dot{\mathbf{e}}(t) = \dot{\mathbf{x}}(t) - \dot{\mathbf{x}}_r(t) = \mathbf{A}(t)(\mathbf{x}(t) - \mathbf{x}_r(t)) + \mathbf{B}(t)(\mathbf{u}(t) - \mathbf{u}_r(t)) \\ \boldsymbol{\epsilon}(t) = \mathbf{C}(\mathbf{x}(t) - \mathbf{x}_r(t)) + \mathbf{D}(\mathbf{u}(t) - \mathbf{u}_r(t)) \end{cases} \quad (4.30)$$

Which simplifies to:

$$\begin{cases} \dot{\mathbf{e}}(t) = \mathbf{A}(t)\mathbf{e}(t) + \mathbf{B}(t)\Delta\mathbf{u}(t) \\ \mathbf{e}(t) = \mathbf{C}\mathbf{e}(t) + \mathbf{D}\Delta\mathbf{u}(t) \end{cases} \quad (4.31)$$

Finally, the LQR controller is employed to minimize the new state $\mathbf{e}(t)$, and the control law is given by:

$$\Delta\mathbf{u}(t) = -\mathbf{K}(t)\mathbf{e}(t) \Rightarrow \mathbf{u}(t) = -\mathbf{K}(t)\mathbf{e}(t) + \mathbf{u}_r(t) \quad (4.32)$$

Here, the reference acceleration $\mathbf{u}_r(t)$ is provided by the guidance algorithm, while the “new state” $\mathbf{e}(t)$ corresponds to the feedback error. This feedback error is a state vector comprising both position and its time derivative (velocity), resulting in a proportional-derivative (PD) control structure determined by the gain matrix. This configuration is well-suited to the rendezvous dynamics, which exhibits low frequency poles in the components of the frequency response function, effectively acting as integrators. Consequently, an additional integral action is not required, and the proportional-derivative structure delivers satisfactory performance [16]. This rationale supported the adoption of a standard Linear Quadratic Regulator (LQR) approach over a Linear Quadratic Integrator (LQI) design [49], the latter aiming to reduce steady-state error by incorporating integral action. The final control architecture thus consists of a proportional-derivative controller augmented by a *feedforward* term derived from the guidance profile. When an impulsive guidance is considered, the guidance function provides not acceleration but the velocity variation $\Delta\mathbf{V}$. To align this information with the controller algorithm and the discretized thruster logic, the $\Delta\mathbf{V}$ is converted into an equivalent acceleration using:

$$\mathbf{u}_r = \frac{\Delta\mathbf{V}}{t_{disc}} \quad (4.33)$$

Here, t_{disc} denotes the discretization time chosen for the PWM logic. The resulting action corresponds to a constant acceleration applied over this time interval, effectively reproducing a pulse-like behavior.

4.2.4. LQR Control of Rendezvous Dynamics

The solution of the LQR problem depends on the characteristics of the system to be controlled. Eq. (4.26) can be analyzed based on the considerations introduced in Section 4.2.1.

- **Cartesian-Based Circular Dynamics:** The Cartesian-based formulation of the rendezvous dynamics with a circular orbit of the target vehicle is represented by a linear time-invariant (LTI) system. Therefore, the control gain obtained from the steady-state solution of the DRE backward integration is constant. This solution can be computed through the corresponding Algebraic Riccati Equation (ARE), assuming an infinite time horizon.

- **Cartesian-Based Eccentric Dynamics:**

In this case, the state-space system is linear time-varying (LTV) due to the time dependence of the plant matrix. The differential Riccati equation becomes:

$$\dot{\mathbf{P}}(t) = -\mathbf{A}(t)^\top \mathbf{P}(t) - \mathbf{P}(t)\mathbf{A}(t) - \mathbf{Q} + \mathbf{P}(t)\mathbf{B}\mathbf{R}^{-1}\mathbf{B}^\top \mathbf{P}(t) \quad (4.34)$$

By considering constant weighting matrices, the time dependence of the plant matrix results in a time-varying control gain. In this study, two potential solutions to the DRE, Eq. (4.34), are proposed:

1. *Numerical Integration Approach:*

An intuitive method for solving the DRE involves direct numerical integration. The matrix form of the DRE is transformed into an equivalent vectorized form. Since the matrix \mathbf{P} is 6×6 , this transformation yields a system of 36 coupled differential equations, which are numerically integrated in *MATLAB*.

For non-stiff problems, explicit Runge-Kutta methods such as RK45 can be effectively employed. However, the DRE is often a stiff initial value problem (IVP) [12], in which case an implicit integrator is more suitable. The *MATLAB* function *ode15s* is well-suited for stiff problems and offers improved precision compared to other solvers. It is therefore adopted here in place of *ode45* to integrate the DRE, as recommended in the solver selection guidelines provided by MathWorks [29].

2. *Discretized periodic infinite horizon:*

The second approach exploits the structure of the plant matrix, specifically its time-periodic nature due to the angular velocity $\boldsymbol{\omega}$, which varies periodically in a Keplerian orbit. As a result, the system can be classified as linear time-periodic (LTP). For such systems, the infinite-horizon LQR problem admits a periodic steady-state solution [11, 32, 38], as the solution to the associated Periodic Riccati Equation (PRE) converges to a time-periodic function.

To compute this solution, the orbital period is discretized into N intervals of

duration Δt . At each time step, the system is treated as time-invariant over Δt , and an Algebraic Riccati Equation (ARE) is solved. This yields a sequence of time-varying control gains that repeat each orbital period, forming an effective periodic infinite-horizon controller. Therefore:

$$0 = -\mathbf{A}(t_n)^\top \mathbf{P}(t_n) - \mathbf{P}(t_n)\mathbf{A}(t_n) - \mathbf{Q} + \mathbf{P}(t_n)\mathbf{B}\mathbf{R}^{-1}\mathbf{B}^\top \mathbf{P}(t_n), \quad (4.35)$$

for $n = 1, \dots, N$

The choice of N depends on the desired accuracy. In this study, it is determined experimentally by simulating the results and comparing them with the numerical integration described in the previous approach.

- **ROE-based dynamics:** in the ROE-based formulation of relative motion dynamics, the system can be represented as a Linear Time-Varying (LTV) system for both circular and eccentric reference orbits. As previously noted, the plant matrix remains constant, while the input matrix varies with time due to its dependence on the true anomaly. Given that the true anomaly evolves periodically in a Keplerian orbit, the resulting system is Linear Time-Periodic (LTP). As with the Cartesian-based eccentric dynamics, this time-periodicity implies that the solution of the differential Riccati equation (DRE) will converge to a periodic steady-state solution. To obtain this solution, the DRE is numerically integrated using the *MATLAB* function *ode15s*, which is well-suited for stiff systems. The resulting periodic solution is then used to define the time-varying control gain along the orbital period.
- **Rotational dynamics:** As previously discussed, the system exhibits linear time-varying (LTV) behavior, but tends to approach a linear time-invariant (LTI) form in the case of circular orbits. Consequently, as with the Cartesian-based controller, a simplified infinite-horizon solution derived from the Algebraic Riccati Equation (ARE) can be used when the orbit eccentricity is zero. In contrast, for eccentric orbits, the periodic solution of the Riccati Differential Equation (RDE) is employed. Both control strategies introduced for the Cartesian-based controller remain applicable in this context.

5 | Simulations and Case Studies

This chapter presents the case studies used to analyze the algorithms described in the previous sections. The primary focus is on the final approach phase of a rendezvous and docking (RV&D) mission, although a formation flying scenario is also considered. The guidance reference trajectory is generated using a Cartesian formulation of the equations of motion, as Cartesian coordinates are typically more suitable for analyzing the final approach phase. The controller is evaluated using both Cartesian-based and ROE-based dynamics to assess performance and determine their suitability for the scenarios under investigation. Translational dynamics are controlled via thrusters, while for rotational dynamics, no actuators are modeled; instead, the ideal control action generated by the feedback controller is directly applied to the system dynamics.

The following experiments are carried out:

- Control gain tuning with the target in a circular orbit;
- RV&D using impulsive guidance;
- RV&D using continuous guidance;
- Formation flying using an eccentricity/inclination separation orbit.

The first experiment investigates gain computation and control behavior in a simplified circular orbit scenario, serving as a baseline for comparison with more general eccentric cases. The second and third experiments provide a complete analysis of guidance profile design, control gain behavior, and mission performance in eccentric orbits using both impulsive and continuous guidance schemes, with Cartesian-based and ROE-based controllers. Finally, the last experiment simulates a transition from a position along the target's orbit to an eccentricity/inclination separation orbit in a formation flying scenario. In the latter, ideal control of the translational dynamics is assumed as explained in Section 3.2.3.

5.1. Hypothesis and Data Selection

The mission scenario considered involves a rendezvous operation with the International Space Station (ISS) [16, 31]. Accordingly, the ISS is selected as the target vehicle. The chaser vehicle is chosen from among those that routinely conduct rendezvous operations with the ISS; in this case, data from the Soyuz spacecraft are used [15]. It is important to emphasize that the objective is not to replicate a real mission, but rather to utilize existing spacecraft data to evaluate the performance of the algorithms described.

5.1.1. Target Vehicle

The orbit of the ISS is retrieved from real-time data [33]. The orbital elements are provided for the current Central European Summer Time (CEST), specifically at **16:42 (4:42 PM), June 1, 2025**, as shown in Table 5.1. In particular, the elements i , Ω , ω , and M are kept constant across all study cases. The eccentricity, however, is varied to assess the algorithm's performance under different orbital configurations. Consequently, by maintaining a fixed pericenter radius, the semi-major axis is adjusted accordingly as the eccentricity changes.

Parameter	Value
Pericenter altitude [km]	416
Eccentricity [-]	Simulation-specific
Inclination [deg]	51.6366
RAAN [deg]	27.8423
Argument of pericenter [deg]	174.0070
Mean anomaly [deg]	186.0942

Table 5.1: ISS orbital data

The target vehicle's body frame is defined such that the x -axis aligns with the docking axis (line-of-sigh). A direction cosine matrix (DCM) is derived from a sequence of 321 Euler rotations transforming the LVLH frame into the target's body frame (see Eq. (2.66)). The chosen Euler angles for this transformation are:

Parameter	Value
θ_x [deg]	0
θ_y [deg]	−30
θ_z [deg]	20

Table 5.2: Target body frame attitude with respect to LVLH

The resulting DCM from LVLH to the body frame is:

$$\mathbf{A}_{t/lvlh} = \begin{bmatrix} 0.8138 & 0.2962 & 0.5 \\ -0.3420 & 0.9397 & 0 \\ -0.4699 & -0.1710 & 0.8660 \end{bmatrix} \quad (5.1)$$

Here, $\mathbf{A}_{t/lvlh}$ represents the direction cosine matrix (DCM) that rotates a vector from the LVLH frame to the body frame. As stated in Section 2.4, the target's attitude relative to its LVLH frame is assumed constant throughout the maneuver to prevent coupling between translational and rotational dynamics. The target spacecraft rotates with the natural orbital angular velocity, defined as:

$$\omega_t(t) = \frac{\|\mathbf{r}(t) \times \mathbf{v}(t)\|}{\|\mathbf{r}(t)\|^2}$$

$$\boldsymbol{\omega}_t^{lvlh}(t) = \begin{bmatrix} 0 \\ -\omega_t(t) \\ 0 \end{bmatrix} \quad (5.2)$$

Here, \mathbf{r} and \mathbf{v} are the position and velocity vectors in the ECI frame, while $\boldsymbol{\omega}_t^{lvlh}$ is the angular velocity of the target in the LVLH frame. In the case of a circular orbit, the angular velocity is constant and given by:

$$\omega_t = \sqrt{\frac{\mu}{a_t^3}} \quad (5.3)$$

In the target's body frame, the angular velocity is:

$$\boldsymbol{\omega}_t^t(t) = \mathbf{A}_{t/lvlh} \boldsymbol{\omega}_t^{lvlh}(t) \quad (5.4)$$

Here, $\boldsymbol{\omega}_t^t$ denotes the angular velocity expressed in the target's body frame.

To fully define the satellite's motion, additional inertial and geometrical data are required. Specifically, the satellite's mass is necessary for modeling the perturbed two-body problem, and the inertia tensor is needed for integrating Euler's rotational equations (see Section 3.1). According to the assumptions in Section 2.4, the body frame is aligned with the principal axes of inertia, resulting in a diagonal inertia tensor. The geometric shape is also used to compute the ballistic coefficient, which affects the aerodynamic drag disturbance (see Section 3.1). The inertia tensor and cross-sectional area are obtained from ISS datasheets [16], while the drag coefficient is selected based on reference values [14].

Parameter	Value
Mass [kg]	470000
Principal moments of inertia [$\text{kg}\cdot\text{m}^2$]	$I_{xx} = 128 \times 10^6$ $I_{yy} = 107 \times 10^6$ $I_{zz} = 201 \times 10^6$
Dimensions [m]	$x = 67.5$ $y = 108.48$ $z = 44.98$
Drag coefficient [-]	2.07

Table 5.3: ISS inertial and geometrical data

For the purposes of this study, the approach ellipsoid, defined as the region within which the final approach is actively controlled, is approximated as a sphere with a radius of 200 m. When the chaser vehicle enters this region, the approach maneuver is initiated. For Soyuz-type missions, the docking axis is typically aligned along the $-\mathbf{V}$ -bar, \mathbf{R} -bar, or $-\mathbf{R}$ -bar directions. However, in this study, the docking axis is intentionally modeled as misaligned with respect to both the \mathbf{V} -bar and \mathbf{R} -bar, introducing a nonzero angle with the LVLH frame. This modeling choice generalizes the scenario and enables analysis of the controller's response in both in-plane and out-of-plane components. An additional critical constraint is the maximum allowable docking velocity, set to 0.1 m/s [16]. A summary of the RV&D scenario parameters is provided in Table 5.4.

Parameter	Value
Approach ellipsoid radius [m]	200
Maximum docking velocity [m/s]	0.1

Table 5.4: RV&D scenario data

The desired final state of the chaser relative to the target, as defined by the docking requirements (see Table 5.4), is:

$$\mathbf{x}^t(t_f) = [0, 0, 0, 0.1, 0, 0]^\top \quad (5.5)$$

This state is defined in the rotated frame aligned with the docking axis, which corresponds to the target body frame. The equivalent coordinates in the LVLH frame are computed as:

$$\mathbf{x}^{lvlh}(t_f) = \mathbf{A}_{lvlh/t} \mathbf{x}^t(t_f) = [0, 0, 0, 0.0814, 0.0296, 0.05]^\top \quad (5.6)$$

5.1.2. Chaser Vehicle

The initial orbit of the Soyuz spacecraft is defined based on its relative position with respect to the ISS. This position varies across the different study cases and will be discussed in the following sections of this chapter. As with the ISS, inertial and geometrical data are required to define the position and attitude of the spacecraft, as well as to model the aerodynamic disturbance. The mass, dimensions, and principal moments of inertia are obtained from known datasheets [16], while the drag coefficient is selected by approximating the Soyuz as a long cylindrical body [35].

Parameter	Value
Mass [kg]	6850
Principal moments of inertia [kg·m ²]	$I_{xx} = 5300$ $I_{yy} = 33000$ $I_{zz} = 33000$
Dimensions [m]	Length = 7.5 Diameter = 2.7
Drag coefficient [-]	0.82

Table 5.5: Soyuz inertial and geometrical data

The principal moments of inertia I_{yy} and I_{zz} reflect the symmetry of the satellite, which plays an important role in canceling certain components of Eq. (2.85).

The thrusters are selected to match the size and mass of the spacecraft, as well as the acceleration requirements for the maneuvers. Data for the monopropellant thruster *MONARC-90HT* [30] are chosen, as the thrust level provided by this engine aligns with the recommended thrust level for the Soyuz, as specified in Ref. [16]. Its datasheet is reported in Table 5.6.

Parameter	Value
Steady-state thrust [N]	111
Specific impulse [s]	234.0
Minimum impulse bit [Ns]	1.16

Table 5.6: MONARC-90HT datasheet

From the MIB and thrust level, the minimum allowed firing time can be defined as:

$$t_{\text{fire,min}} = \frac{\text{MIB}}{T} = 0.0105 \text{ [s]} \quad (5.7)$$

Thrusters with shorter durations are not commanded directly but are accumulated, as described in Section 3.2.3.

The thruster configuration does not replicate the actual placement used in real Soyuz missions. Since the main objective of incorporating thruster logic into the algorithm is to

study the controller's response to the error introduced by converting ideal control actions into real ones via pulse-width modulation, rather than to model the exact thruster layout, the simplest configuration is selected. Specifically, *six thrusters* are employed, each aligned with the spacecraft's center of mass and oriented along the six principal directions ($+x$, $+y$, $+z$, $-x$, $-y$, $-z$).

5.2. Test 1: Control Gain Tuning with the Target in a Circular Orbit

Equations of Motion

The first study case focuses on analyzing the control gain tuning, assuming the target is on a circular orbit. The data in Table 5.1 is completed here by specifying the eccentricity value:

Parameter	Value
Eccentricity [-]	10^{-6}

Table 5.7: ISS eccentricity for near-circular orbit

It is important to note that the orbit is near-circular but not perfectly circular. This choice is motivated by the need to avoid significant errors when converting Cartesian state vectors into Keplerian orbital elements. The conversion algorithm used yields acceptable accuracy for eccentricity values as low as approximately 10^{-9} [17]. The set of orbital elements is now fully defined and can be used to compute the target's absolute state, which is required to define the Cartesian equations of relative motion (see Eq.(2.14)).

Due to the low eccentricity, the in-plane angular velocity components are negligible compared to the out-of-plane component, allowing the angular velocity vector to be approximated as:

$$\boldsymbol{\omega}_t^{lwh} = \begin{bmatrix} 0 \\ -\sqrt{\frac{\mu}{a_t^3}} \\ 0 \end{bmatrix} = \begin{bmatrix} 0 \\ -1.126 \times 10^{-3} \\ 0 \end{bmatrix} [\text{rad/s}] \quad (5.8)$$

In the target's body frame, this angular velocity is expressed as:

$$\boldsymbol{\omega}_t^t = \mathbf{A}_{t/lvlh} \boldsymbol{\omega}_t^{lvlh} = \begin{bmatrix} -3.336 \times 10^{-4} \\ -1.057 \times 10^{-3} \\ 1.926 \times 10^{-4} \end{bmatrix} [\text{rad/s}] \quad (5.9)$$

These values are used to define the translational equations of relative motion (see Eq. (2.85)).

Feedback Controller

This section outlines the selection of the weight matrices used in the generation of the control gains. The initial values are chosen using Bryson's Rule [7], and subsequently refined through an iterative trial-and-error process. This refinement takes into account the differing orders of magnitude among the state and input variables in the system equations. An important factor in the tuning process is the interaction between the controller and the thruster duty cycle: selecting a controller with excessively tight tracking performance may result in high thruster activity, leading to impractically frequent firings given the selected guidance profile. Therefore, a trade-off must be found between tracking accuracy and actuation feasibility.

- **Cartesian-based controller:** The matrices are defined in the rotated frame aligned with the docking axis. Equal weights are assigned to the propagated and final state errors, as the objective is to minimize the error over the entire trajectory, not only at the final time.

$$\mathbf{Q} = \mathbf{I}_{6 \times 6}, \quad \mathbf{R} = 1 \times 10^8 \cdot \text{diag}([1, 1, 1]), \quad \mathbf{S} = \mathbf{Q} \quad (5.10)$$

- **ROE-based controller:** To ensure a consistent comparison with the Cartesian-based formulation in terms of magnitude, a scaled version of the quasi-nonsingular (qns) ROE dynamics is employed. The scaling is performed using the semi-major axis a_t :

$$a_t \delta \dot{\boldsymbol{\alpha}}_{qns} = a_t \mathbf{A} \delta \boldsymbol{\alpha}_{qns} + a_t \mathbf{B} \mathbf{u}_c \quad (5.11)$$

The weight matrices are chosen accordingly for the scaled system:

$$\mathbf{Q} = \mathbf{I}_{6 \times 6}, \quad \mathbf{R} = 5 \times 10^9 \cdot \text{diag}([1, 1, 1]), \quad \mathbf{S} = \mathbf{Q} \quad (5.12)$$

- **Attitude controller:** The weights for the attitude controller prioritize attitude

accuracy, with relatively lower penalty on the control effort:

$$\mathbf{Q} = 10^8 \cdot \text{diag}([1, 1, 1, 1, 1, 1]), \quad \mathbf{R} = \mathbf{I}_{3 \times 3}, \quad \mathbf{S} = \mathbf{Q} \quad (5.13)$$

5.3. Test 2: RV&D using Impulsive Guidance

Equations of Motion

The second case study focuses on analyzing the final approach phase of a rendezvous and docking (RV&D) mission, assuming the target is on an eccentric orbit. As previously discussed in Section 5.1, the guidance reference trajectory is generated using a Cartesian-based algorithm, and both Cartesian-based and ROE-based controllers are evaluated. The parameters in Table 5.1 are now extended to include the eccentricity of the orbit:

Parameter	Value
Eccentricity [-]	0.2

Table 5.8: ISS eccentricity

For non-zero eccentricities, the angular velocity of the target varies with time and its time evolution is computed using Eqs. (5.2) and (5.4). With these values defined, both the translational and rotational equations of motion can now be fully specified (see Eqs. (2.14) and (2.85)).

Initial Relative State

The initial relative state of the chaser is selected to lie on the boundary of the Approach Ellipsoid defined for the ISS (see Section 5.1.1). To generalize the analysis for any point along the ellipsoid's surface, a skew angle is introduced between the docking axis and the Local Vertical Local Horizontal (LVLH) frame of the target. The chaser initiates its maneuver from a hold point located along the docking axis. The initial position is therefore derived from the known radius of the Approach Ellipsoid and the defined docking axis orientation (see Table 5.2).

The initial relative velocity is set to zero, so that the chaser begins by accelerating toward the target, then decelerates to satisfy the final docking velocity constraint. The initial

chaser state, expressed in the rotated frame aligned with the docking axis, is defined as:

$$\mathbf{x}^t(t_0) = [-200, 0, 0, 0, 0, 0]^\top \quad (5.14)$$

Here, \mathbf{x}^t denotes the chaser's relative position and velocity with respect to the target, expressed in the rotated docking frame. The equivalent representation in the standard LVLH frame is given by:

$$\mathbf{x}^{lvlh}(t_0) = \mathbf{A}_{lvlh/t}\mathbf{x}^t(t_0) = [-162.76, -59.24, -100, 0, 0, 0]^\top \quad (5.15)$$

The chaser's initial attitude and angular velocity are set to match those of the target, yielding a null initial attitude and angular velocity error. This is defined as:

$$\begin{aligned} \mathbf{A}_{c/t}(t_0) &= \mathbf{I}_{3 \times 3} \\ \boldsymbol{\omega}_c^t(t_0) &= \mathbf{A}_{c/t}(t_0)\boldsymbol{\omega}_t^t(t_0) = \boldsymbol{\omega}_t^t(t_0) \end{aligned} \quad (5.16)$$

Here, $\mathbf{A}_{c/t}(t_0)$ is the rotation matrix from the target's body frame to the chaser's body frame, and $\boldsymbol{\omega}_c^t$ is the angular velocity of the chaser expressed in its own body frame.

Guidance Profile

As stated in Section 4.1, the definition of both impulsive and continuous guidance profiles requires the parameters ρ_0 , ρ_f , $\dot{\rho}_0$, and $\dot{\rho}_f$, which are derived from the initial and final conditions. These represent, respectively, the initial and final distances from the starting point along the docking axis, and the corresponding initial and final velocities in that direction.

Parameter	Value
ρ_0 [m]	0
ρ_f [m]	200
$\dot{\rho}_0$ [m/s]	0
$\dot{\rho}_f$ [m/s]	0.1

Table 5.9: Parameters based on initial and final state

The methodology used to generate the guidance reference profile is described in Section 4.1. In this section, we focus on the specific values selected to fully define the

impulsive guidance profile. These parameters are summarized in Table 5.10.

Parameter	Value
$\rho_{f,acc}$ [m]	70
a_{acc} [m/s ²]	0.0002
N_{acc} [-]	20
N_{coast} [-]	5

Table 5.10: Parameters for impulsive guidance profile

Feedback Controller

To allow a meaningful comparison between the control gain shapes in the circular and eccentric cases, the weight matrices are selected identically to those presented in Section 5.2.

5.4. Test 3: RV&D using Continuous Guidance

For a meaningful comparison between the impulsive and continuous guidance scenarios, the target orbital data as well as the initial and final relative states are selected as defined in Section 5.3. However, the weight matrices used to tune the control gains are adjusted to better match the smoother, more continuous control effort required by this guidance profile.

Guidance Profile

As stated in Section 4.1, both impulsive and continuous guidance profiles require the parameters ρ_0 , ρ_f , $\dot{\rho}_0$, and $\dot{\rho}_f$, which are derived from the initial and final conditions. These values are chosen as described in Table 5.9. The parameters employed for the construction of the continuous guidance profile are listed in Table 5.11.

Parameter	Value
$\rho_{f,acc}$ [m]	70
a_{acc} [m/s ²]	0.0055
a_{dec} [m/s ²]	-0.0055

Table 5.11: Parameters: continuous guidance

Feedback Controller

The same attitude controller used in the previous experiments is adopted here. However, the weight matrices for the Cartesian-based and ROE-based translational controllers are modified to reflect the more continuous nature of the control action required in this scenario.

- **Cartesian-based controller:**

$$\mathbf{Q} = \mathbf{I}_{6 \times 6}, \quad \mathbf{R} = 1 \times 10^6 \cdot \text{diag}([1, 1, 1]), \quad \mathbf{S} = \mathbf{Q} \quad (5.17)$$

- **ROE-based controller:**

$$\mathbf{Q} = \mathbf{I}_{6 \times 6}, \quad \mathbf{R} = 5 \times 10^7 \cdot \text{diag}([1, 1, 1]), \quad \mathbf{S} = \mathbf{Q} \quad (5.18)$$

5.5. Test 4: Formation Flying using e/i Separation Orbit

In the context of formation flying and proximity operations, it is essential to maintain a safe, bounded, and controllable relative motion between spacecraft. Traditional approaches based on Cartesian coordinates (position and velocity) can be unintuitive and computationally burdensome for design and long-term stability analysis. An alternative, more geometrically insightful method is the use of eccentricity/inclination (e/i) vector separation.

The primary motivation for adopting an e/i separation orbit is collision avoidance. In practice, along-track separation, governed by differences in mean argument of latitude and semi-major axis, is the most uncertain and susceptible to drift due to errors in maneuver execution and orbit determination. By deliberately offsetting the radial and cross-track components, e/i vector separation ensures that the satellites are never aligned simultaneously in all three dimensions [9].

The separation orbit targeted by this mission scenario is defined as:

$$a_t \delta \boldsymbol{\alpha}_{qns,f} = \begin{bmatrix} \delta a_f \\ a_t \delta \lambda_f \\ a_t \delta e_{x,f} \\ a_t \delta e_{y,f} \\ a_t \delta i_{x,f} \\ a_t \delta i_{y,f} \end{bmatrix} = \begin{bmatrix} 0 \\ 0 \\ 0 \\ 25 \\ 0 \\ 25 \end{bmatrix} \quad [\text{m}] \quad (5.19)$$

Starting from a position along the target's orbit, the goal of the mission is to reach the final separation orbit. In this case, no guidance reference profile is employed to track the path from the initial to the final state; full authority is left to the feedback controller. Therefore, the information on the final state is directly communicated to the controller, which computes the control action based on the error between the final and current states.

The target vehicle is considered to be on an eccentric orbit and aligned with its LVLH orbital frame. The angular velocity varies periodically with the true anomaly due to the orbit's eccentricity and is obtained from Eqs. (5.2) and (5.4).

The chaser's relative initial state is defined in terms of relative orbital elements. The initial position lies along the target's orbit:

$$a_t \delta \boldsymbol{\alpha}_{qns,0} = \begin{bmatrix} \delta a_0 \\ a_t \delta \lambda_0 \\ a_t \delta e_{x,0} \\ a_t \delta e_{y,0} \\ a_t \delta i_{x,0} \\ a_t \delta i_{y,0} \end{bmatrix} = \begin{bmatrix} 0 \\ 20 \\ 0 \\ 0 \\ 0 \\ 0 \end{bmatrix} \quad [\text{m}] \quad (5.20)$$

The weight matrices used for tuning the control gains are selected as described in Section 5.4.

6 | Results

This chapter presents the results obtained from the simulations outlined in Chapter 5. The outcomes of the experiments are organized into the following categories:

- Control gain tuning with the target in a circular orbit;
- Rendezvous and docking (RV&D) using impulsive guidance;
- Rendezvous and docking (RV&D) using continuous guidance;
- Formation flying using an eccentricity/inclination separation orbit.

6.1. Test 1: Control Gain Tuning with the Target in a Circular Orbit

Cartesian-Based Controller

As explained in Section 4.2, the Cartesian-based controller is analyzed using two different techniques. The first approach involves the numerical integration of the Differential Riccati Equation (DRE) using MATLAB’s `ode15s` solver. The second approach computes the infinite-horizon solution through the Algebraic Riccati Equation (ARE).

The results of the DRE numerical integration are shown in Figure 6.1. The figure displays all 18 components of the control gain matrix, each plotted over the integration time, represented as the number of orbits. Each row corresponds to the control gains influencing the transverse, out-of-plane, and radial components of the control input, respectively. The integration is carried out over the duration of three orbits.

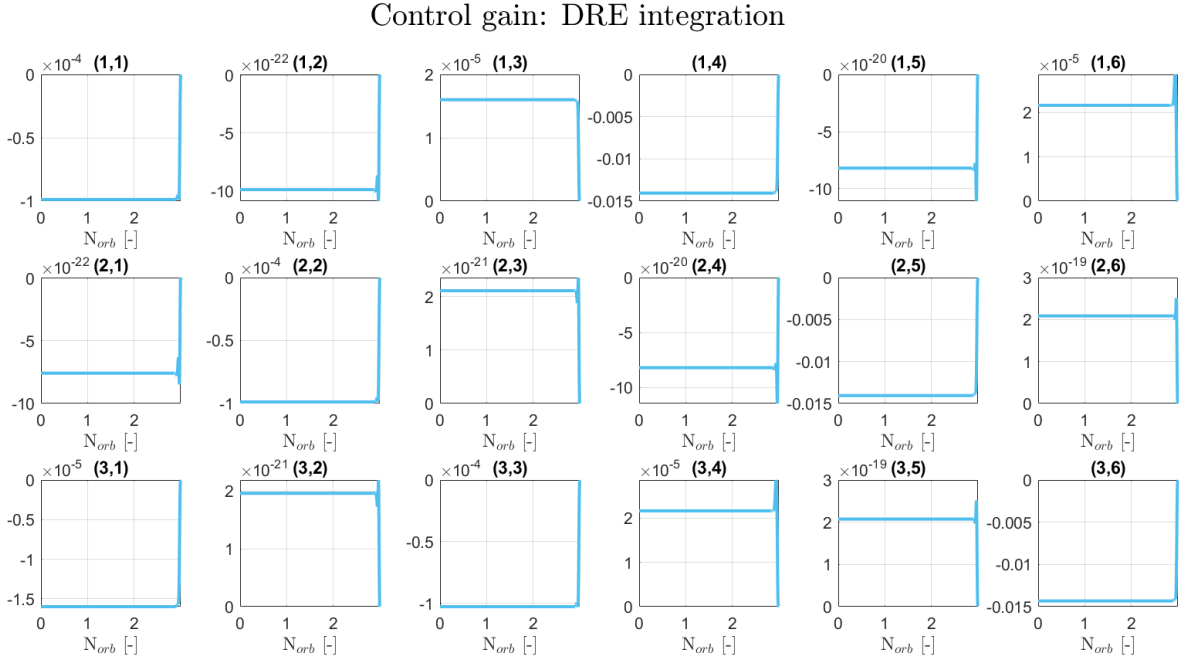


Figure 6.1: Control gain: DRE integration

Due to the backward nature of the integration in time, the gain components exhibit a transient behavior near the final time. As expected from the linear time-invariant (LTI) system describing the Cartesian-based circular dynamics, the gain matrix converges to a steady-state profile as it approaches the initial time. It is evident that the in-plane and out-of-plane components of the state and control inputs are decoupled through these gains. For clarification, the rows of the gain matrix correspond to the transverse, out-of-plane, and radial components of the control input, while the columns correspond to the same components of the position in the first three columns and of the velocity in the last three.

The steady-state gains are presented in Table 6.1, alongside the solution obtained via the ARE for comparison.

Control Gains: LQR Solution					
9.871330e-05	3.1710e-21	-1.6002e-05	0.0140547	1.1538e-18	-2.1619e-05
6.9893e-21	9.8737e-05	2.3030e-20	1.1539e-18	0.0140529	3.2885e-18
1.5990e-05	1.0165e-20	1.0260e-04	-2.1619e-05	3.2897e-18	0.0143216

Table 6.1: Control gain matrix: DRE integration (steady state) and ARE solution

The results from both methods agree up to at least the 16th decimal digit, validating the use of the ARE solution for computing steady-state gains.

ROE-Based Controller

The ROE-based dynamics are modeled as a linear time-varying (LTV) system. Consequently, the control gains are computed via numerical integration of the DRE using `ode15s`. The results of the backward-time integration are shown in Figure 6.2. In this context, the rows of the gain matrix correspond to the transverse, out-of-plane, and radial components of the control input, while the columns represent the six qns-ROE defined in Eq.(2.37), each scaled by the target semi-major axis. As expected, following a transient phase near the final time, the gains converge to a periodic steady state, exhibiting consistent time evolution over each orbital period.

Since the in-plane and out-of-plane dynamics are decoupled, the tangential and radial control inputs are not influenced by the qns-ROE components associated with variations in RAAN and inclination. Conversely, these components are the sole contributors to the out-of-plane control input. The steady-state control gains are shown in Figure 6.3 as a function of the true argument of latitude θ , which corresponds to the mean argument of latitude μ in the case of a near-circular orbit.

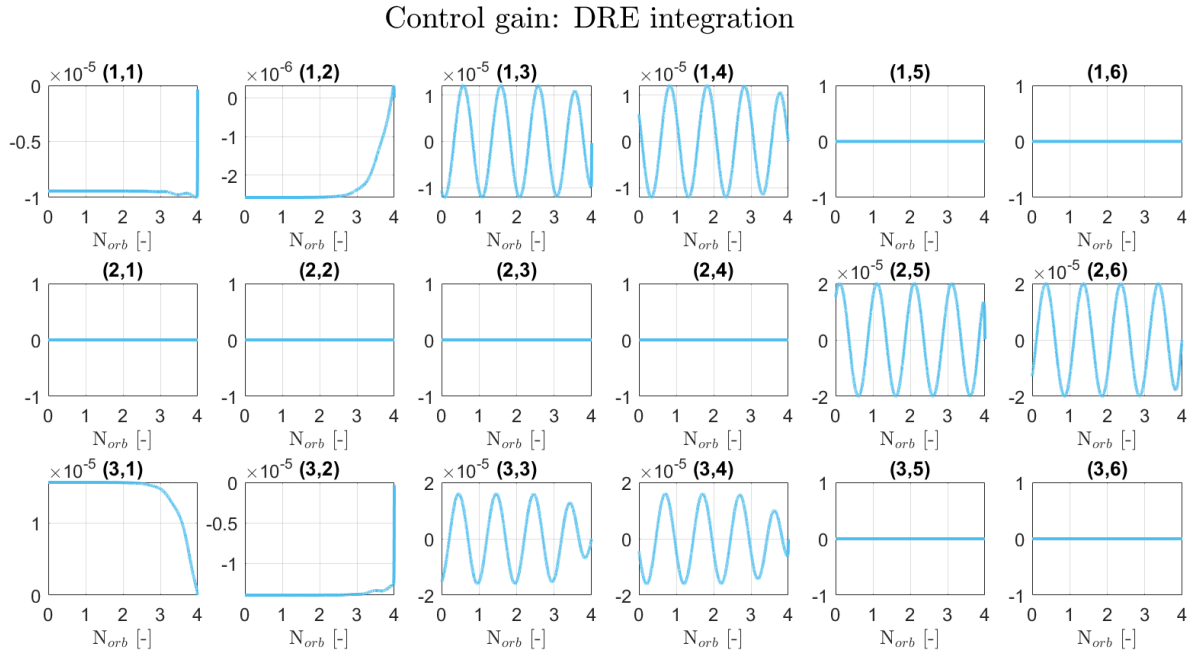


Figure 6.2: Control gains: DRE integration

Control gain: DRE integration (steady state)

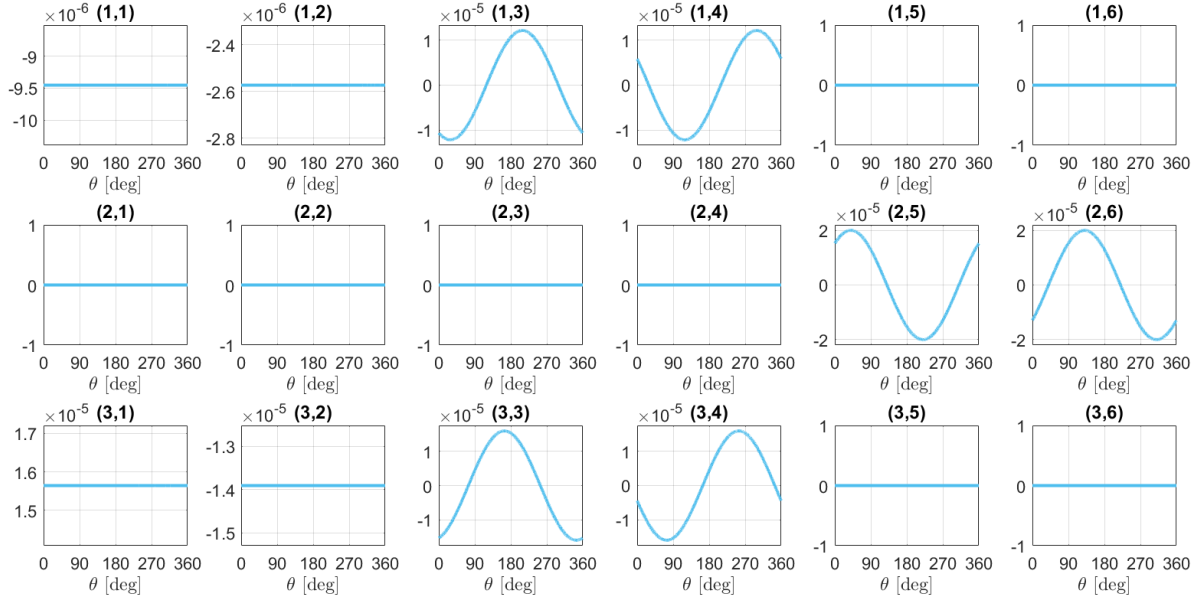


Figure 6.3: Control gains: DRE integration (steady state)

Attitude Controller

As with the translational Cartesian-based dynamics, the equations of motion for the attitude dynamics are described by a linear time-varying (LTV) system, which simplifies to a linear time-invariant (LTI) system in the case of near-circular orbits of the target vehicle. In the current experiment, this condition is satisfied, and thus the backward integration of the Riccati equation, shown in Figure 6.4, converges to constant steady-state values. These steady-state values, reported in Table 6.2, correspond both to the steady-state solution of the Differential Riccati Equation (DRE) integration and to the result obtained by solving the Algebraic Riccati Equation (ARE).

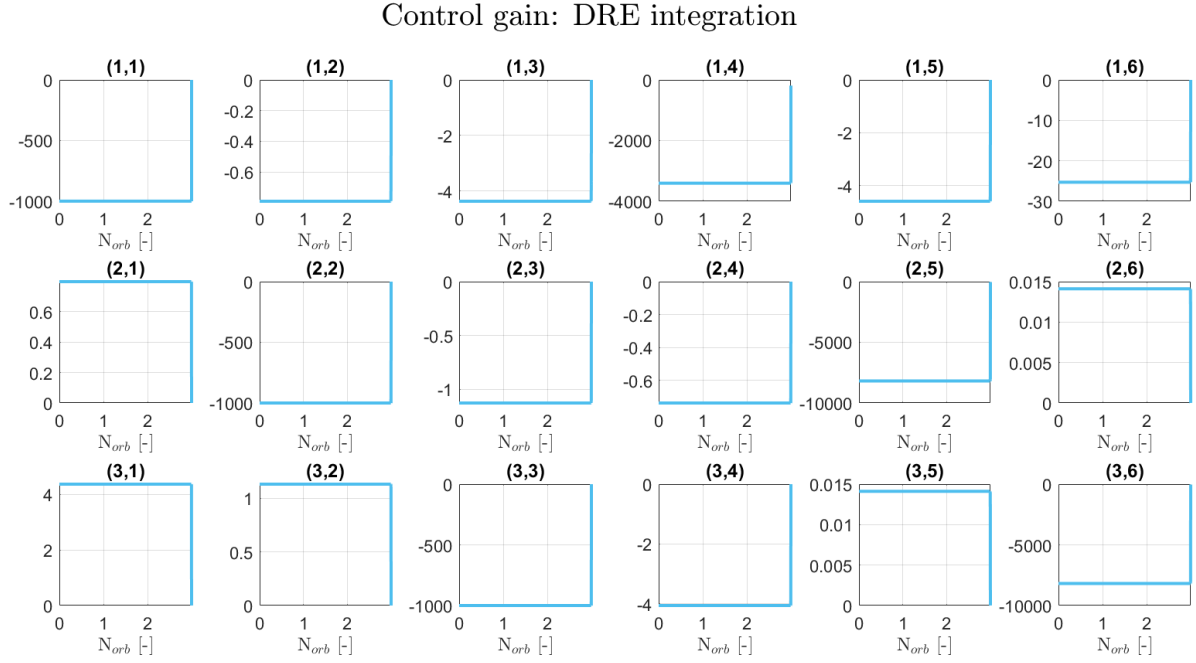


Figure 6.4: Control gain: DRE integration

Control Gains: LQR Solution					
999.99016	0.79084	4.36313	3405.89561	4.59281	25.28530
-0.79577	999.99946	1.12829	0.73763	8185.34762	-0.01411
-4.36223	-1.13175	999.98984	4.060972	-0.01411	8185.27279

Table 6.2: Control gain: DRE integration (steady state) and ARE solution

6.2. Test 2: RV&D using Impulsive Guidance

Guidance Profile

The guidance trajectory is described through its spatial components in Figure 6.5 and time evolution in Figure 6.6. The $\Delta\mathbf{V}$ table containing all impulsive manoeuvres required by the reference profile is reported in Appendix B. An overview of the manoeuvres is displayed in Table 6.3. The $\Delta\mathbf{V}$ values are expressed in the reference frame aligned with the docking axis (Line-of-sight).

Component (Line-of-sight)	Maximum Value	Time [s]	Minimum Value	Time [s]
ΔV_x	0.01041	44.0	-0.00414	1711.2
ΔV_y	0.00110	1051.0	-0.00070	44.0
ΔV_z	0.01074	836.7	0.00227	0.0

Total number of pulses: 41

Duration of the manoeuvre: 29.25 [min]

Table 6.3: Overview of the impulsive manoeuvres

The impulsive manoeuvre is constructed as a series of hops, as shown in Figure 4.1. However, due to the high number of nodes selected for the path construction, it resembles a straight-line trajectory with a trapezoidal velocity profile in the along-track direction. Consequently, the position components exhibit a parabolic–straight–parabolic profile, while the velocity components show an overall trapezoidal trend. On top of this, small zig-zag fluctuations appear due to the impulses applied at each node.

The initial and final states are defined in Eqs. (5.15) and (5.6). Since the initial point is defined with a drift with respect to the target LVLH frame, both in-plane and out-of-plane, all LVLH coordinates contribute to the chaser’s motion, with less workload on the out-of-plane axis due to the shorter initial distance from the docking point.

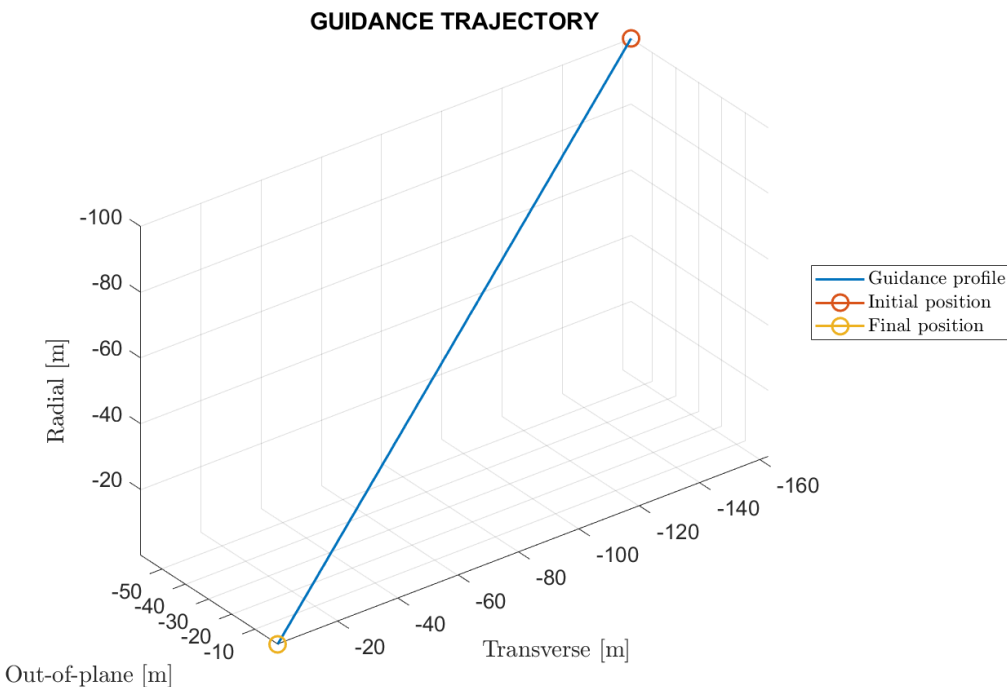


Figure 6.5: Guidance trajectory (LVLH frame)

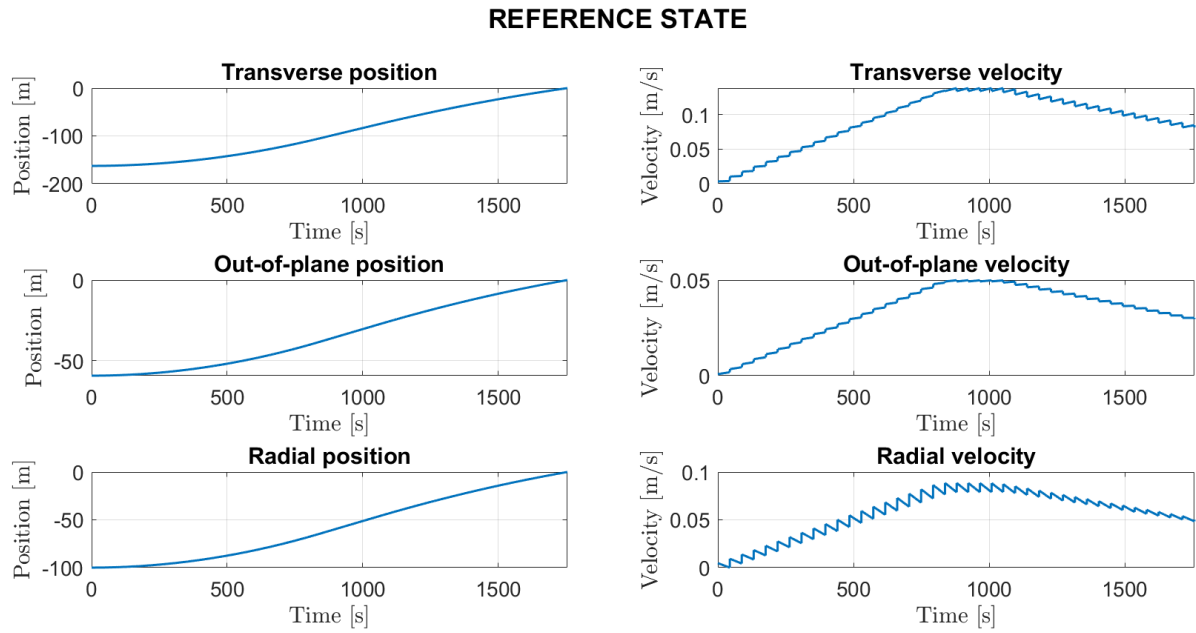


Figure 6.6: Time evolution of the reference state (LVLH frame)

The reference profile can also be viewed from a ROE (Relative Orbital Elements) perspective. This is obtained by transforming the propagated state in Figure 6.6 using the transformation described in Eq. (2.61). The resulting qns-ROE trajectory will be used for validating the ROE-based controller.

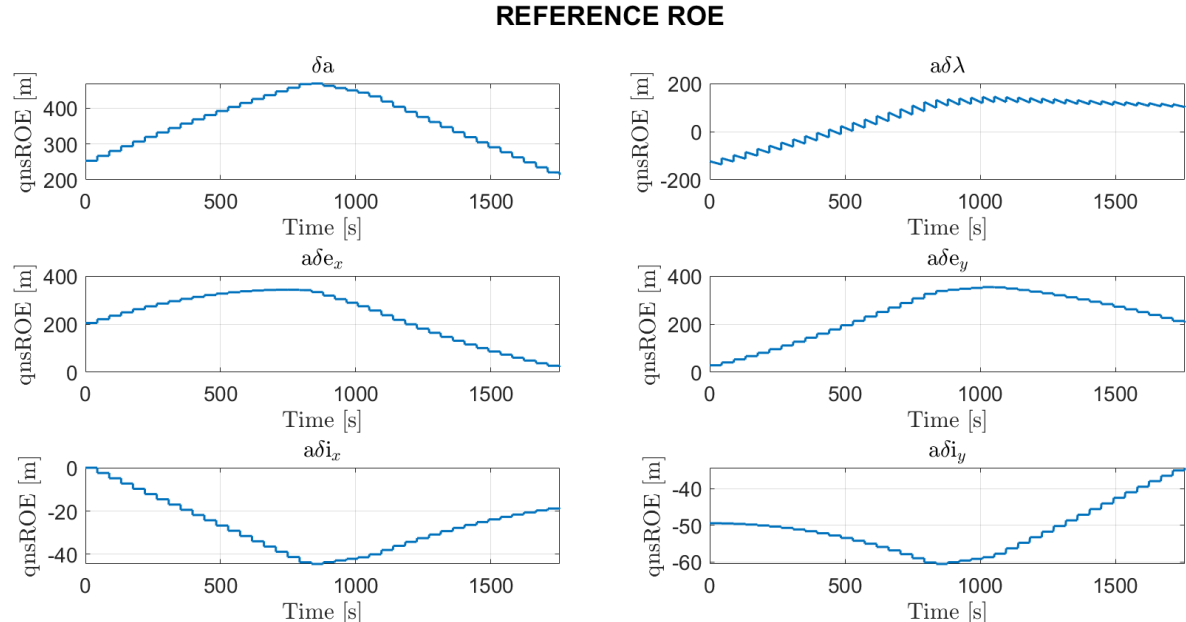


Figure 6.7: Time evolution of the reference qns-ROEs

Control Gains: Cartesian-Based dynamics

As explained in Section 4.2, the Cartesian-based controller is analyzed via two methods:
 (i) numerical integration of the Differential Riccati Equation (DRE) using `ode15s`, and
 (ii) solution of the infinite-horizon Algebraic Riccati Equation (ARE).

The results of the DRE integration are shown in Figure 6.8. The plot contains the 18 elements of the control gain matrix, with each element tracked over time (expressed in orbits). Each row corresponds to the gains influencing the tangential, out-of-plane, and radial control components. The integration spans three orbital periods.

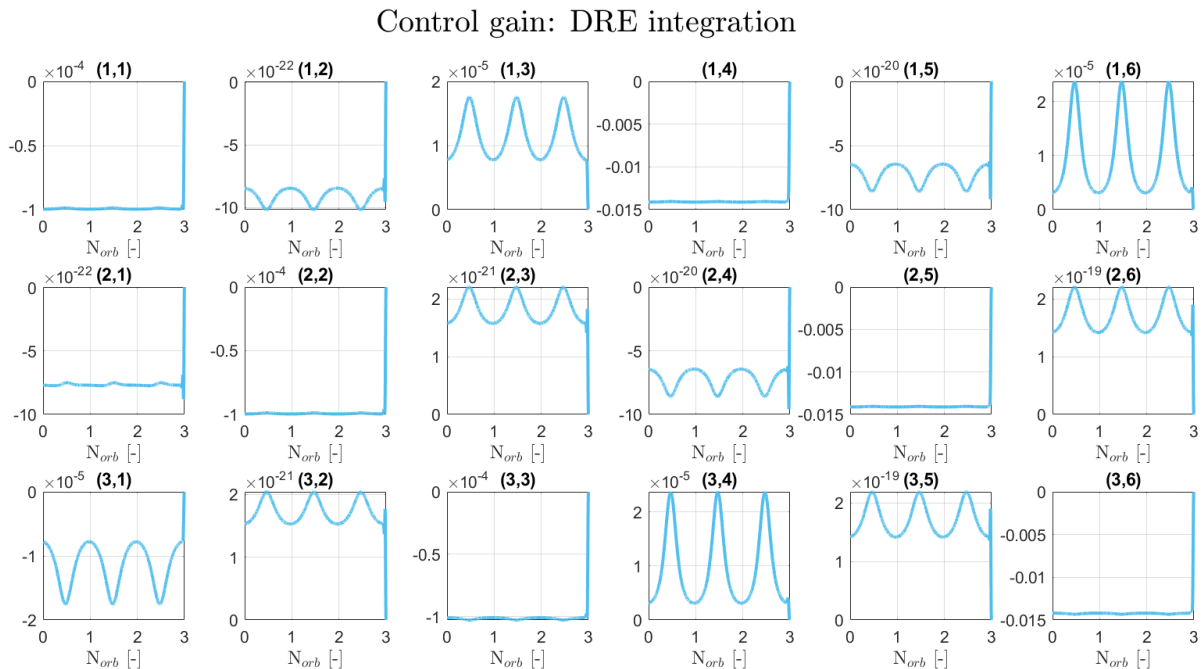


Figure 6.8: Control gain: DRE integration

Due to the backward integration, a transient behavior appears near the final time. As expected from the periodic LTV system describing the eccentric dynamics, the solution converges to a periodic steady state, with values repeating each orbit during the backward integration. These steady-state gains are compared with the ARE solution in Figure 6.9.

Control gain: DRE integration vs Infinite horizon

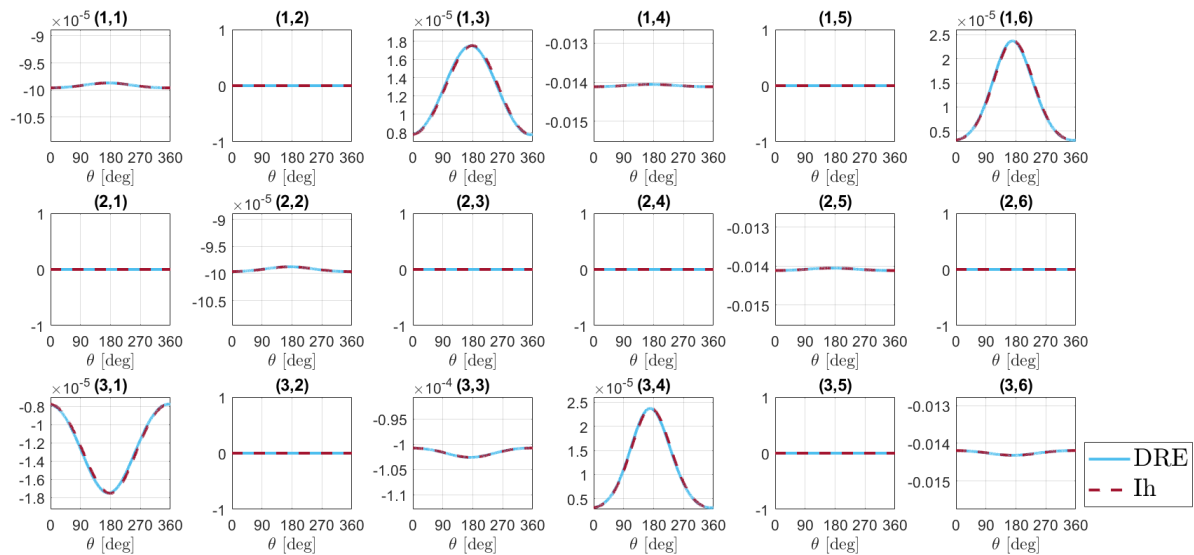


Figure 6.9: Control gain: DRE integration (steady state) vs Infinite horizon

The two methods produce comparable results, exhibiting the same shape and order of magnitude. As observed in the circular case, the gains linking the out-of-plane states to the in-plane components of the controller are zero, and vice versa.

Control Gains: ROE-based dynamics

The ROE-based dynamics form an LTV system. Control gains are computed by backward integration of the DRE using `ode15s`. As shown in Figure 6.10, a transient occurs near the final time, followed by a periodic steady-state profile repeating each orbital period.

By analysing Eq. (2.54), we observe that, unlike the circular case, the equations of motion for the third and fourth qns-ROE components (e_x and e_y) are influenced by the out-of-plane control input through the input matrix \mathbf{B} . This results in control gains exhibiting non-zero values in components that were previously zero in the circular dynamics control gains (see Figure 6.3). The steady-state control gains are presented in Figure 6.11 as functions of the true argument of latitude θ .

Control gain: DRE integration

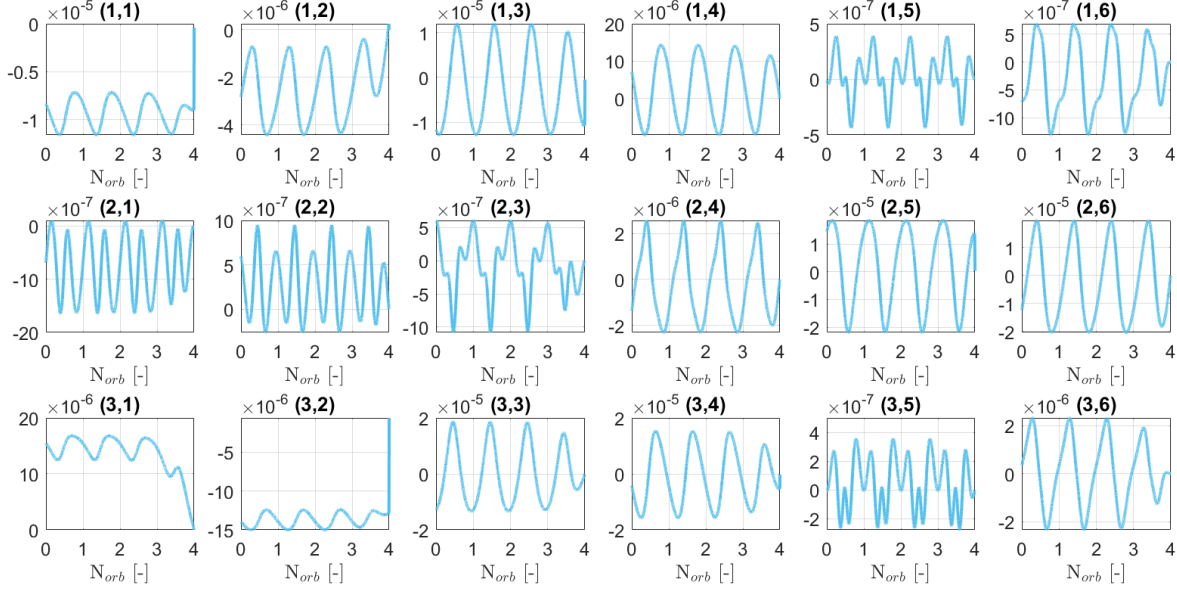


Figure 6.10: Control gains: DRE integration

Control gain: DRE integration (steady state)

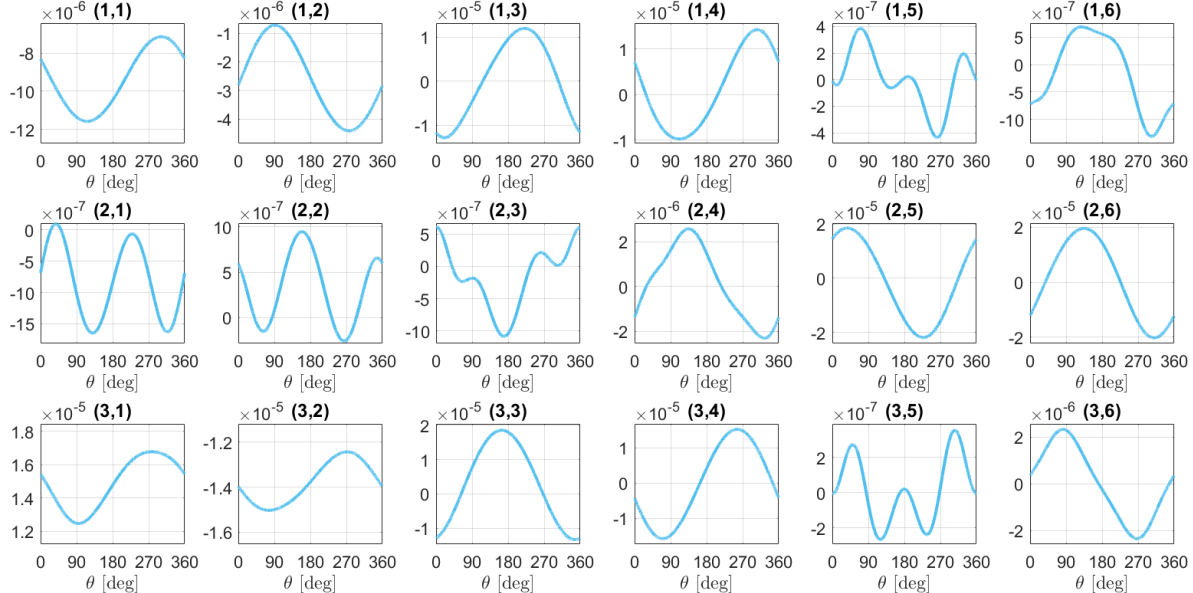


Figure 6.11: Control gains: DRE integration (steady state)

Control Gains: Attitude dynamics

Since the eccentric dynamics are described by a periodic LTV system, the gains converge to a periodic steady state that repeats every orbit. The integration of the differential

Riccati equation (DRE) is shown in Figure 6.12, and the steady-state gains are reported in Figure 6.13, compared against the results obtained from the algebraic Riccati equation (ARE).

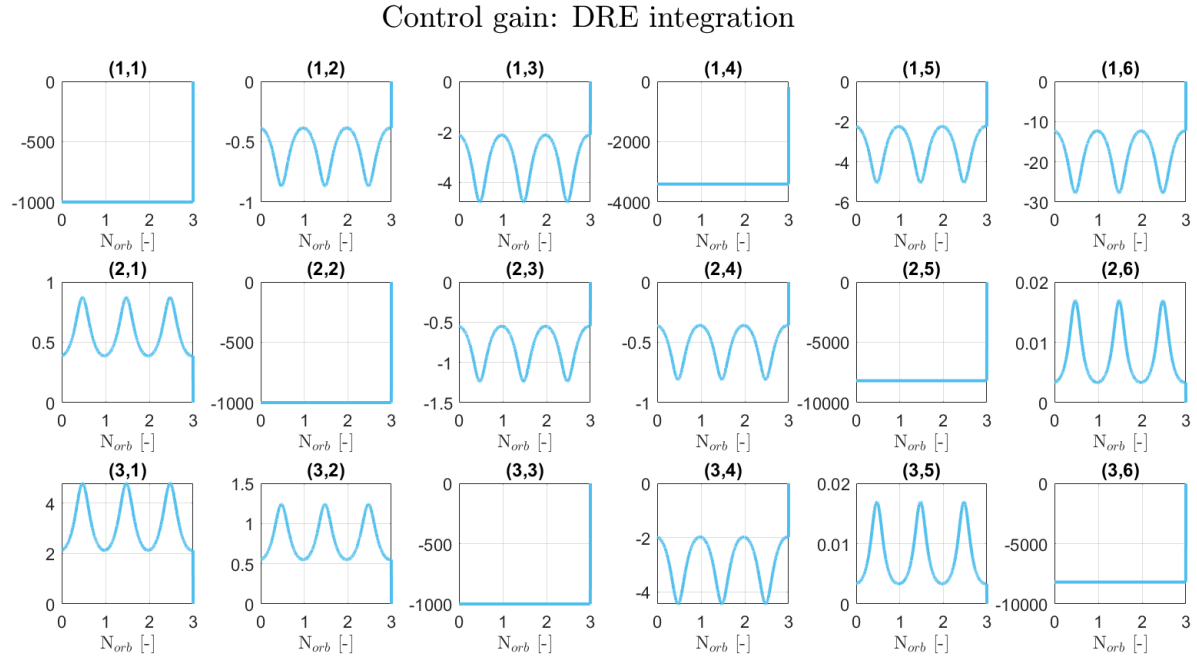


Figure 6.12: Control gain: DRE integration

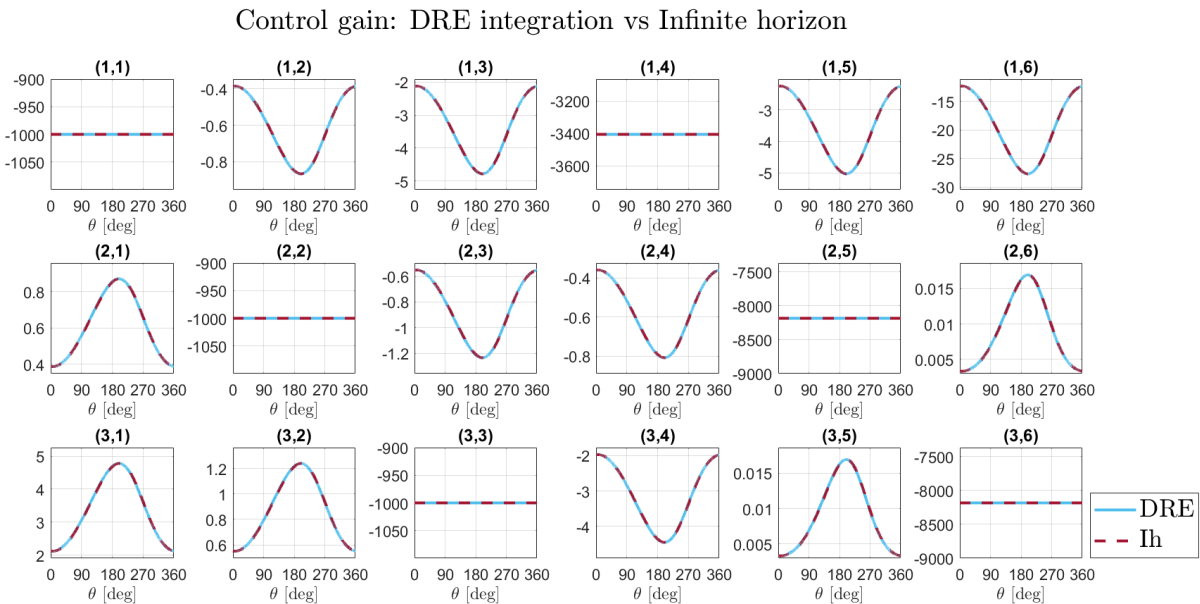


Figure 6.13: Control gain: DRE integration (steady state) vs Infinite horizon

Simulation Results: Cartesian-based Controller

This section presents the results of the simulation conducted using the Cartesian-based formulation of the controller. The trajectory and component-wise time evolution of the controlled state are shown in Figure 6.14, closely following the guidance in Section 6.2. The control error is presented in Figure 6.15.

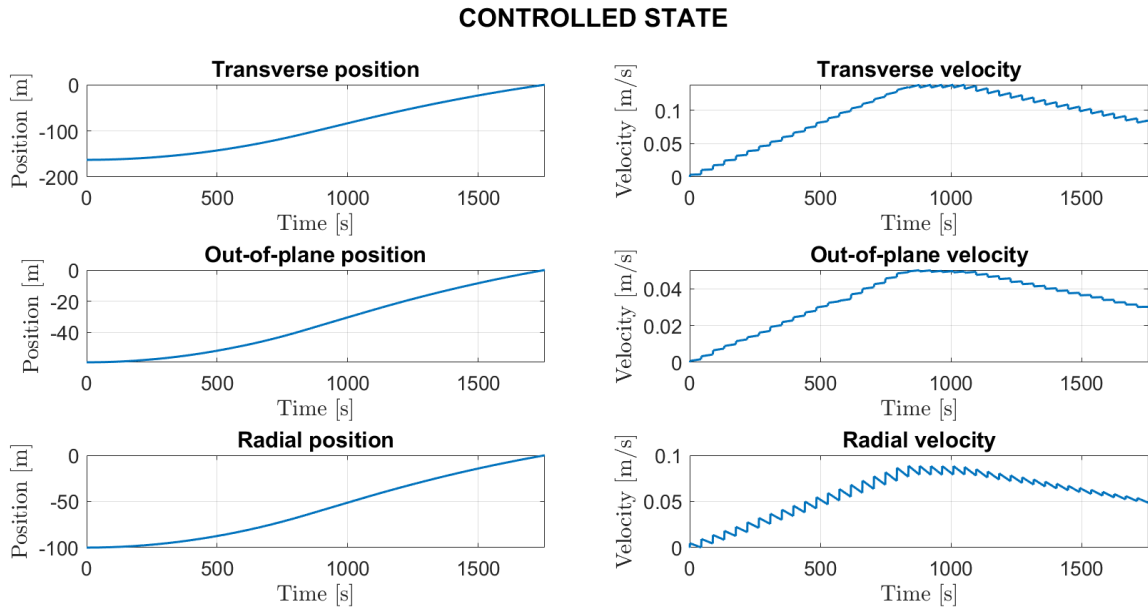


Figure 6.14: Time evolution of the controlled profile (LVLH frame)

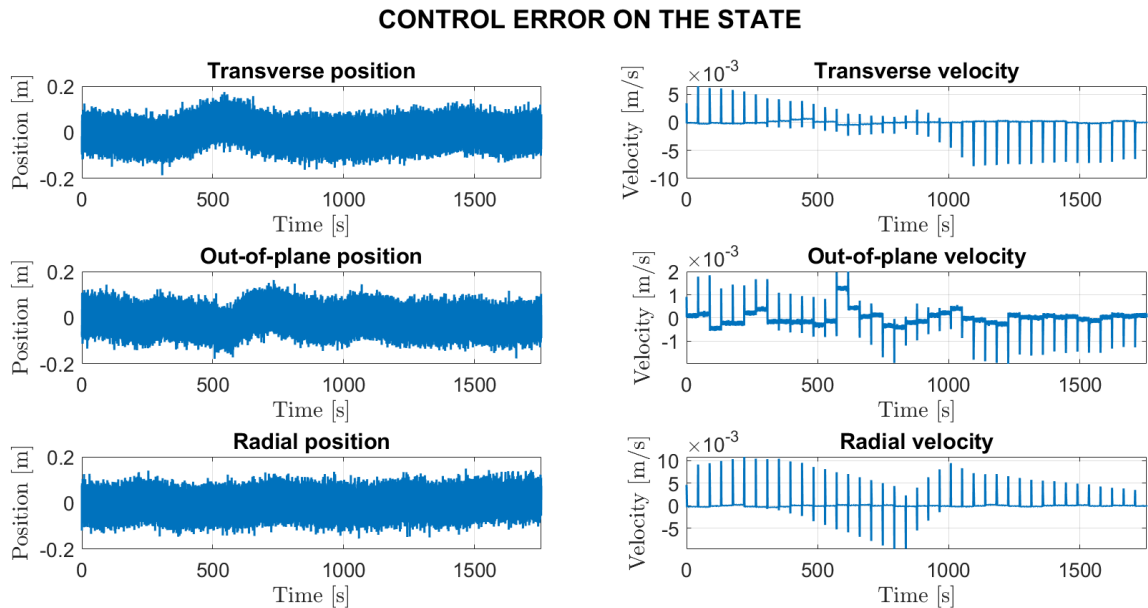


Figure 6.15: Control error on the state (LVLH frame)

All position errors remain within a few centimeters, indicating excellent controller performance. Velocity errors behave similarly well; however, instantaneous errors occur during pulse applications, due to the conversion of impulsive $\Delta\mathbf{V}$ into discrete control inputs as explained in Section 4.2. These are quickly corrected by the controller.

Figure 6.16 shows the ideal thrust directly computed by the controller. As expected, thrust peaks occur at time instants consistent with the planned $\Delta\mathbf{V}$ impulses. The required thrust remains within the operational limits of the thrusters (Table 5.6), confirming the effectiveness of both the guidance design and the control input minimization strategy. The thrust actions are expressed in the chaser's body frame axes.

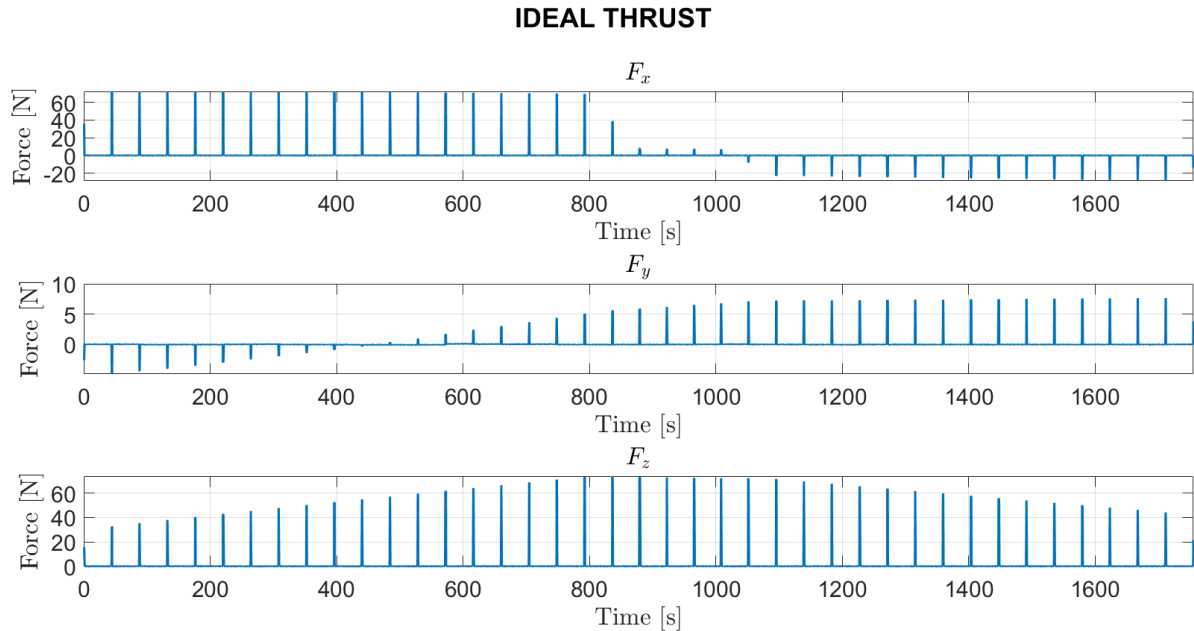


Figure 6.16: Ideal thrust (body frame)

Figure 6.17 shows the actual thrust commands generated by the pulse-width modulation (PWM) logic, as described in Section 3.2.3. Only a single thrust level is available, consistent with the specifications of the selected thrusters (Table 5.6). When the ideal thrust falls below the Minimum Impulse Bit (MIB) threshold, no pulse is triggered, and the corresponding impulse is accumulated and released in subsequent steps when the threshold is exceeded.

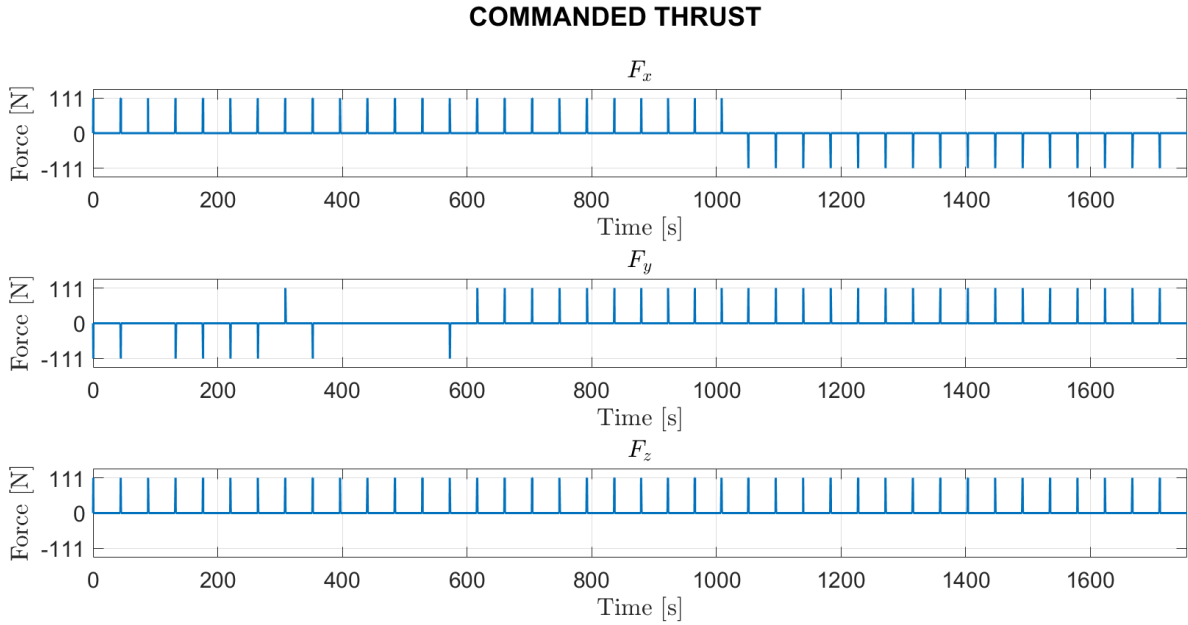


Figure 6.17: Commanded thrust (body frame)

An overview of the thruster activity is provided in Table 6.4, which reports the firing times for each of the six selected thrusters along with the total propellant consumption. The directions listed in the table refer to the chaser's body frame, with the majority of thrusting time concentrated in the $+x$ and $+z$ directions, aligned with the main axis of motion.

Direction	Firing Time [s]
$+x$	12.520
$+y$	1.730
$+z$	24.400
$-x$	3.630
$-y$	0.470
$-z$	0.080
Total propellant consumption	1.878 [kg]

Table 6.4: Thruster firing times and total propellant consumption

CONTROL ERROR ON THE ATTITUDE

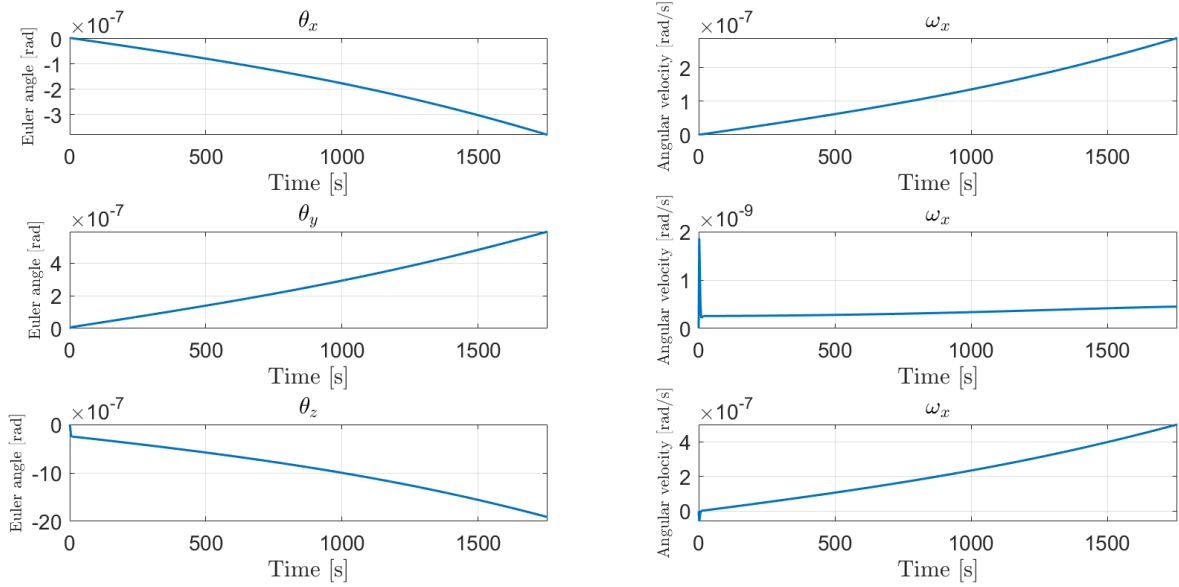


Figure 6.18: Control error on the attitude (body frame)

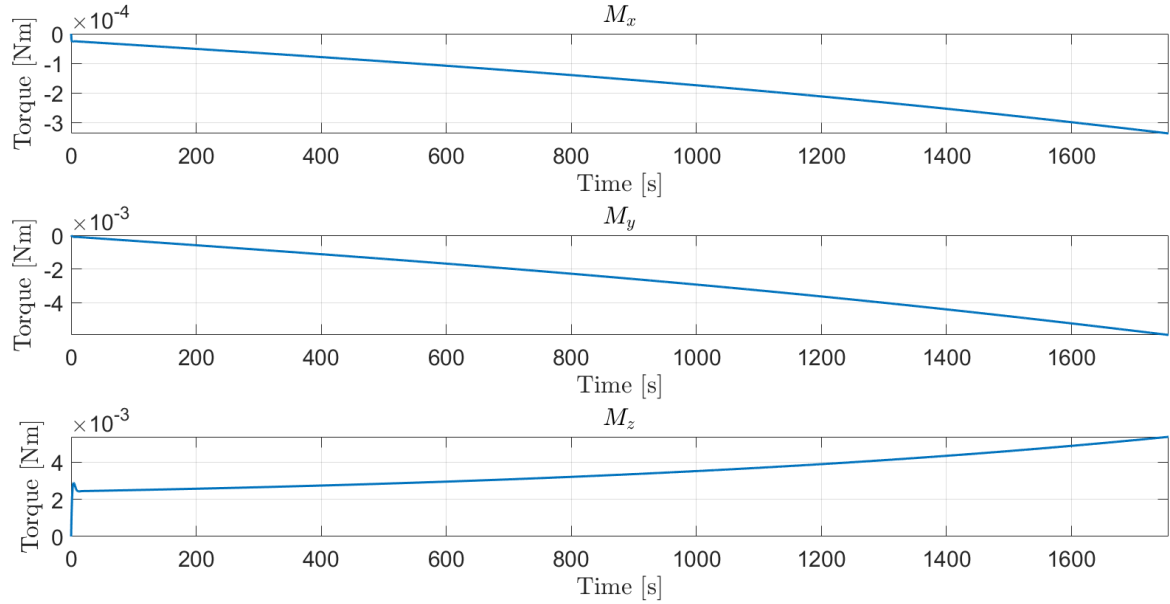


Figure 6.19: Control torque (body frame)

Figure 6.18 presents the control error on the attitude, as regulated by the attitude controller. The error exhibits a gradual increase over time, primarily due to the target vehicle transitioning from a region near apocentre, where orbital curvature is relatively low, to the pericentre, where curvature effects are more pronounced. This increased curvature makes

it more challenging to align the chaser's attitude with that of the target, particularly when they are located at significantly different true anomalies. Nevertheless, despite the local increase in error, the overall deviation remains within acceptable limits, ensuring that the chaser accurately tracks both the target's attitude and angular velocity with negligible error. Similarly, the control torque shown in Figure 6.19 experiences a greater demand as the vehicle progresses from the apocentre toward regions of higher orbital curvature. This reflects the increased control effort required to maintain precise attitude alignment under more dynamic orbital conditions.

Simulation Results: ROE-based Controller

This section presents the results of the simulation performed using the ROE-based formulation of the controller. The results are presented in the same format as those for the Cartesian-based formulation, with the exception of the attitude controller results, which are omitted here as they are identical to those previously discussed.

Figure 6.20 illustrates the time evolution of the controlled quasi-nonsingular relative orbital elements (qns-ROE). A comparison with the guidance reference shown in Figure 6.7 demonstrates that the feedback controller effectively tracks a trajectory that closely follows the time evolution of the reference qns-ROE. The control error associated with the ROE is reported in Figure 6.21, which shows that the error remains consistently small relative to the order of magnitude of the orbital elements. The local peaks in the error, occurring at the instants of thrust application, are due to the fact that the thrusters and the control algorithm cannot deliver truly impulsive actions. Nevertheless, the control error is quickly corrected after each thrust event, and the overall impulse delivered in the vicinity of the intended application time closely approximates that of an ideal instantaneous impulse.

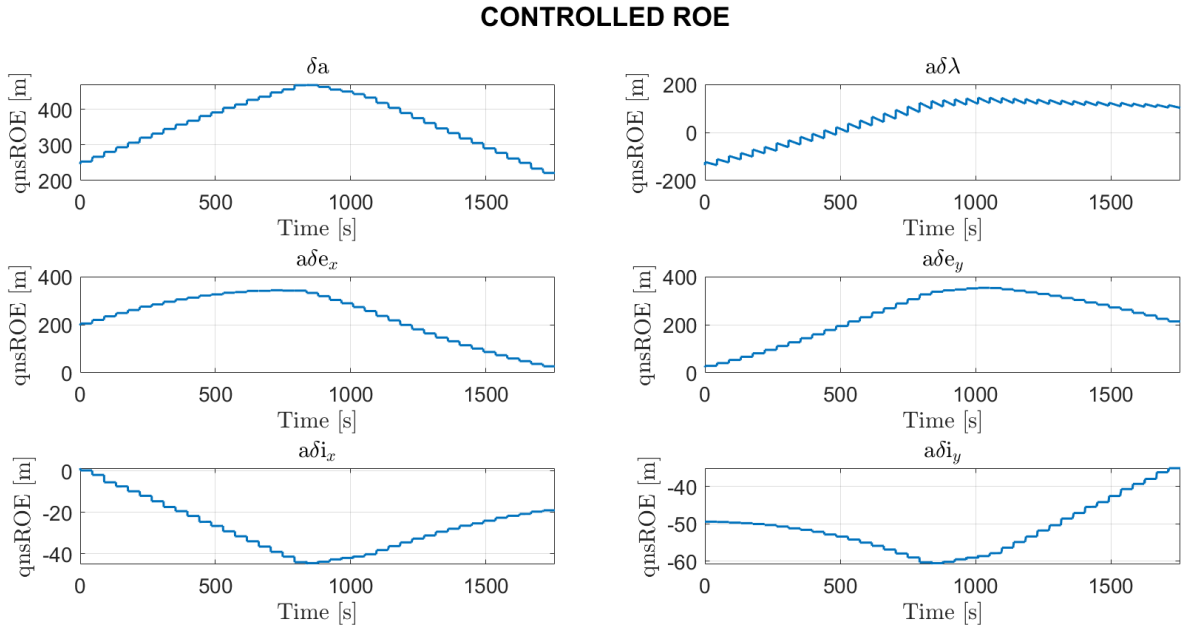


Figure 6.20: Time evolution of the controlled qns-ROE

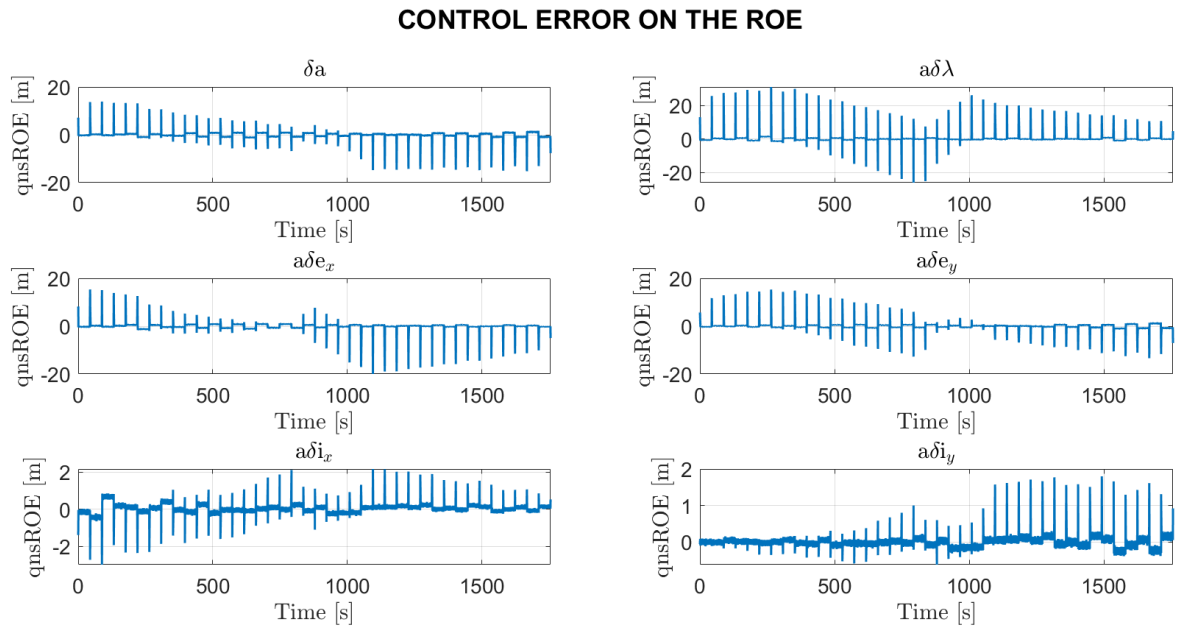


Figure 6.21: Control error on the qns-ROE

For a more comprehensive evaluation, the control error produced by the ROE-based controller is also expressed in terms of the Cartesian state, as shown in Figure 6.22. The resulting error remains within a few centimeters. When compared to the dimensions of the satellites used in the simulation, this error is small.

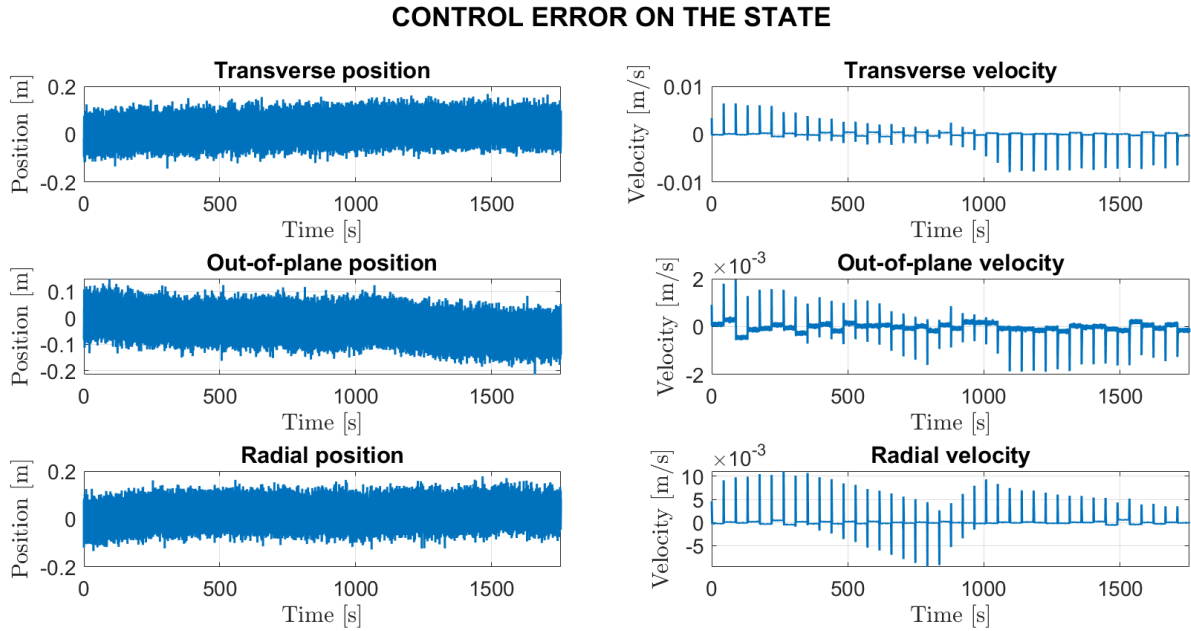


Figure 6.22: Control error on the Cartesian state (LVLH frame)

The commanded thrust is shown in Figure 6.23, where control inputs are applied in correspondence with the reference $\Delta\mathbf{V}$ events. The resulting thrust profile resembles the commanded actions observed when employing the Cartesian-based controller.

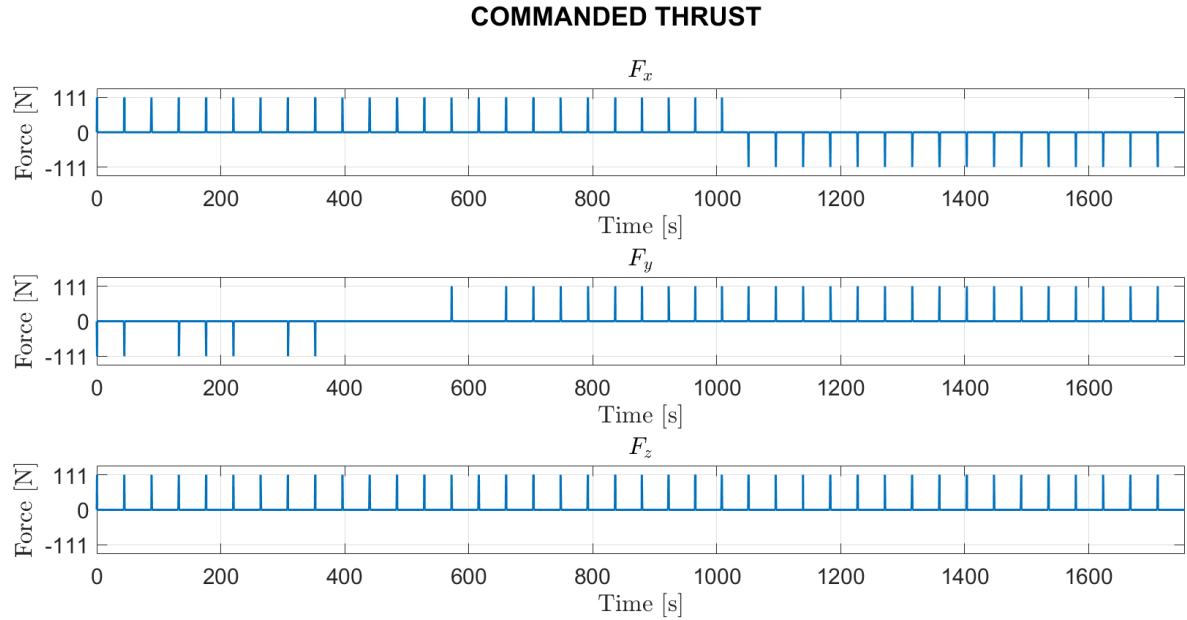


Figure 6.23: Commanded thrust (body frame)

An overview of the thruster firing times and the corresponding propellant consumption

is provided in Table 6.5, once again demonstrating results that are consistent with those obtained using the Cartesian-based control approach. A difference of 0.058 kg is observed, which comes from the relationship between the selected weighting matrices used in generating the control gains and the thruster management algorithm. This discrepancy does not indicate any performance difference between the Cartesian-based and ROE-based controllers.

Direction	Firing Time [s]
+x	13.010
+y	1.690
+z	20.560
-x	4.100
-y	0.420
-z	0.250
Total propellant consumption	1.936 [kg]

Table 6.5: Thruster firing times and total propellant consumption

6.3. Test 3: RV&D using Continuous Guidance

This section presents the guidance profile, control gains, and simulation results for the experiment conducted with continuous guidance. The results of the attitude controller are not shown, as they are expected to be as those obtained in the impulsive guidance experiment.

Guidance Profile

Figure 6.24 shows the reference accelerations in the rotated docking frame. As expected, the acceleration in the along-track direction follows the typical accelerating, coasting, decelerating profile, consisting of an initial phase of constant positive acceleration, a coasting phase with zero acceleration, and a final phase of constant negative acceleration. The accelerations in the cross-track directions serve to counteract gravitational perturbations and to support the motion in the along-track direction. The duration of the maneuver is shorter than that required for the impulsive guidance experiment:

$$T = 370.32 \quad [\text{s}] \quad (6.1)$$

This duration corresponds to 0.05% of the target's orbital period and is shorter than the typical final approach time between the ISS and Soyuz, which is approximately 11 minutes [44].

In this case, the difference in duration between the impulsive and continuous maneuvers arises from their underlying guidance strategies. The impulsive maneuver leverages the satellite's natural dynamics in combination with discrete thrust pulses to follow the desired trajectory, which inherently requires more time. In contrast, the continuous maneuver imposes a sustained forced motion, without relying on natural orbital dynamics, allowing it to reach the final point in a shorter time. This difference will lead to a variation in propellant consumption, as will be demonstrated later.

The guidance trajectory follows a straight-line path similar to that shown in Figure 6.5 for the impulsive guidance experiment. However, whereas in the impulsive case the straight-line motion was the result of a high number of discrete thrust pulses, in this case the straight-line path is explicitly generated by the continuous guidance strategy.

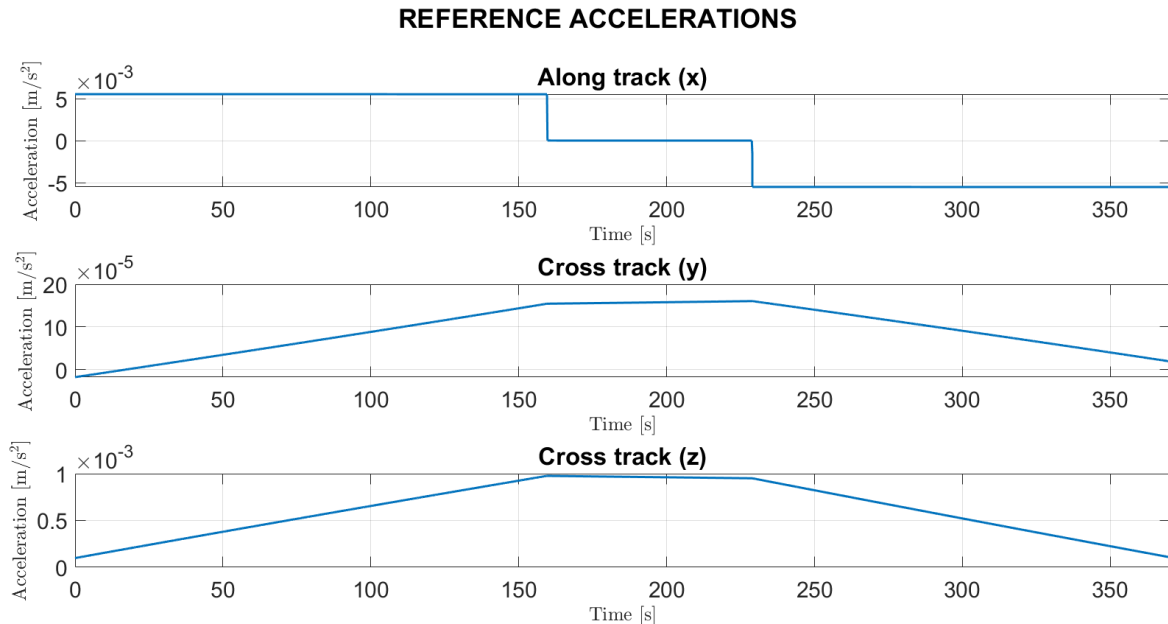


Figure 6.24: Reference acceleration (Rotated docking frame)

The time evolution of the reference state and qns-ROEs are shown in Figure 6.25 and Figure 6.26, respectively. The position profiles exhibit the expected behavior of an accelerating–coasting–decelerating motion: an initial exponential increase, followed by a linear segment, and a final exponential increase. The velocity profiles take the form of a

trapezoidal waveform, consistent with the applied acceleration profile.

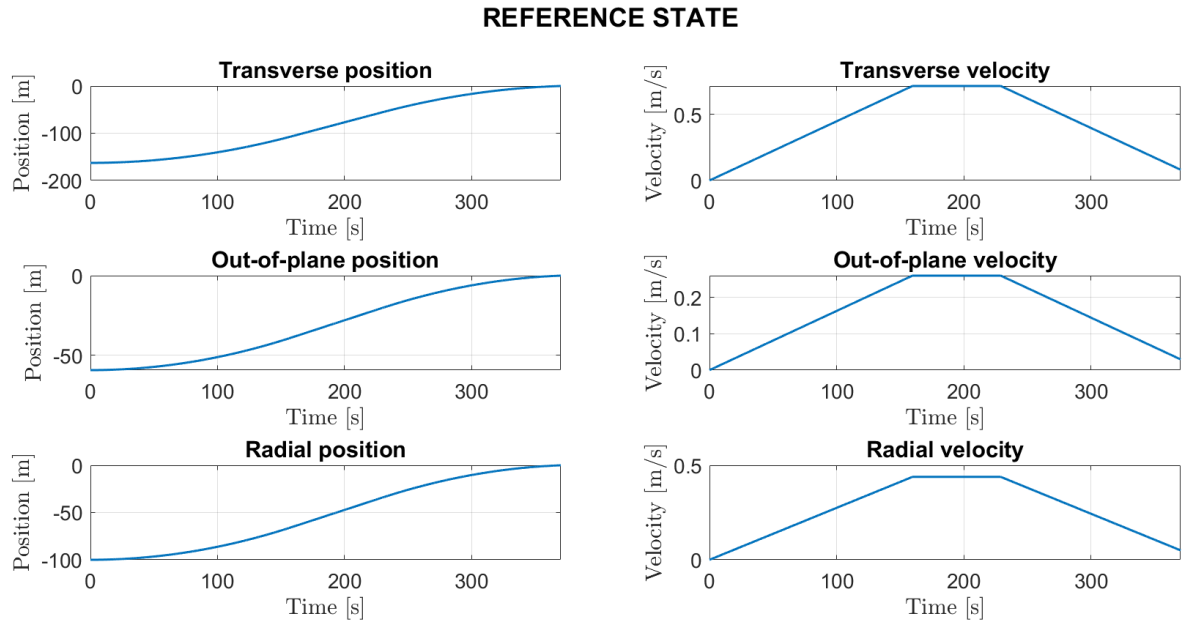


Figure 6.25: Time evolution of the reference state (LVLH frame)

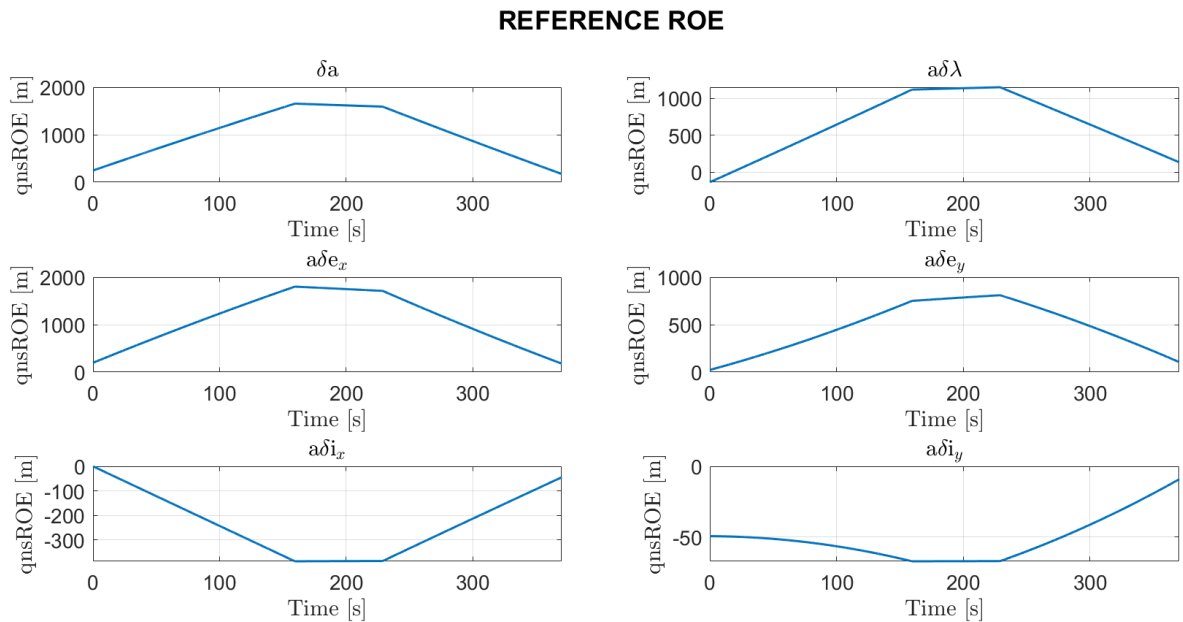


Figure 6.26: Time evolution of the reference qns-ROEs

Simulation Results: Cartesian-Based Controller

Both the position and velocity errors remain small when compared to the magnitude of the state variables themselves. These errors are similar to those observed in the impulsive guidance experiment, with the key difference being the absence of sharp peaks in the velocity error. In this case, the smoother guidance profile leads to better compatibility with the thruster dynamics, eliminating the transient peaks that occurred at thrust pulse events in the impulsive case.

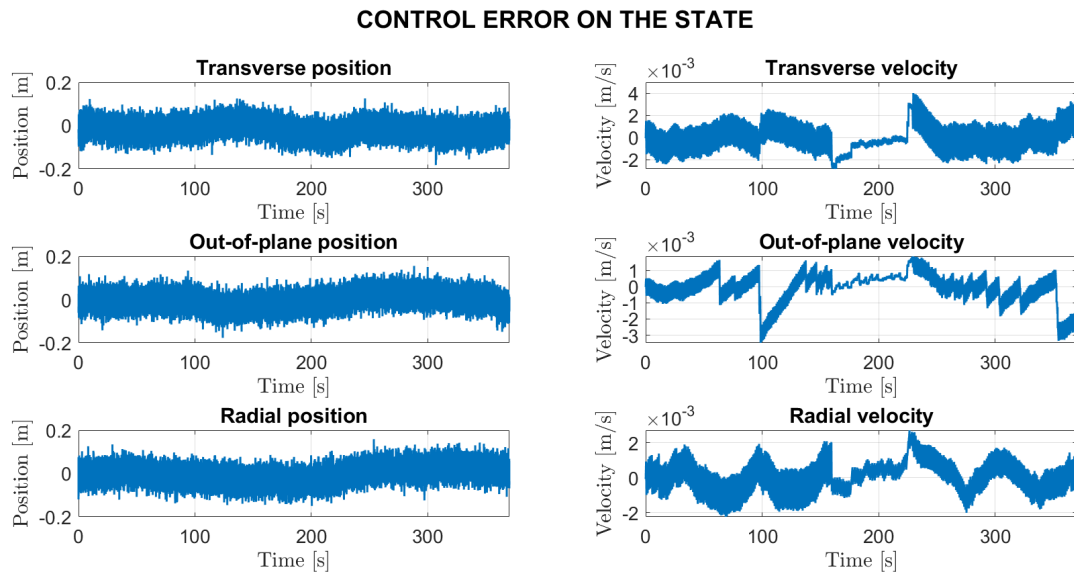


Figure 6.27: Control error on the state (LVLH frame)

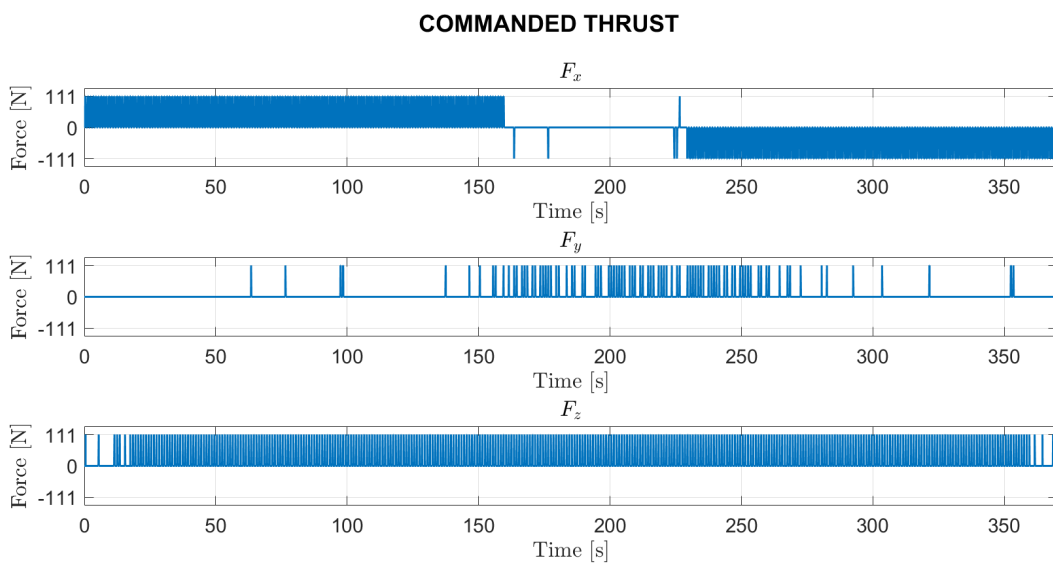


Figure 6.28: Commanded thrust (body frame)

The commanded thrust is consistent with the reference acceleration provided by the guidance block (see Figure 6.24). The table of thruster firing times and propellant consumption indicates a more intensive use of the thrusters in this scenario, with higher cumulative firing durations and increased propellant usage.

Direction	Firing Time [s]
$+x$	54.640
$+y$	2.290
$+z$	14.060
$-x$	47.970
$-y$	0.000
$-z$	0.000
Total propellant consumption	5.752 [kg]

Table 6.6: Thruster firing times and total propellant consumption

Simulation Results: ROE-based Controller

The performance of the ROE-based controller is evaluated in terms of the control error on the qns-ROEs (see Figure 6.29), the control error on the state (see Figure 6.30), and the commanded thrust (see Figure 6.31). The state error and the commanded thrust are comparable to those obtained with the Cartesian-based controller. The control errors on the qns-ROEs remain small relative to the magnitude of the orbital elements, indicating effective tracking performance.

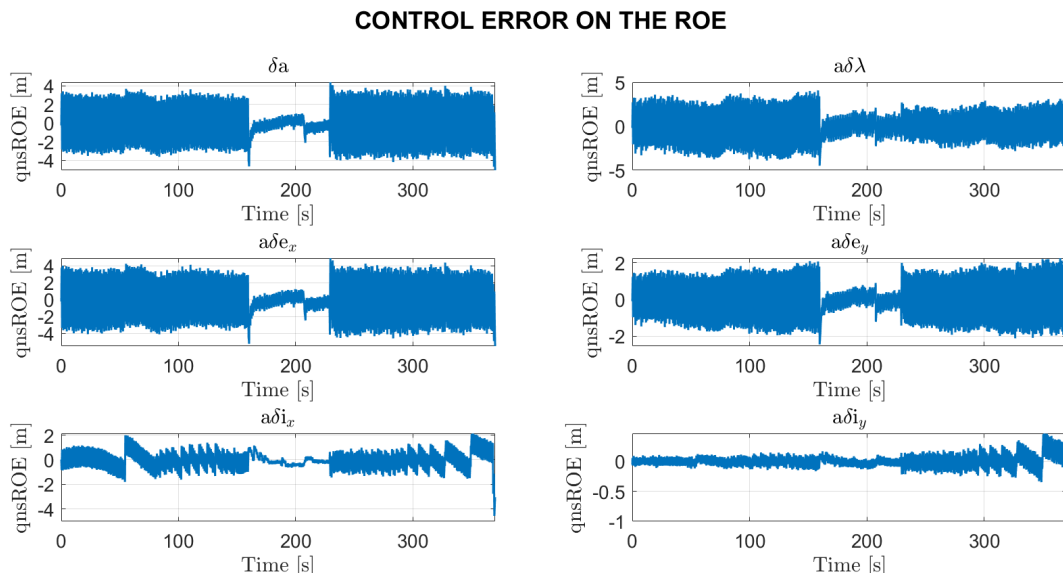


Figure 6.29: Control error on the qns-ROE

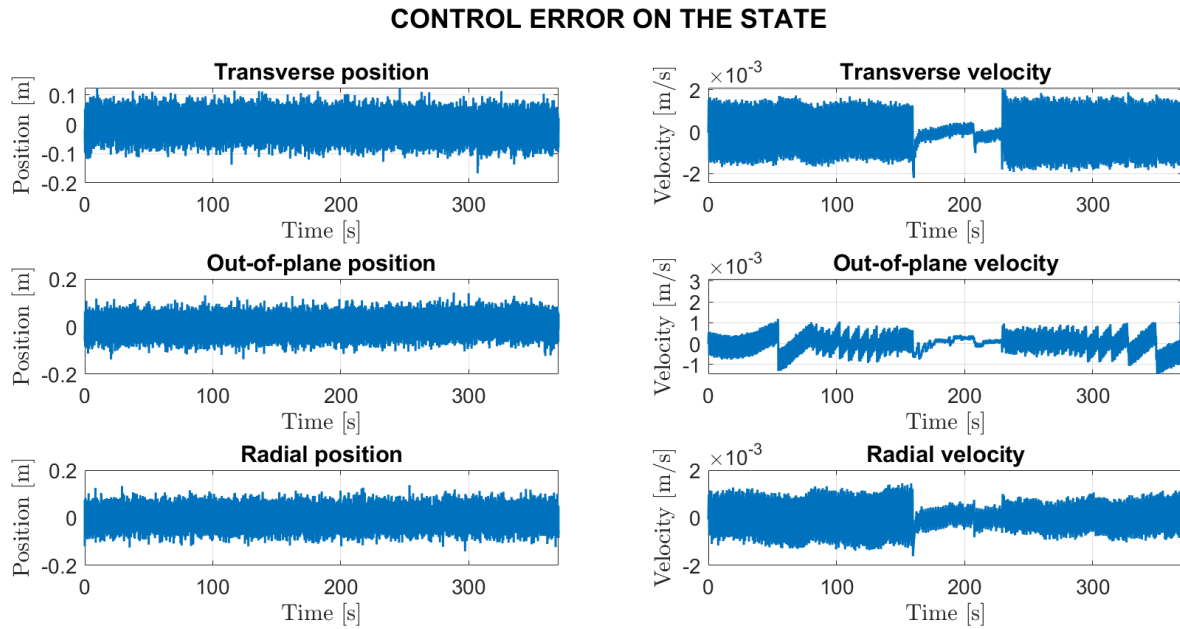


Figure 6.30: Control error on the state (LVLH frame)

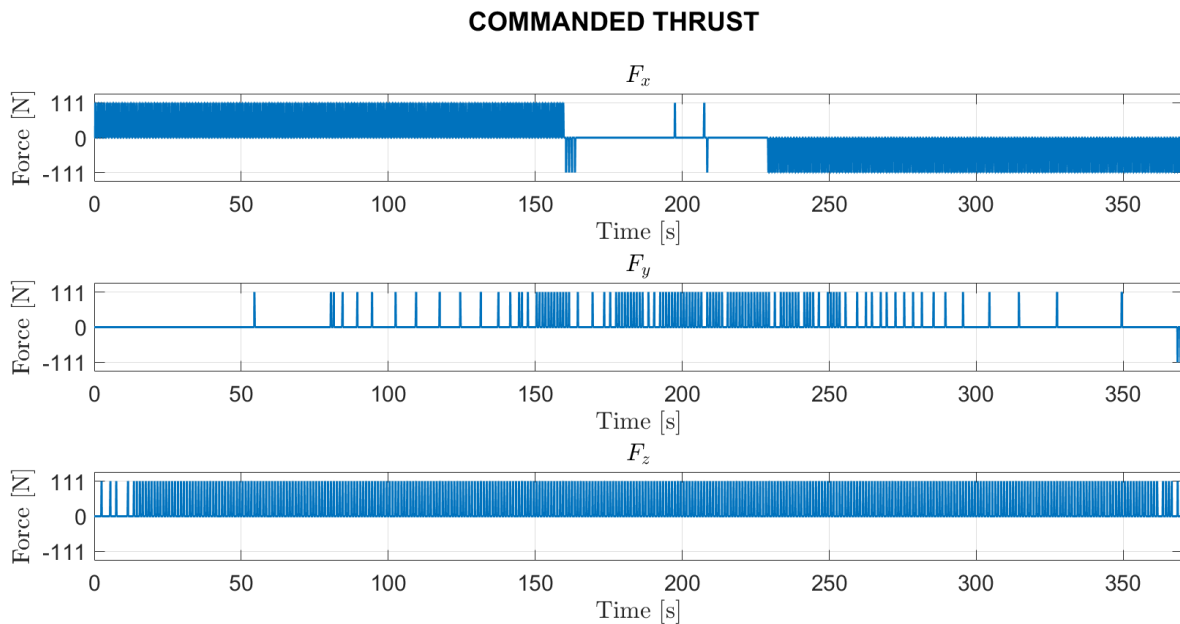


Figure 6.31: Commanded thrust (body frame)

Direction	Firing Time [s]
$+x$	54.700
$+y$	2.190
$+z$	14.040
$-x$	47.980
$-y$	0.230
$-z$	0.000
Total propellant consumption	5.761 [kg]

Table 6.7: Thruster firing times and total propellant consumption

6.4. Test 4: Formation Flying using e/i Separation Orbit

The results of the fourth test are presented in terms of the time evolution of the quasi-nonsingular Relative Orbital Elements (qns-ROE) and the corresponding control error relative to the final target configuration. The simulation is conducted over four orbital periods, during which the controller successfully generates a control force that guides the chaser to the desired formation flying configuration.

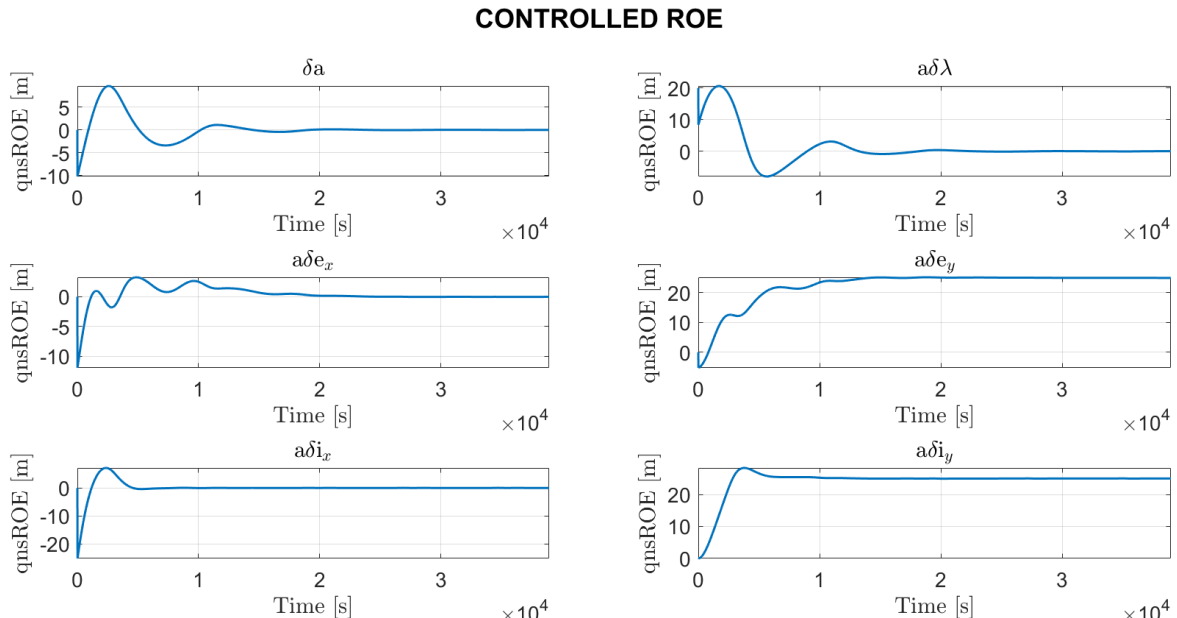


Figure 6.32: Time evolution of the controlled qns-ROE

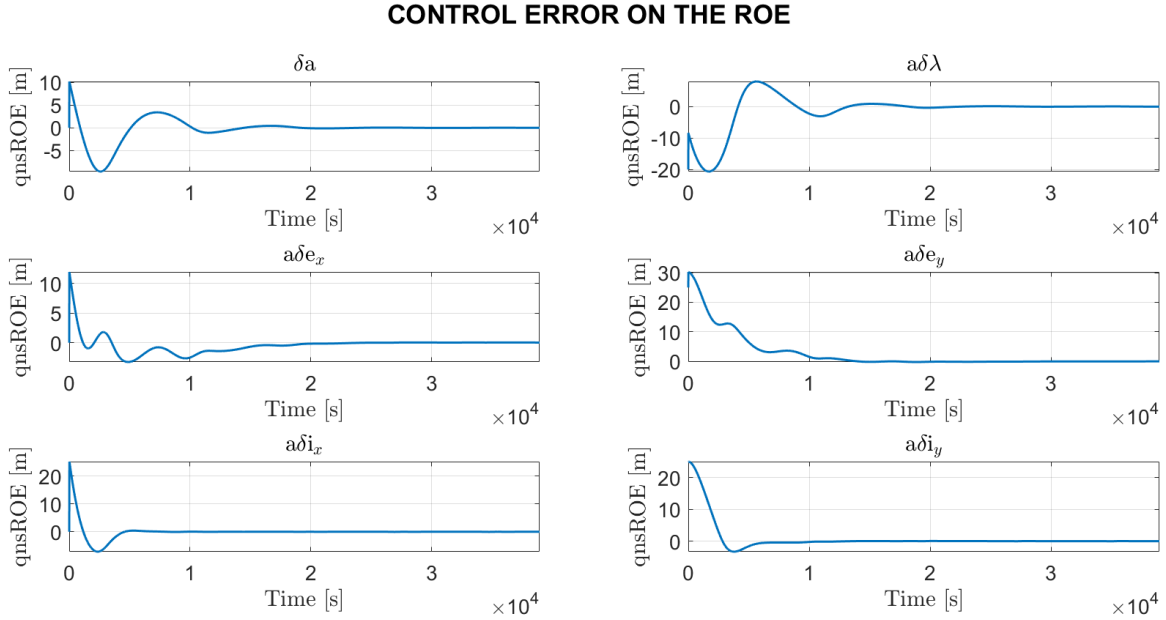


Figure 6.33: Control error on the qns-ROE

Table 6.8 reports the maximum and minimum force components required during the maneuver. These forces are primarily exerted during the transient phase of the control process. The forces reported refer to the ideal control inputs computed by the controller. In this experiment, no pulse-width modulation (PWM) or thruster actuation model is implemented to simulate the actual thruster behavior.

Table 6.8: Maximum and minimum force components along each axis

Force Component	Maximum [N]	Minimum [N]
F_x	1.83	-25.36
F_y	63.92	-0.22
F_z	0.03	-17.86

7 | Conclusions and Recommendations

This thesis has presented a comprehensive study on the modeling, guidance, and control of the final approach phase in Rendezvous and Docking (RVD) missions, with additional information regarding Formation Flying.

Achievements

The most notable contributions of this thesis can be summarized as follows:

- **Dual-framework modeling:** The translational dynamics were formulated using both the Cartesian representation (position and velocity) and the Relative Orbital Elements (ROE) approach.
- **Uncoupled translational and rotational motion:** Under the described assumptions, an uncoupled model for translational and rotational motion was elaborated.
- **Eccentric orbit extension:** While most existing literature focuses on circular or near-circular orbits, this thesis extends the ROE framework and the Tschauner-Hempel equations to support eccentric orbital conditions. This generalization is essential for future missions involving elliptical or higher-fidelity orbit requirements.
- **Guidance profile development:** Impulsive and continuous guidance strategies were both designed and implemented. Impulsive maneuvers offer fuel efficiency, while continuous guidance allows smoother control with lower risk in high-precision environments.
- **Optimal feedback control:** Linear Quadratic Regulator (LQR) techniques were employed to design controllers that balance tracking performance and control effort. The control law was derived and tested in both coordinate systems, validating its ability to ensure system stability and meet final docking constraints.
- **Simulation architecture:** A custom-built rendezvous simulator was developed,

integrating physical dynamics, thruster models, and software control logic. This environment enabled detailed performance evaluation under various test scenarios.

- **Rotational dynamics and attitude control:** The rotational behavior of the chaser was modeled to meet the necessary configuration for the final docking procedure.
- **Formation flying with feedback controller:** The e/i formation flying reconfiguration was performed by giving full authority to the feedback controller.

Discussion of Results

The case studies presented in this work demonstrate that the proposed algorithms can successfully guide the chaser spacecraft to meet docking conditions across a wide range of initial configurations and orbital regimes.

Results were obtained for both impulsive and continuous guidance strategies. In both cases, the docking objectives were achieved with high accuracy, validating the effectiveness of the control architecture. The impulsive strategy proved to be more fuel-efficient, as it leverages the natural motion of the chaser to a greater extent. However, this comes at the cost of longer maneuver durations. Conversely, the continuous guidance approach enables more flexible and time-efficient maneuvers at the expense of slightly higher propellant consumption. The choice between the two methods should be made based on mission-specific constraints, particularly regarding time availability, fuel budget, and safety considerations in the event of a partially executed maneuver.

Both the Cartesian- and ROE-based formulations demonstrated excellent performance in managing the final approach phase of an RVD mission. While the ROE-based control showed precise tracking and is suitable for long-term planning and formation flying, the Cartesian framework was found to be more intuitive and directly applicable to the final approach segment due to its clear physical interpretation. Importantly, the study confirms that the ROE-based controller is capable of achieving comparable precision to its Cartesian counterpart, thereby validating its applicability even in critical close-proximity operations. This is attractive to complement the design of the nominal guidance with strategies to handle off-nominal behavior of the propulsion system.

The attitude control system successfully maintained alignment between the chaser and the target spacecraft, ensuring synchronization in both attitude and angular velocity. This capability is essential to guarantee the correct orientation of the docking ports and to satisfy mechanical capture conditions.

The pulse-modulation strategy adopted for thruster management, although simplified, provided a preliminary validation of the controller's compatibility with discrete, non-throttleable propulsion systems.

Finally, the ROE-based technology was shown to be effective for e/i separation orbits, enabling formation flying with collision avoidance.

Recommendations for Future Work

This study opens several promising directions for further investigation:

- **Extension to disturbances:** The dynamical models are elaborated for an unperturbed environment. An extension of the equations of motion to include the effects of external disturbances such as the J_2 secular effect and aerodynamic drag can improve the model precision [22, 23].
- **Robust control integration:** The analysis of control strategies can be extended to a mixed-sensitivity \mathcal{H}_∞ controller for enhanced robustness [4].
- **Sensor modeling and navigation:** Current simulations assume Gaussian white noise on ideal measurements taken from previous studies [39]. The simulator should be extended to include a navigation filter.
- **Hybrid control strategies:** The trade-offs between impulsive and continuous control suggest that a hybrid approach could leverage the strengths of both. Investigating fuel-optimal control scheduling, perhaps using Model Predictive Control (MPC), could be an interesting direction.
- **Coupled translational and rotational motion:** By dropping the introduced hypothesis, the motion can be generalized to a target with arbitrary attitude, leading to a coupled model between translation and rotation. This would allow the study of more challenging scenarios involving non-collaborative targets [4].

Final Remarks

The work carried out in this thesis contributes both theoretically and practically to the domain of spacecraft rendezvous guidance and control. By addressing realistic orbital conditions, adopting a dual-framework modeling approach, and leveraging optimal control techniques, it provides a solid foundation for future developments in RV&D systems.

Bibliography

- [1] *Classical Two-Body Problem*, chapter Chapter 9, pages 519–576. . doi: 10.2514/5.9781624105210.0519.0576. URL <https://arc.aiaa.org/doi/abs/10.2514/5.9781624105210.0519.0576>.
- [2] *Gravitational Potential Field Models*, chapter Chapter 11, pages 621–646. . doi: 10.2514/5.9781624105210.0621.0646. URL <https://arc.aiaa.org/doi/abs/10.2514/5.9781624105210.0621.0646>.
- [3] *Spacecraft Formation Flying*, chapter Chapter 14, pages 767–862. . doi: 10.2514/5.9781624105210.0767.0862. URL <https://arc.aiaa.org/doi/abs/10.2514/5.9781624105210.0767.0862>.
- [4] F. Ankersen. Guidance, navigation, control and relative dynamics for spacecraft proximity maneuvers, Dec. 2010.
- [5] T. Bennett and H. Schaub. Continuous-time modeling and control using nonsingular linearized relative-orbit elements. *Journal of Guidance, Control, and Dynamics*, 39: 2605–2614, 12 2016. doi: 10.2514/1.G000366.
- [6] N. Bloise, E. Capello, M. Dentis, and E. Punta. Obstacle avoidance with potential field applied to a rendezvous maneuver. *Applied Sciences*, 7:1042, 10 2017. doi: 10.3390/app7101042.
- [7] A. E. Bryson and Y.-C. Ho. *Applied Optimal Control: Optimization, Estimation and Control*. Taylor & Francis, New York, 1975. ISBN 0-89116-320-5.
- [8] S. D'Amico. *Autonomous Formation Flying in Low Earth Orbit*. PhD thesis, 01 2010.
- [9] S. D'Amico and O. Montenbruck. Proximity operations of formation-flying spacecraft using an eccentricity/inclination vector separation. *Journal of Guidance, Control, and Dynamics*, 29, 05 2006. doi: 10.2514/1.15114.
- [10] Z. Dang. Solutions of tschauner–hempel equations. *Journal of Guidance, Control,*

- and Dynamics*, 40(11):2956–2960, 2017. doi: 10.2514/1.G002774. URL <https://doi.org/10.2514/1.G002774>.
- [11] V. S. Deshmukh and S. C. Sinha. Control of dynamic systems with time-periodic coefficients via the lyapunov-floquet transformation and backstepping technique. *Journal of Vibration and Control*, 10(10):1517–1533, 2004. doi: 10.1177/1077546304042064. URL <https://doi.org/10.1177/1077546304042064>.
- [12] L. Dieci. Numerical integration of the differential riccati equation and some related issues. *SIAM Journal on Numerical Analysis*, 29(3):781–815, 1992. ISSN 00361429. URL <http://www.jstor.org/stable/2158279>.
- [13] ESA CPO-WG. Guidelines on Safe Close Proximity Operations. Technical Report ESA-TECSYE-TN-022522, ESA, 2021.
- [14] European Space Agency. Atv, a very special delivery - lesson notes, 2025. URL https://www.esa.int/Education/Space_In_Bytes/ATV_a_very_special_delivery_-_Lesson_notes. Accessed: 2025-06-01.
- [15] European Space Agency. The russian soyuz spacecraft, 2025. URL https://www.esa.int/Enabling_Support/Space_Transportation/Launch_vehicles/The_Russian_Soyuz_spacecraft.
- [16] W. Fehse. *Automated Rendezvous and Docking of Spacecraft*. Cambridge Aerospace Series. Cambridge University Press, 2003.
- [17] R. Flores and E. Fantino. Computing classical orbital elements with improved efficiency and accuracy. *Advances in Space Research*, 75, 12 2024. doi: 10.1016/j.asr.2024.12.048.
- [18] C. Foster, J. Mason, V. Vittaldev, L. Leung, V. Beukelaers, and L. Stepan. Differential drag control scheme for large constellation of planet satellites and on-orbit results. *arXiv preprint arXiv:1806.01218*, 2018. URL <https://arxiv.org/abs/1806.01218>.
- [19] G. Gaias and S. D’Amico. Impulsive maneuvers for formation reconfiguration using relative orbital elements. *Journal of Guidance, Control, and Dynamics*, 38:1036–1049, 06 2015. doi: 10.2514/1.G000189.
- [20] G. Gaias and M. Lovera. Safe trajectory design for close proximity operations. 08 2020.
- [21] G. Gaias and M. Lovera. Trajectory design for proximity operations: The relative orbital elements’ perspective. *Journal of Guidance, Control, and Dynamics*, 44(12):

- 2294–2302, 2021. doi: 10.2514/1.G006175. URL <https://doi.org/10.2514/1.G006175>.
- [22] G. Gaias, J.-S. Ardaens, and O. Montenbruck. Model of j2 perturbed satellite relative motion with time-varying differential drag. *Celestial Mechanics and Dynamical Astronomy*, 123, 08 2015. doi: 10.1007/s10569-015-9643-2.
- [23] G. Gaias, C. Colombo, and M. Lara. Analytical framework for precise relative motion in low earth orbits. *Journal of Guidance, Control, and Dynamics*, 43(5):915–927, 2020. doi: 10.2514/1.G004716. URL <https://doi.org/10.2514/1.G004716>.
- [24] H. B. Hablani, M. L. Tapper, and D. J. Dana-Bashian. Guidance and relative navigation for autonomous rendezvous in a circular orbit. *Journal of Guidance, Control, and Dynamics*, 25(3):553–562, 2002. doi: 10.2514/2.4916. URL <https://doi.org/10.2514/2.4916>.
- [25] A. W. Koenig, T. Guffanti, and S. D’Amico. *New State Transition Matrices for Relative Motion of Spacecraft Formations in Perturbed Orbits*. doi: 10.2514/6.2016-5635. URL <https://arc.aiaa.org/doi/abs/10.2514/6.2016-5635>.
- [26] J. M. Longuski, F. R. Hoots, and G. E. P. IV. *Introduction to Orbital Perturbations*, volume 40 of *Space Technology Library*. Springer, 2022. ISBN 978-3-030-89758-1. doi: 10.1007/978-3-030-89758-1. URL <https://link.springer.com/book/10.1007/978-3-030-89758-1>.
- [27] F. L. Markley and J. L. Crassidis. *Attitude Kinematics and Dynamics*, pages 67–122. Springer New York, New York, NY, 2014. ISBN 978-1-4939-0802-8. doi: 10.1007/978-1-4939-0802-8_3. URL https://doi.org/10.1007/978-1-4939-0802-8_3.
- [28] MathWorks. *Design a Trajectory with Velocity Limits Using a Trapezoidal Velocity Profile*, 2024.
- [29] MathWorks. Choose an ode solver. <https://it.mathworks.com/help/matlab/math/choose-an-ode-solver.html>, 2025. URL <https://it.mathworks.com/help/matlab/math/choose-an-ode-solver.html>.
- [30] Moog Inc. Monopropellant thrusters, 2024. URL <https://www.moog.com/products/propulsion/space-propulsion/spacecraft-propulsion/thrusters/monopropellant-thrusters.html>.
- [31] NASA. International space station, 2025. URL <https://www.nasa.gov/international-space-station/>.

- [32] M. Nazari, W. Anthony, and E. Butcher. Continuous thrust stationkeeping in earth-moon l1 halo orbits based on lqr control and floquet theory. 08 2014. ISBN 978-1-62410-308-7. doi: 10.2514/6.2014-4140.
- [33] C. Peat. Iss - orbit, 2025. URL <https://www.heavens-above.com/orbit.aspx?satid=25544>. Accessed: 2025-06-01.
- [34] G. Popescu. Pixel geolocation algorithm for satellite scanner data. 06 2014.
- [35] R. Ramsdell and S. Miedema. Hydraulic transport of sand/shell mixtures. 09 2010.
- [36] M. Ramunno. Dynamical modeling and guidance algorithms for elliptic orbit rendezvous and impulsive proximity maneuvers. Master's thesis, Politecnico di Torino, Turin, Italy, 2024. URL <https://webthesis.biblio.polito.it/31204/>. Supervised by Marcello Romano, Thomas Peters, and Stefano Torresan.
- [37] L. Riggi and S. D'Amico. Optimal impulsive closed-form control for spacecraft formation flying and rendezvous. In *2016 American Control Conference (ACC)*, pages 5854–5861, 2016. doi: 10.1109/ACC.2016.7526587.
- [38] T. Sasaki. Linear time/parameter-varying models with relative orbit elements considering continuous controllability. *Journal of Guidance, Control, and Dynamics*, 48(1):177–191, 2025. doi: 10.2514/1.G008297. URL <https://doi.org/10.2514/1.G008297>.
- [39] D. Seer. Preliminary trade-off and design of a navigation method for collaborative rendezvous and docking. Master's thesis, Politecnico di Milano, 2024. URL https://www.politesi.polimi.it/retrieve/22a67952-0bc0-41a0-8241-48dabd8cac3c/2024_10_Seer_ExecutiveSummary.pdf. Executive Summary available online.
- [40] S. Skogestad and I. Postlethwaite. *Multivariable Feedback Control: Analysis and Design*, volume 2. 01 2005.
- [41] G. P. Sutton and O. Biblarz. *Rocket Propulsion Elements*. Wiley, 9th edition, 2016.
- [42] R. Tedrake. Chapter 8: Linear quadratic regulators. In *Underactuated Robotics: Algorithms for Walking, Running, Swimming, Flying, and Manipulation*. 2024. URL <https://underactuated.mit.edu/lqr.html>. Course notes for MIT 6.832.
- [43] G. Teschl. Chapter 3: Linear equations. In *Ordinary Differential Equations and Dynamical Systems*, volume 140 of *Graduate Studies in Mathematics*, pages 59–94. American Mathematical Society, 2012. ISBN 978-0-8218-8328-0. URL <https://www.mat.univie.ac.at/~gerald/ftp/book-ode/>.

- [44] Wikipedia contributors. Soyuz TMA-07m. https://en.wikipedia.org/wiki/Soyuz_TMA-07M.
- [45] Wikipedia contributors. Controllability Gramian — Wikipedia, The Free Encyclopedia, 2025. URL https://en.wikipedia.org/wiki/Controllability_Gramian.
- [46] Wikipedia contributors. Pulse-width modulation — Wikipedia, the free encyclopedia, 2025. URL https://en.wikipedia.org/wiki/Pulse-width_modulation.
- [47] D. Woffinden and D. Geller. Navigating the road to autonomous orbital rendezvous. *Journal of Spacecraft and Rockets*, 44:898–909, 06 2007. doi: 10.2514/1.30734.
- [48] K. Yamanaka and F. Ankersen. New state transition matrix for relative motion on an arbitrary elliptical orbit. *Journal of Guidance, Control, and Dynamics*, 25(1): 60–66, 2002. doi: 10.2514/2.4875. URL <https://doi.org/10.2514/2.4875>.
- [49] P. Young and J. Willems. An approach to the linear multivariable servomechanism problem. *International Journal of Control*, 15, 06 1972. doi: 10.1080/00207177208932211.
- [50] R. Zappulla II, J. Virgili-Llop, and M. Romano. Spacecraft thruster control via sigma-delta modulation. *Journal of Guidance, Control, and Dynamics*, 40:1–6, 07 2017. doi: 10.2514/1.G002986.

A | Appendix: Relative Motion Dynamics

The transformation matrix of Eq. (2.61) is presented here for the more general eccentric case. It is a 6×6 matrix, and its components are as follows:

$$T_{11} = -\frac{2e \sin \nu (e \cos \nu + 1)^2}{a(e^2 - 1)^2}$$

$$T_{12} = 0$$

$$T_{13} = -\frac{2(e \cos \nu + 1)(e^2 \cos^2 \nu + 3e \cos \nu + 2)}{a(e^2 - 1)^2}$$

$$T_{14} = \frac{2(e \cos \nu + 1)(-a\mu(e^2 - 1))^{3/2}}{a\mu^2(e^2 - 1)^2}$$

$$T_{15} = 0$$

$$T_{16} = -\frac{2e \sin \nu (-a\mu(e^2 - 1))^{3/2}}{a\mu^2(e^2 - 1)^2}$$

$$T_{21} = \frac{\sin^2 \nu (e \cos \nu + 2)}{a\eta} - \frac{2 \cos^2 \nu + e \cos^3 \nu - 1}{a(e^2 - 1)}$$

$$T_{22} = 0$$

$$T_{23} = \frac{\sin \nu (e^2 \cos^2 \nu + 4e \cos \nu + e^2 + 3)}{ae\eta} + \frac{\sin \nu (e \cos \nu + 1)(e \cos \nu + 3)}{ae(e^2 - 1)}$$

$$T_{24} = \frac{\sin \nu (e \cos \nu + 2)(e^2 + \eta - 1)(-a\mu(e^2 - 1))^{3/2}}{ae\mu^2\eta^3(e \cos \nu + 1)}$$

$$T_{25} = 0$$

$$T_{26} = -\frac{\cos \nu (-a\mu(e^2 - 1))^{3/2}}{ae\mu^2(e^2 - 1)} - \frac{\cos \nu (e \cos \nu + 1)^2 - e(2e \cos \nu + 2)}{ae\mu^2\eta(e \cos \nu + 1)^2} (-a\mu(e^2 - 1))^{3/2}$$

$$T_{31} = \frac{e \sin \omega (2 \cos^2 \nu + e \cos^3 \nu - 1)}{a(e^2 - 1)} + \frac{e \cos \omega \sin \nu (e + 2 \cos \nu + e \cos^2 \nu)}{a(e^2 - 1)}$$

$$T_{32} = -\frac{e \cos i (\sin(\nu + 2\omega) - \sin \nu + e \sin(2\omega))}{2a \sin i (e^2 - 1)}$$

$$T_{33} = \frac{(e \cos \nu + 1) \left(3 \cos(\nu + \omega) + \frac{5e \cos \omega}{2} + \frac{e \cos(2\nu + \omega)}{2} \right)}{a(e^2 - 1)}$$

$$T_{34} = -\frac{(-a\mu(e^2 - 1))^{3/2} \left(2 \cos(\nu + \omega) + \frac{3e \cos \omega}{2} + \frac{e \cos(2\nu + \omega)}{2} \right)}{a\mu^2(e^2 - 1)(e \cos \nu + 1)}$$

$$T_{35} = \frac{e \sin(\nu + \omega) \sin \omega (-a\mu(e^2 - 1))^{3/2}}{a\mu^2 \tan i (e^2 - 1)(e \cos \nu + 1)}$$

$$T_{36} = \frac{\sin(\nu + \omega) (-a\mu(e^2 - 1))^{3/2}}{a\mu^2(e^2 - 1)}$$

$$T_{41} = \frac{e \sin \nu \sin \omega (e + 2 \cos \nu + e \cos^2 \nu)}{a(e^2 - 1)} - \frac{e \cos \omega (2 \cos^2 \nu + e \cos^3 \nu - 1)}{a(e^2 - 1)}$$

$$T_{42} = \frac{e \cos i \cos \omega (\cos(\nu + \omega) + e \cos \omega)}{a \sin i (e^2 - 1)}$$

$$T_{43} = \frac{(e \cos \nu + 1) \left(3 \sin(\nu + \omega) + \frac{5e \sin \omega}{2} + \frac{e \sin(2\nu + \omega)}{2} \right)}{a(e^2 - 1)}$$

$$T_{44} = -\frac{\left(2 \sin(\nu + \omega) + \frac{3e \sin \omega}{2} + \frac{e \sin(2\nu + \omega)}{2} \right) (-a\mu(e^2 - 1))^{3/2}}{a\mu^2(e^2 - 1)(e \cos \nu + 1)}$$

$$T_{45} = -\frac{e \sin(\nu + \omega) \cos \omega (-a\mu(e^2 - 1))^{3/2}}{a\mu^2 \tan i (e^2 - 1)(e \cos \nu + 1)}$$

$$T_{46} = -\frac{\cos(\nu + \omega) (-a\mu(e^2 - 1))^{3/2}}{a\mu^2(e^2 - 1)}$$

$$T_{51} = 0$$

$$T_{52} = \frac{\sin(\nu + \omega) + e \sin \omega}{a(e^2 - 1)}$$

$$T_{53} = 0$$

$$T_{54} = 0$$

$$T_{55} = \frac{\cos(\nu + \omega) (-a\mu(e^2 - 1))^{3/2}}{a\mu^2(e^2 - 1)(e \cos \nu + 1)}$$

$$T_{56} = 0$$

$$T_{61} = 0$$

$$T_{62} = -\frac{\cos(\nu + \omega) + e \cos \omega}{a(e^2 - 1)}$$

$$T_{63} = 0$$

$$T_{64} = 0$$

$$T_{65} = \frac{\sin(\nu + \omega) (-a\mu(e^2 - 1))^{3/2}}{a\mu^2(e^2 - 1)(e \cos \nu + 1)}$$

$$T_{66} = 0$$

B | Appendix: Results

B.1. Test 2: RV&D using Impulsive Guidance

Guidance profile

Table B.1: $\Delta\mathbf{V}$ table (Part 1)

Time [s]	ΔV_x	ΔV_y	ΔV_z
0.0	0.00519	-0.00036	0.00227
44.0	0.01041	-0.00070	0.00470
88.1	0.01041	-0.00063	0.00508
132.1	0.01041	-0.00056	0.00544
176.1	0.01041	-0.00049	0.00581
220.2	0.01040	-0.00042	0.00616
264.2	0.01040	-0.00035	0.00652
308.2	0.01039	-0.00027	0.00687
352.3	0.01037	-0.00019	0.00722
396.3	0.01036	-0.00011	0.00757
440.3	0.01034	-0.00003	0.00792
484.4	0.01032	0.00005	0.00826
528.4	0.01030	0.00014	0.00860
572.5	0.01027	0.00023	0.00895
616.5	0.01025	0.00032	0.00929
660.5	0.01021	0.00042	0.00963
704.6	0.01018	0.00052	0.00997
748.6	0.01014	0.00063	0.01031
792.6	0.01009	0.00073	0.01065
836.7	0.00563	0.00081	0.01074
879.5	0.00116	0.00086	0.01062

Table B.2: $\Delta\mathbf{V}$ table (Part 2)

Time [s]	ΔV_x	ΔV_y	ΔV_z
922.4	0.00111	0.00089	0.01054
965.3	0.00106	0.00093	0.01046
1008.2	0.00100	0.00097	0.01038
1051.0	-0.00114	0.00101	0.01039
1095.1	-0.00329	0.00104	0.01029
1139.1	-0.00335	0.00104	0.01001
1183.1	-0.00341	0.00104	0.00972
1227.1	-0.00347	0.00105	0.00944
1271.1	-0.00352	0.00105	0.00916
1315.1	-0.00358	0.00106	0.00887
1359.1	-0.00364	0.00106	0.00859
1403.1	-0.00370	0.00107	0.00832
1447.2	-0.00376	0.00107	0.00804
1491.2	-0.00382	0.00108	0.00776
1535.2	-0.00389	0.00108	0.00748
1579.2	-0.00395	0.00108	0.00720
1623.2	-0.00401	0.00109	0.00691
1667.2	-0.00408	0.00109	0.00663
1711.2	-0.00414	0.00110	0.00635
1755.2	-0.00206	0.00054	0.00310

Simulation Results: Cartesian-based Controller

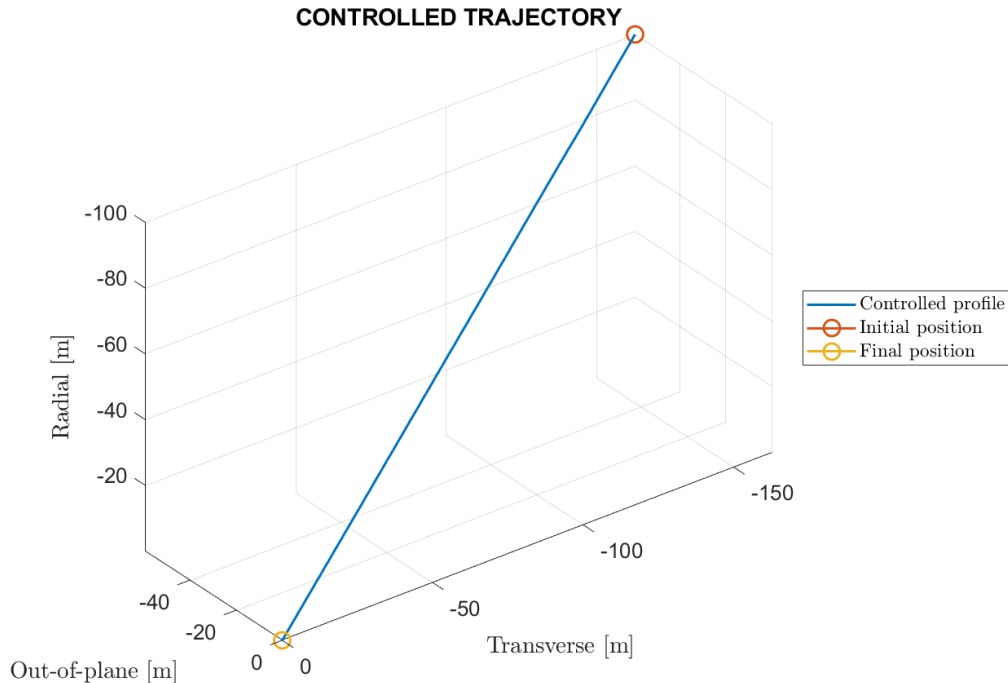


Figure B.1: Controlled trajectory (LVLH frame)

Simulation Results: ROE-based Controller

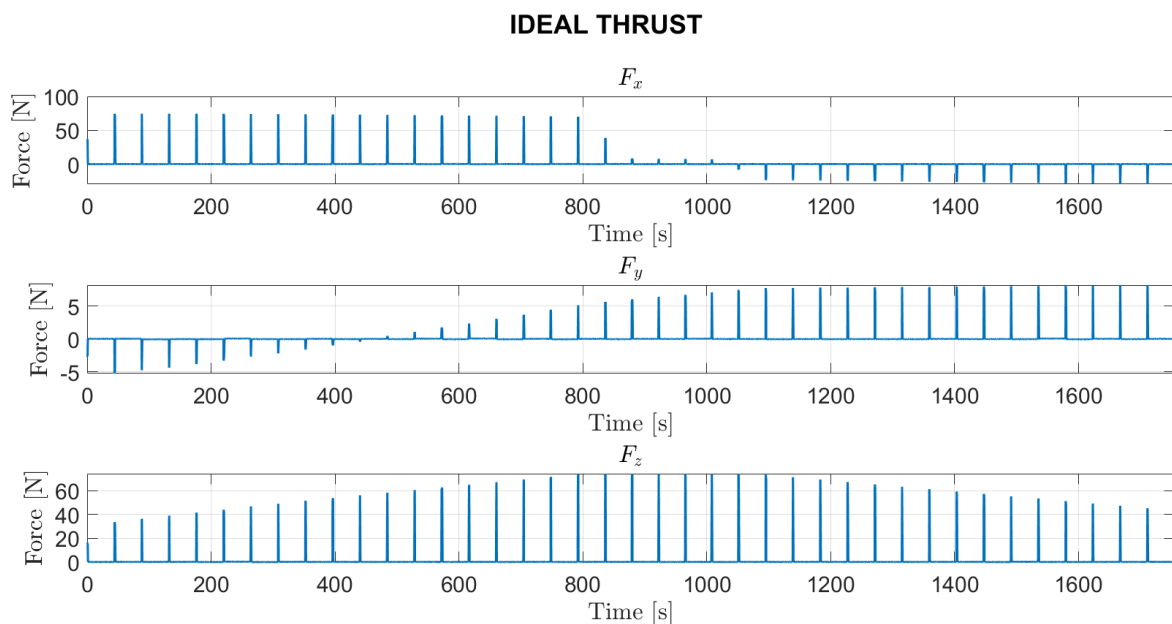


Figure B.2: Ideal thrust (body frame)

B.2. Test 3: RV&D using Continuous Guidance

Simulation Results: Cartesian-based Controller

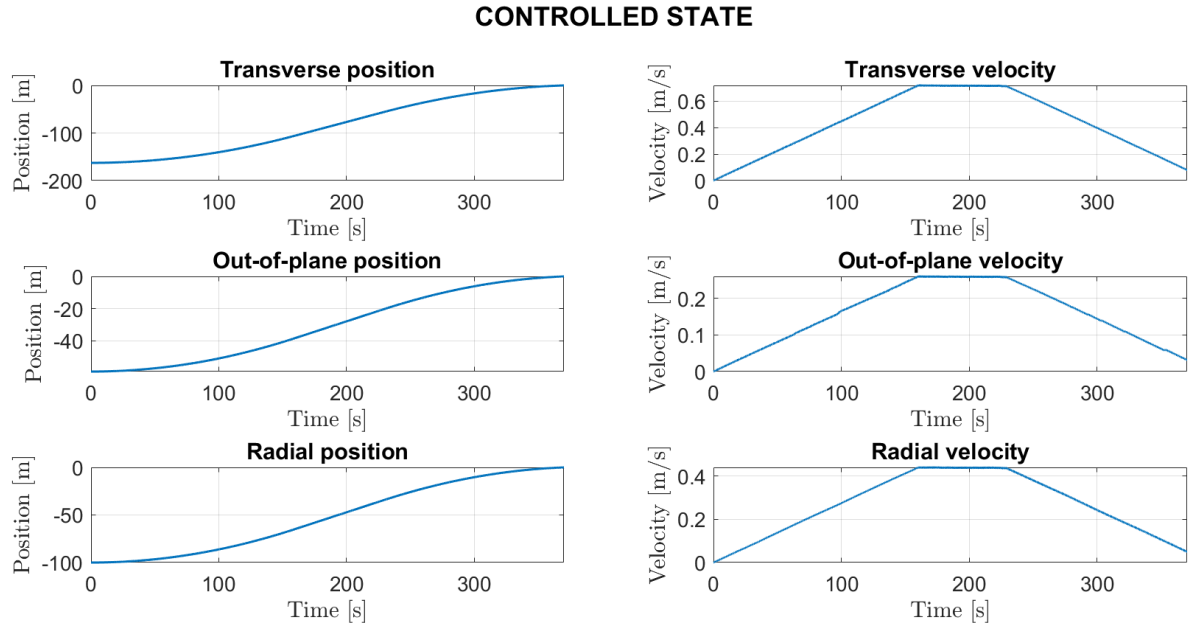


Figure B.3: Time evolution of the controlled profile (LVLH frame)

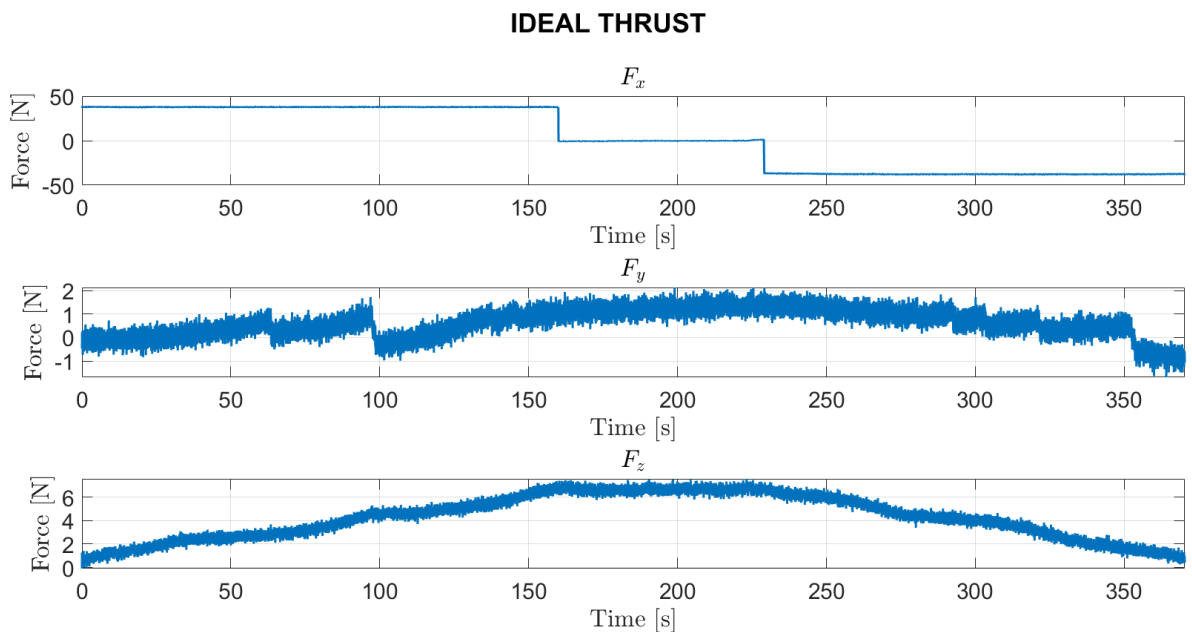


Figure B.4: Ideal thrust (body frame)

Simulation Results: ROE-based Controller

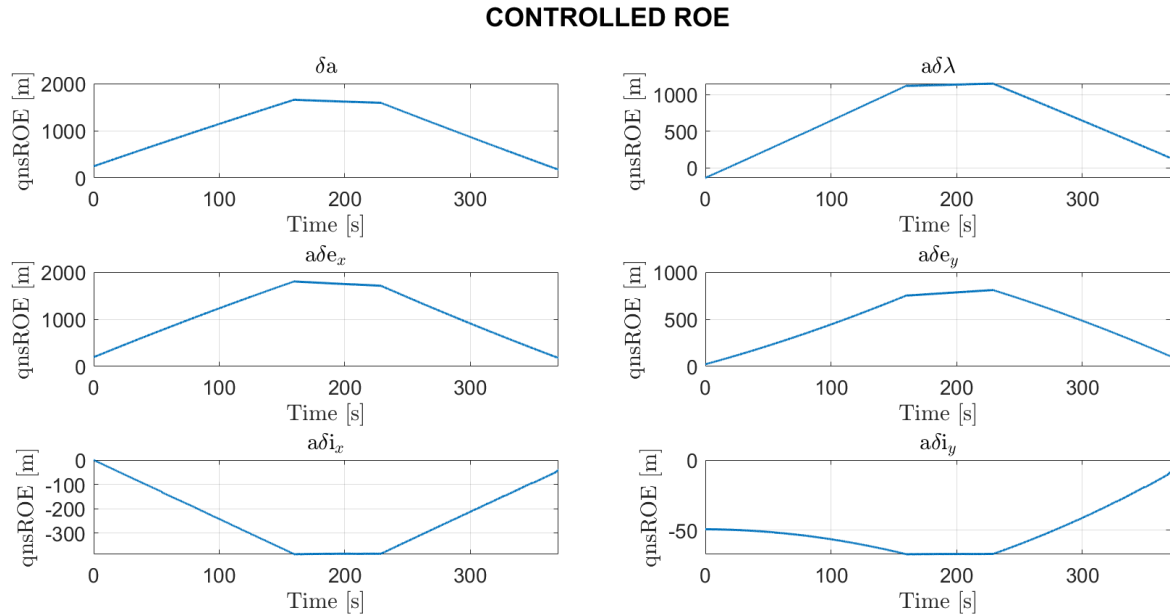


Figure B.5: Time evolution of the controlled ROE

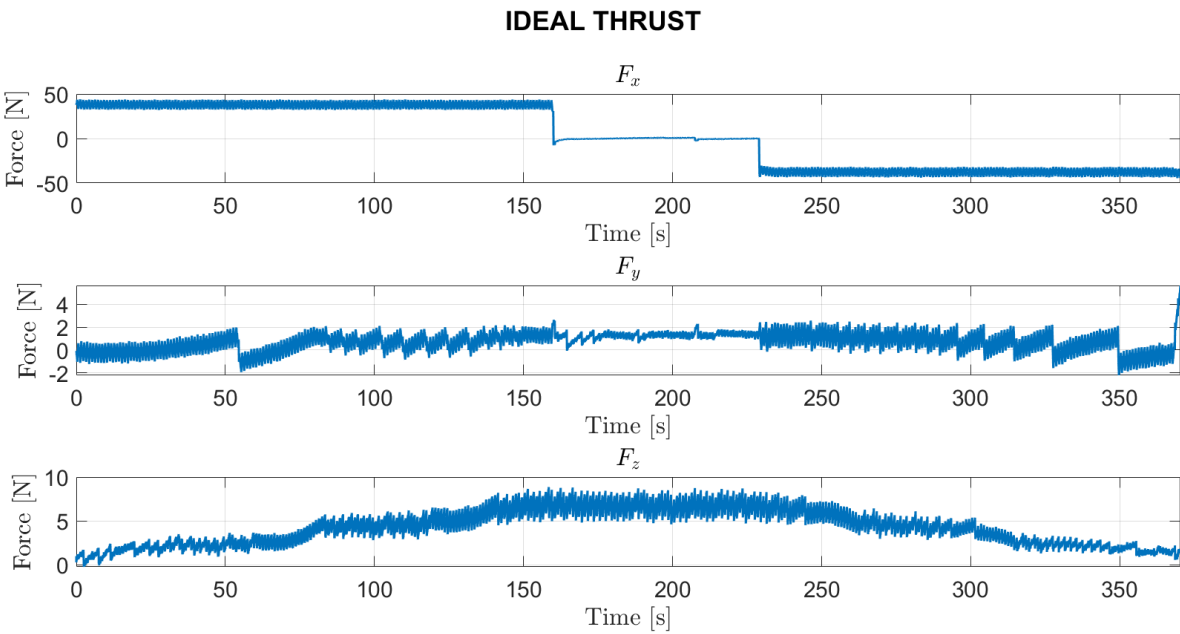


Figure B.6: Ideal thrust (body frame)

List of Figures

2.1	ECI reference frame (from Ref. [34])	10
2.2	LVLH reference frame (from Ref. [6])	11
2.3	321 rotation set (from Ref. [18])	33
3.1	Simulator	39
3.2	Simulator/ Real World	40
3.3	Simulator/ Real World/ Dynamics	41
3.4	Simulator/ Real World/ Dynamics/ Absolute Dynamics	41
3.5	Simulator/ Real World/ Dynamics/ Relative States	43
3.6	Simulator/ On-Board Software	45
3.7	Pulse-width-modulation (From Ref. [46])	47
4.1	Decelerating inbound glideslope (from Ref. [24])	53
4.2	Accelerating inbound glideslope (from Ref. [24])	53
4.3	Trapezoidal velocity profile (from Ref. [28])	54
6.1	Control gain: DRE integration	82
6.2	Control gains: DRE integration	83
6.3	Control gains: DRE integration (steady state)	84
6.4	Control gain: DRE integration	85
6.5	Guidance trajectory (LVLH frame)	86
6.6	Time evolution of the reference state (LVLH frame)	87
6.7	Time evolution of the reference qns-ROEs	87
6.8	Control gain: DRE integration	88
6.9	Control gain: DRE integration (steady state) vs Infinite horizon	89
6.10	Control gains: DRE integration	90
6.11	Control gains: DRE integration (steady state)	90
6.12	Control gain: DRE integration	91
6.13	Control gain: DRE integration (steady state) vs Infinite horizon	91
6.14	Time evolution of the controlled profile (LVLH frame)	92
6.15	Control error on the state (LVLH frame)	92

6.16 Ideal thrust (body frame)	93
6.17 Commanded thrust (body frame)	94
6.18 Control error on the attitude (body frame)	95
6.19 Control torque (body frame)	95
6.20 Time evolution of the controlled qns-ROE	97
6.21 Control error on the qns-ROE	97
6.22 Control error on the Cartesian state (LVLH frame)	98
6.23 Commanded thrust (body frame)	98
6.24 Reference acceleration (Rotated docking frame)	100
6.25 Time evolution of the reference state (LVLH frame)	101
6.26 Time evolution of the reference qns-ROEs	101
6.27 Control error on the state (LVLH frame)	102
6.28 Commanded thrust (body frame)	102
6.29 Control error on the qns-ROE	103
6.30 Control error on the state (LVLH frame)	104
6.31 Commanded thrust (body frame)	104
6.32 Time evolution of the controlled qns-ROE	105
6.33 Control error on the qns-ROE	106
B.1 Controlled trajectory (LVLH frame)	122
B.2 Ideal thrust (body frame)	122
B.3 Time evolution of the controlled profile (LVLH frame)	123
B.4 Ideal thrust (body frame)	123
B.5 Time evolution of the controlled ROE	124
B.6 Ideal thrust (body frame)	124

List of Tables

3.1	Standard deviation values used for noise modeling	46
5.1	ISS orbital data	68
5.2	Target body frame attitude with respect to LVLH	69
5.3	ISS inertial and geometrical data	70
5.4	RV&D scenario data	71
5.5	Soyuz inertial and geometrical data	72
5.6	MONARC-90HT datasheet	72
5.7	ISS eccentricity for near-circular orbit	73
5.8	ISS eccentricity	75
5.9	Parameters based on initial and final state	76
5.10	Parameters for impulsive guidance profile	77
5.11	Parameters: continuous guidance	77
6.1	Control gain matrix: DRE integration (steady state) and ARE solution . .	82
6.2	Control gain: DRE integration (steady state) and ARE solution	85
6.3	Overview of the impulsive manoeuvres	86
6.4	Thruster firing times and total propellant consumption	94
6.5	Thruster firing times and total propellant consumption	99
6.6	Thruster firing times and total propellant consumption	103
6.7	Thruster firing times and total propellant consumption	105
6.8	Maximum and minimum force components along each axis	106
B.1	$\Delta\mathbf{V}$ table (Part 1)	121
B.2	$\Delta\mathbf{V}$ table (Part 2)	121

List of Symbols

Symbol	Description	SI Unit
a_{dec}	Deceleration (negative acceleration)	m/s^2
\mathbf{a}_{drag}	Aerodynamic drag acceleration	m/s^2
\mathbf{a}_{ext}	External acceleration vector	m/s^2
$\mathbf{a}_g(\mathbf{r})$	Gravitational acceleration at position \mathbf{r}	m/s^2
\mathbf{a}_{J_2}	Acceleration due to J2 perturbation	m/s^2
$\mathbf{A}(t)$	Plant matrix	6×6 matrix
$\mathbf{A}_{a/b}$	DCM from frame b to a	3×3 matrix
$\boldsymbol{\alpha}_{\text{kep}}$	Keplerian orbital elements vector	$\text{m}, -, \text{rad}$
$\boldsymbol{\alpha}_{\text{qns}}$	Quasi-nonsingular orbital elements vector	$-, \text{rad}$
b	Semi-minor axis	m
C_d	Drag coefficient	—
$\delta\boldsymbol{\alpha}_{\text{kep}}$	Relative Keplerian orbital elements	$\text{m}, -, \text{rad}$
$\delta\boldsymbol{\alpha}_{\text{qns}}$	Relative QNS orbital elements	$-, \text{rad}$
Δt_{dec}	Time interval between impulses in deceleration	s
$\Delta \mathbf{v}$	Instantaneous velocity change (impulsive maneuver)	m/s
$\dot{\omega}$	Time derivative of angular velocity	rad/s^2
$\dot{\omega}_{c/t}^c$	Time derivative of relative angular velocity	rad/s^2
$\dot{\rho}$	Velocity along the glideslope	m/s
$\dot{\rho}_f$	Final velocity at landing	m/s
$\dot{\rho}_{f,\text{acc}}$	Velocity at end of acceleration phase	m/s
$\dot{\theta}_x$	Derivative of Euler angle θ_x	rad/s
$\dot{\theta}_y$	Derivative of Euler angle θ_y	rad/s
$\dot{\theta}_z$	Derivative of Euler angle θ_z	rad/s
e	Orbital eccentricity	—
e_x	Component of eccentricity (x-axis)	rad
e_y	Component of eccentricity (y-axis)	rad
η	Eccentricity function	—

Symbol	Description	SI Unit
$e^{\mathbf{A}(t-\tau)}$	Matrix exponential	6×6 matrix
g_0	Standard gravity	m/s^2
G	Gravitational constant	$\text{m}^3/(\text{kg}\cdot\text{s}^2)$
h	Specific angular momentum	m^2/s
\mathbf{I}	Inertia tensor matrix	$\text{kg}\cdot\text{m}^2$
I_s	Specific impulse	s
I_{tot}	Total impulse	$\text{N}\cdot\text{s}$
i_x	Component of inclination vector (x-axis)	rad
i_y	Component of inclination vector (y-axis)	rad
$J(\nu)$	Scaled integral of motion function	—
J_2	Earth's second zonal harmonic	—
λ	Mean longitude	rad
$\mu = GM$	Gravitational parameter of Earth	m^3/s^2
M	Mean anomaly	rad
\mathbf{M}	External torque on body	$\text{N}\cdot\text{m}$
M_c	Control torque on chaser	$\text{N}\cdot\text{m}$
M_p	Propellant mass	kg
M_t	Control torque on target	$\text{N}\cdot\text{m}$
m_c	Mass of chaser spacecraft	kg
m_t	Mass of target spacecraft	kg
\mathbf{M}_{ext}	External torque vector	$\text{N}\cdot\text{m}$
n	Mean motion / Impulse index	$\text{rad}/\text{s} / -$
N_{dec}	Number of impulses during deceleration	—
ν	True anomaly	rad
$\Omega(\omega)$	Quaternion kinematics matrix	4×4 matrix
p	Semi-latus rectum	m
$\Phi(t, t_0)$	State transition matrix (STM)	6×6 matrix
\mathbf{q}	Quaternion (attitude representation)	—
\mathbf{q}_{rel}	Relative attitude quaternion	—
\mathbf{r}_c	Position vector of chaser spacecraft (inertial frame)	m
r_{eq}	Earth's equatorial radius	m
r_t	Radial distance of the target spacecraft	m
ρ	Atmospheric density (kg/m^3)	kg/m^3

Symbol	Description	SI Unit
ρ_f	Final position of the glideslope	m
$\rho_{f,\text{coast}}$	Final position at end of coasting phase	m
$\rho_{f,\text{dec}}$	Final position during deceleration	m
\mathbf{s}	Relative position vector (chaser wrt target)	m
\mathbf{s}_{rot}	Relative position vector in LVLH frame	m
S	Cross-sectional area	m^2
t_{disc}	Thrust command discretization interval	s
t_{fire}	Thruster firing time	s
t_{imp}^-	Time before impulse	s
t_{imp}^+	Time after impulse	s
T_{acc}	Duration of acceleration phase	s
T_{coast}	Duration of coasting phase	s
T_{dec}	Duration of deceleration phase	s
T_{ideal}	Ideal thrust required	N
T_{real}	Actual thruster capability	N
u	Mean argument of latitude ($= M + \omega$)	rad
$\mathbf{u}(t)$	Control input vector	m/s^2
v	Orbital velocity at true anomaly ν	m/s
\mathbf{v}_{atm}	Atmospheric velocity vector	m/s
x	Relative position in LVLH frame	m
$\mathbf{x}(t)$	Relative state vector $[x, y, z, \dot{x}, \dot{y}, \dot{z}]^T$	$\text{m}, \text{m}/\text{s}$
x_b	Body frame x-axis	—
y	Relative position in LVLH frame	m
y_b	Body frame y-axis	—
z	Relative position in LVLH frame	m
z_b	Body frame z-axis	—
$\mathcal{X}(t)$	Fundamental matrix of LTV system	6×6 matrix
$\boldsymbol{\omega}$	Target angular velocity vector (LVLH)	rad/s
$\boldsymbol{\omega}_B^B$	Angular velocity in body frame	rad/s
$\boldsymbol{\omega}_{B/N}^B$	Angular velocity of body wrt inertial (body frame)	rad/s
$\boldsymbol{\omega}_{c/t}^c$	Relative angular velocity chaser wrt target	rad/s
$\boldsymbol{\omega}_c^c$	Angular velocity of chaser in chaser frame	rad/s
$\boldsymbol{\omega}_N^B$	Angular velocity of inertial frame in body frame	rad/s
$\boldsymbol{\omega}_t^c$	Angular velocity of target in chaser frame	rad/s

List of Acronyms

Acronym	Meaning
ECI	Earth-Centered Inertial
LVLH	Local Vertical Local Horizontal
ROE	Relative Orbital Elements
HCW	Hill-Clohessy-Wiltshire
TH	Tschauner-Hempel
LQR	Linear Quadratic Regulator
AR&D	Autonomous Rendezvous and Docking
DRE	Differential Riccati Equation
ARE	Algebraic Riccati Equation
ISS	International Space Station
RVD/B	Rendezvous and Docking/Berthing

Acknowledgements

I would like to express my heartfelt gratitude to my academic advisor, Prof. Gabriella Vittoria Maria Gaias, as well as my company supervisors, Stefano Torresan and Thomas Peters, for their invaluable support, guidance, and technical advice throughout the development of this thesis. I am also sincerely thankful to the AOCS & GNC department of OHB SE System AG for offering me the opportunity to carry out my thesis in such a dynamic and inspiring environment, where I had the chance to learn from experts in the field.

A special thank you goes to my family, who have always stood by my side throughout my life and academic journey, both in good times and in challenging ones. Their unwavering moral support has been fundamental in achieving this milestone.

I am also deeply grateful to my friends and my girlfriend for always being there for me, especially during the moments when I felt discouraged and doubted my ability to complete my exams or this thesis. Your encouragement made all the difference. A special thanks to those who supported me not only emotionally but also by studying together (those long hours were tough, but we made it through). Not feeling alone on this journey was one of the key factors that kept me focused and determined to reach this final result.

